UNIVERSITY OF CALIFORNIA SAN DIEGO

Ku-band Transmit/Receive All-Silicon Planar Phased Arrays for SATCOM and SOTM Terminals

A dissertation submitted in partial satisfaction of the
requirements for the degree
Doctor of Philosophy

in

Electrical Engineering (Electronic Circuits and Systems)

by

Gökhan Gültepe

Committee in charge:

Professor Gabriel M. Rebeiz, Chair
Professor Gert Cauwenberghs
Professor William Hodgkiss
Professor Vitaliy Lomakin
Professor Daniel Sievenpiper

2021

The dissertation of Gökhan Gültepe is approved, and it is acceptable in quality and form for publication on microfilm and electronically.

University of California San Diego

2021

DEDICATION

To my beloved family and friends

EPIGRAPH

İstikbal göklerdedir. / The future is in the skies.

–Mustafa Kemal Atatürk

TABLE OF CONTENTS

LIST OF FIGURES

LIST OF TABLES

ACKNOWLEDGEMENTS

I would first like to thank my advisor, Professor Gabriel M. Rebeiz, for his invaluable expertise, guidance and endless support during my doctoral studies. When I first joined TICS Group, I was really anxious even though I had a bit of experience before. I sat on the meeting table which I saw in his slides a year ago during his recognition speech at the National Academy of Engineering ceremony. Sometimes, there were 8 students around the table waiting to present their work in a meeting lasting up to 5-6 hours. Although I was extremely anxious and shy in the beginning, I saw that some senior students also contributed and shared their ideas. Then, I realized why we were attending those crowded and everlasting meetings. It was to encourage brainstorming and collaboration for greater good and a great learning opportunity. I was pretty amazed when he was able to comment on many different subjects, not only technical but also historical or business related. Although, sometimes, I had some terrible moments, I also enjoyed his funny stories and anecdotes. Everything on that table was to prepare us for the life after graduation. Besides I learned a lot from him, I am really glad to know him. He also supported me when I had a serious medical problem. When I called him early morning to inform him that I could not attend the meeting with professionals which would start in an hour due to an emergency, he said in 5 minutes he would take me from home and help me go to hospital, and he supported me and asked about my condition almost every day during my recovery. I know that Prof. Rebeiz will always share his experience and be my ally if I face a problem I could not solve on my own. I am also glad to work with him after my graduation.

I would like to thank my dissertation committee members, Prof. Gert Cauwenberghs, Prof. William Hodgkiss, Prof. Vitaliy Lomakin and Prof. Daniel Sievenpiper for their time, interest, and valuable comments about my research studies.

I would like to thank Prof. Özlem A. Çivi for her guidance during my master studies. She led me to work with Prof. Rebeiz when I asked her about my decision to pursue my doctoral studies abroad.

I would like to thank Ahmed Nafe, Bhaskara Rupakula and Kevin Low for the discussions about some antenna and system design related problems and their invaluable friendship. I would like to thank Dimitrios Baltimas, my friend across the Aegean Sea, for his friendship and the great conversations about science and politics and Tom Phelps for his friendship, volleyball, quality time and burgers. He persistently tried to convince me to go surfing with him, but I was too lazy to wake up early. I would like to thank my colleagues in the future, Qian Ma, Hyunchul Chung and Yusheng Yin, for their friendship and support.

I would like to thank my other TICS group colleagues I had a chance to spend time with, Abdurrahman Aljuhani, Zhe Zhang, Abdulrahman Alhamed, Oğuz Kazan, Arman Galioğlu, Jacob Schalch, Siwei Li, Yaochen Wang, Changtian Wang, Zhaoxin Hu, Shufan Wang, Mustafa Lokhandwala, Sultan Alqarni, Eric Wagner, Umut Kodak, Li Gao and Omar El-Aassar for their technical discussions and friendship. I would also like to thank the previous TICS group members, Samet Zihir and Tumay Kanar for their help and support.

I would like to thank Faruk Gencel, Arda Şimşek and Onur Atan for their support and friendship while I was trying to blend in and adapt to the America's Finest City, San Diego. I would like to thank my friends I met at UC San Diego, Cenk Demir, Elana Metz, Can Uysalel, Kazım Ergün, Rüveyda Ayasun, Scott Lancaster, Ayman Jabaren, Aman Raj, Michelle Rodriguez, Maxine Van Doren, Nina Hagen Kaldhol, Pınar Şen and Tuğcan Aktaş for the time we enjoyed.

I would like to thank Burak Alptuğ Yılmaz for listening my complaints and supporting me, when everything goes south, and sharing my success. After I moved in San Diego, he never stopped calling me as a brother, and I hope we would live closer again. I would like to thank Meltem Parlak, Mehmet Gökcan Bayrak and Seda Acıkara for visiting me in San Diego and make me have a wonderful break from work. I would also like to thank Buket Akın whom our paths crossed in the City of Angels for her support. I would also like to thank my friends in Turkey, Selin Aktaş, Murat Özatay, Tolga Dağdelen, Berkay and Ece Çalışkan, Ozan Hazır, Taylan Yapıcı, Abdullah Onur Koyuncu, Arda Deveci, Ömürcan Demiralp, Dilem Karakaya, Gizem Aktaş and

Pelin Çıbık.

Finally, I would like to thank parents, Gülay and Bahattin Gültepe, for their support, love and encouragement. I should express my gratitude to my sister, Serpil Gültepe, and my aunt, Kadriye Araol, for their unconditional support. They always listened to me, and my graduation would not be possible without her support. I would also like to thank my deceased uncle, Murat Araol, who would be proud.

This dissertation was completed with the generous support of Renesas Electronics America (formerly IDT), Qualcomm and Kyocera International, San Diego.

The material in this dissertation is based on the following papers which are either published, has been submitted for publication, or contains material that is currently being prepared for submission for publication.

Chapter 2, in part, is a reprint of the material as it appears in: G. Gultepe, S. Zihir, T. Kanar and G. M. Rebeiz, "A Dual-Polarized 1024-Element Ku-band SATCOM Transmit Phased-Array with $\pm 70°$Scan and 43.5 dBW EIRP," *2020 IEEE/MTT-S International Microwave Symposium (IMS)*, Los Angeles, CA, USA, 2020, pp. 837-840, doi: 10.1109/IMS30576.2020.9223977. The dissertation author was the primary investigator and author of this paper.

Chapter 2, in full, has been submitted for publication of the material as it may appear in: G. Gültepe, T. Kanar, S. Zihir and G. M. Rebeiz, "A 1024-Element Ku-Band SATCOM Phased-Array Transmitter with 45 dBW Single-Polarization EIRP", in *IEEE Transactions on Microwave Theory and Techniques*, accepted. The dissertation author was the primary investigator and author of this paper.

Chapter 3, in part, is a reprint of the material as it appears in: G. Gultepe, S. Zihir, T. Kanar and G. M. Rebeiz, "A Dual-Polarized 1024-Element Ku-band SATCOM Phased-Array with Embedded Transmit Filter and >10 dB/K G/T," presented at 2021 IEEE/MTT-S International Microwave Symposium (IMS), Atlanta, GA, USA, Jun. 10, 2021. The dissertation author was the primary investigator and author of this paper.

Chapter 3, in full, has been submitted for publication of the material as it may appear in: G. Gültepe, T. Kanar, S. Zihir and G. M. Rebeiz, "A 1024-Element Ku-band SATCOM Dual-Polarized Receiver with $>$10 dB/K G/T and Embedded Transmit Rejection Filter", in *IEEE Transactions on Microwave Theory and Techniques*, accepted. The dissertation author was the primary investigator and author of this paper.

Chapter 4, in part, is a reprint of the material as it appears in: G. Gultepe and G. M. Rebeiz, "A 256-Element Dual-Beam Dual-Polarization Ku-Band Phased-Array with 5 dB/K G/T for Simultaneous Multi-Satellite Reception," presented at 2021 IEEE/MTT-S International Microwave Symposium (IMS), Atlanta, GA, USA, Jun. 10, 2021. The dissertation author was the primary investigator and author of this paper.

Chapter 4, in full, has been submitted for publication of the material as it may appear in: G. Gültepe and G. M. Rebeiz, "A 256-Element Dual-Beam Polarization-Agile SATCOM Ku-Band Phased-Array with 5 dB/K G/T", in *IEEE Transactions on Microwave Theory and Techniques*, submitted. The dissertation author was the primary investigator and author of this paper.

VITA

2015	Bachelor of Science in Electrical and Electronics Engineering, Middle East Technical University, Turkey
2017	Master of Science in Electrical and Electronics Engineering, Middle East Technical University, Turkey
2015-2018	Antenna Design Engineer, Aselsan Inc., Turkey
2021	Doctor of Philosophy in Electrical Engineering (Electronic Circuits and Systems), University of California San Diego

PUBLICATIONS

G. Gultepe, T. Kanar, S. Zihir and G. M. Rebeiz, "A 1024-Element Ku-Band SATCOM Phased-Array Transmitter with 45 dBW Single-Polarization EIRP," in *IEEE Transactions on Microwave Theory and Techniques* (accepted).

G. Gultepe, T. Kanar, S. Zihir and G. M. Rebeiz, "A 1024-Element Ku-band SATCOM Dual-Polarized Receiver with >10 dB/K G/T and Embedded Transmit Rejection Filter," in *IEEE Transactions on Microwave Theory and Techniques* (accepted).

G. Gultepe and G. M. Rebeiz, "A 256-Element Dual-Beam Polarization-Agile SATCOM Ku-Band Phased-Array with 5 dB/K G/T," in *IEEE Transactions on Microwave Theory and Techniques* (submitted).

G. Gultepe, S. Zihir, T. Kanar and G. M. Rebeiz, "A Dual-Polarized 1024-Element Ku-band SATCOM Phased-Array with Embedded Transmit Filter and >10 dB/K G/T," presented at 2021 IEEE/MTT-S International Microwave Symposium (IMS), Atlanta, GA, USA, Jun. 10, 2021.

G. Gultepe and G. M. Rebeiz, "A 256-Element Dual-Beam Dual-Polarization Ku-Band Phased-Array with 5 dB/K G/T for Simultaneous Multi-Satellite Reception," presented at 2021 IEEE/MTT-S International Microwave Symposium (IMS), Atlanta, GA, USA, Jun. 10, 2021.

G. Gultepe, S. Zihir, T. Kanar and G. M. Rebeiz, "A Dual-Polarized 1024-Element Ku-band SATCOM Transmit Phased-Array with $\pm 70^{\circ}$ Scan and 43.5 dBW EIRP," *2020 IEEE/MTT-S International Microwave Symposium (IMS)*, Los Angeles, CA, USA, 2020, pp. 837-840, doi: 10.1109/IMS30576.2020.9223977.

G. Gultepe, D. Dogan and O. A. Civi, "An Interleaved LTSA Array on a Waveguide Beamformer with Dual-Plane Monopulse," *2019 13th European Conference on Antennas and Propagation (EuCAP)*, Krakow, Poland, 2019, pp. 1-4.

G. Gultepe, D. Dogan and O. A. Civi, "Waveguide-based monopulse wideband travelling-wave array," *2017 IEEE International Symposium on Antennas and Propagation & USNC/URSI National Radio Science Meeting*, San Diego, CA, 2017, pp. 823-824, doi: 10.1109/APUSNCURSINRSM.2017.8072454.

D. Dogan and G. Gultepe, "A beamforming method enabling easy packaging of scalable architecture phased arrays," *2016 IEEE International Symposium on Phased Array Systems and Technology (PAST)*, Waltham, MA, USA, 2016, pp. 1-4, doi: 10.1109/ARRAY.2016.7832562.

ABSTRACT OF THE DISSERTATION

Ku-band Transmit/Receive All-Silicon Planar Phased Arrays for SATCOM and SOTM Terminals

by

Gökhan Gültepe

Doctor of Philosophy in Electrical Engineering (Electronic Circuits and Systems)

University of California San Diego, 2021

Professor Gabriel M. Rebeiz, Chair

Although phased array is a 100-year-old concept, the research and development efforts have been driven by the defense industry and radio astronomy for many decades. An active electronically scanned array (AESA) has also been getting popular in commercial satellite communications (SATCOM) and 5G cellular applications. With the recent advances in the silicon technologies, the cost barrier for commercial products has been broken down especially after the deployment of 5G wireless technologies. This dissertation focuses on building cost-efficient, all-silicon, planar, SATCOM phased arrays with agile beam steering for SATCOM ground and SATCOM on-the-move (SOTM) terminals, as well as emerging non-geosynchronous-

orbit (NGSO) communication systems. It presents a 1024-element transmit (TX) and receive (RX) planar phased array pair and a 256-element scalable phased array tile with multi-satellite reception capability for Ku-band SATCOM terminals. All the three planar arrays employ silicon beamformer chips mounted on an affordable printed circuit boards, dual-polarized antennas to synthesize rotated linear polarization with high cross polarization rejection for Ku-band SATCOM applications and Wilkinson network with surface mount technology (SMT) resistors. The RX arrays also comprise silicon low-noise amplifiers (LNA) placed at the antenna terminals to increase antenna gain-to-noise temperature (G/T) without enlarging the array size. Record results in EIRP and G/T are demonstrated for the transmit and receive arrays, together with the first affordable two-beam phased-array for satellite and consumer terminal applications.

Chapter 1

Introduction

1.1 Background on Satellite Communications

Satellites are the keystones of the modern global communication networks. Geosynchronous (GEO) satellites have been serving for military ground, maritime, and airborne satellite communications on-the-move (SOTM) and commercial television and connectivity services. Although sparsely spaced GEO satellites can cover large lands, the demand for global connectivity with faster communication and higher bandwidth created a demand for non-geosynchronous constellations.

Low-Earth-Orbit (LEO) constellations arose from the need for global connectivity in 1990s, in which the world wide web and online activities had just been booming. The lack of demand and the high costs prevented the success of the ventures at that time [10].

Nowadays, the demand for broadband data is soaring. Everything is going virtual, and teleworking trend, a consequence of the pandemic, has made fast, broadband internet connectivity with low latency essential. Underserved and rural areas need internet services more than ever. New business models with LEO constellations, attracting funding from many investors contrary to 1990s, aim to provide feasible solutions for internet access because they offer much faster

internet service than a priori fixed cable infrastructure [10]. In early 2021, there have already been 2,612 LEO satellites orbiting the Earth compared to the preexisting 562 GEO satellites. The US owns 1,897 of the total 3,372 satellites in operation, and 1,486 of 1,897 are for commercial use [11]. The number of LEO satellites are growing since the LEO constellations also rely on satellite to satellite communication links.

This new business also needs ground stations, gateways and user terminals. Although parabolic dishes have been used for those, they are not the best option to track the satellites. LEO satellites are moving very fast, and they enter and exist the field of view of the ground terminals in a very short time. This necessitates the terminal to follow the signal, and break the current connection and make a new one with the next satellite. As a parabolic dish needs a mechanical mount with a motor to align its boresight with a satellite, the relatively slower rate of angular rotation, the high, long-term maintenance costs and the keyhole problem, an active electronically steered array antenna (AESA) better suits the task. This is because it can steer the beam in a large conical space even without a mechanical rotation.

With the developments in 5G in the last decade, AESAs have already been deployed for broadband communication. The silicon technology has been getting advanced and lower cost without sacrificing the performance to follow the demand. The commercial SATCOM also takes advantage of it, and the fierce competition is on designing and manufacturing an affordable AESA for both business and commercial users.

Hence, the motivation behind the studies presented in this dissertation is to design cost-efficient, all-silicon and high performance phased arrays for Ku-band SATCOM ground and SOTM terminals for both LEO and GEO satellite systems.

1.2 Existing SATCOM Antenna System Topologies

Historically, SATCOM antennas rely on mechanically steered parabolic dishes or waveguide slot arrays [42–49]. These require gimbals and motors to align the boresight and the antenna polarization (unless the antenna is dual-polarized) with the satellite. The use of motors to rapidly rotate and hold the bulky antenna at a fixed angle increases the power consumption and requires motors with large torque capabilities. They also suffer from a keyhole problem when the satellite being tracked just passes above the antenna (90° elevation) [50], so the antenna should immediately rotate in azimuth by 180°. Also, these motors need maintenance and a closed-loop control system to minimize the pointing error.

(a) (b)

Figure 1.1: (a) Intellian v85NX, a Ku- to Ka-band convertible maritime VSAT antenna system with a 85 cm diameter reflectors [1]. (b) Viasat's second-generation Ku/Ka broadband airborne terminal with waveguide horn array, Global Aero Terminal-5530 (GAT-5530) [2].

To overcome these issues, phased arrays are preferred for SATCOM applications. A phased array antenna (PAA) can steer its main beam to anywhere without the requirement of a physical rotation. The concept relies on having multiple small elements with individually controlled radiation phase. The progressive phase shift applied between the elements determines the beam pointing angle. It also allows simultaneous tracking of multiple satellites/objects for

systems with multiple beams. One drawback of the phased arrays is the need for separate transmit and receive arrays due to the large frequency separation for the Tx and Rx bands, and to eliminate any coupling between the TX and RX paths for full-duplex operation. Another drawback is the scan loss due to the reduction in the effective aperture size when the antenna is scanned to large angles. However, phased-arrays can be manufactured as flat panels, which is aerodynamically advantageous in airborne applications, and multiple-beam reception from the same aperture is possible. In the past, phased-arrays were built using GaAs modules, which are quite expensive due to their low yield and non-ease of packaging. This prevented the penetration of the phased arrays into the commercial market. Yet, they have been widely used in defense application, such as radars. On example of a GaAs-based phased array is the Connexion-by-Boeing Ku-band phased array [51]. Later, SiGe chips with high performance decreased the phased-array cost and started to make them more affordable.

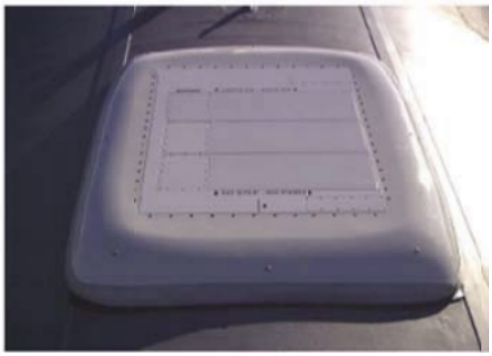

Figure 1.2: Connexion-by-Boeing Flat-Panel GaAs-based Phased-Array [51].

There are several alternative to silicon-based phased-arrays which have a planar design and can be used for SATCOM application. A very popular planar array based on the Variable Inclination Continuous Transverse Stub Array (VICTS) from ThinKom [3]. It is a planar leaky-wave antenna with an inherent beam-squint depending on the operating frequency [4]. In order to do beam scanning, it requires that 3 waveguide layers are rotated mechanically, namely the feed, aperture and polarizer layers. The feed is the traveling-wave parallel plate structure, and when the rotating the Continuous Transverse Stub (CTS) on the aperture layer, the beam can be steered in

the H-plane (elevation). If both the feed and the aperture layers are rotated together, the beam can be steered in azimuth. The polarizer plate coverts the inherent linear polarization into either LHCP or RHCP [3]. Although it is a very low loss structure, it still suffers from the keyhole effect and is very heavy. Also, it requires precise machining especially at Ka-band. Its profile is slightly higher than conventional electronically scanned arrays (ESA). One of its advantages is the metal structure more easily dissipates the heat, but the aperture amplitude profile is fixed.

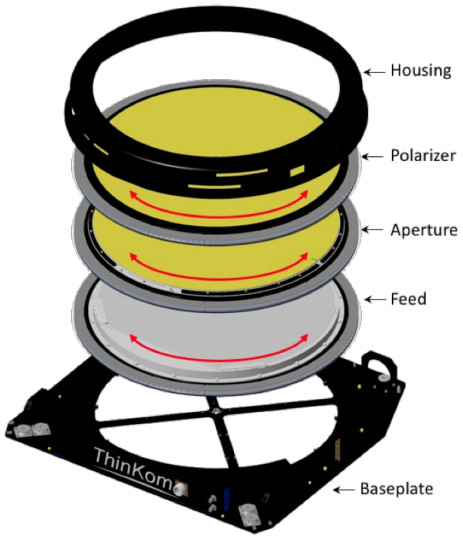

Figure 1.3: ThinKom's variable inclination continuous transverse stub (VICTS) phased array [3].

Kymeta and Alcan Systems have developed a different way to reduce costs by using low cost LCD and TFT technologies and the proven high-yield assembly lines of flat panel televisions. Although both companies use the LCD technology to steer the beam without moving parts, their approaches are very different. Alcan Systems employs Microwave Liquid Crystal (MLC) technology [5] to individually alter the propagation delay of the inverted microstrip (IMSL) feed line of each slot coupled patch antenna. Applying a different voltage to each cell, the phase shift at the input of each element can be controlled and a progressive phase shift is applied. On the other hand, Kymeta uses TFT manufacturing process to place a metasurface [6] onto the broadwall of a waveguide structure. By tuning the voltage applied to the LCD on each scatterer

element, a patch element fed by a subwavelength slot, the resonant frequency of the antenna changes and creates a diffractive surface to steer the beam [7]. It does not use active phase shifters and variable gain amplifiers.

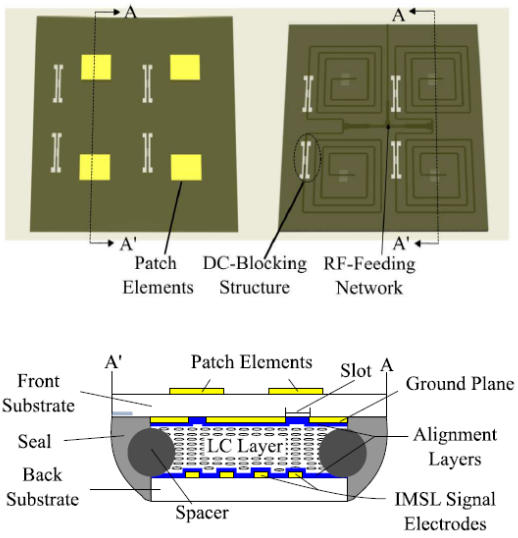

(a)

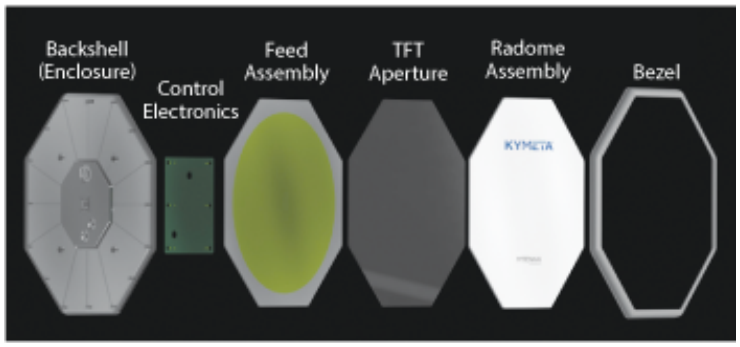

(b)

Figure 1.4: Phased arrays based on the current LCD technologies: (a) Alcan Systems' Microwave Liquid Crystal (MLC) technology [5]. (b) Kymeta's phased array with mTenna^{TM} technology [8].

Another antenna for SATCOM application is being developed by Isotropic Systems. This antenna uses planar sub-arrays covered with a small lenses to enhance the gain and performs sub-array beamforming. Although it decreases the number of active elements and provides a scalable design, it has problems with the need of higher power per element for the required EIRP, grating lobes due to discontinuous sub-array spacing, and periodic dips in the antenna gain as one

is moving from one beam to another (fed by a different element on the focal plane of the small lenses).

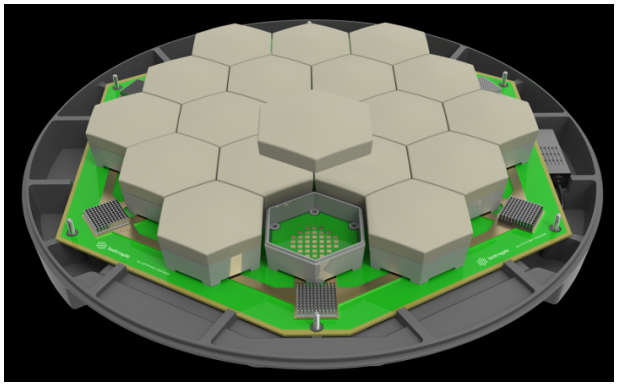

Figure 1.5: Isotropic System's Ku-band satellite terminal [9].

To the author's knowledge, except for Thinkom, none of these systems have yet been used in commercial applications on commercial aircraft, ships or any defense systems. They are all in the development phase with the goal of lowering the cost of phased-arrays. However, the huge reduction in cost of SiGe beamformers from \$10/channel in the early days to <\$1/channel (in large quantities) have made SiGe and CMOS phased-arrays to be a compelling solution for high-performance LEO and GEO systems.

1.3 Thesis Overview

This thesis presents demonstrations of affordable, flat-panel, high performance Ku-band SATCOM active electronically scanned array antenna systems and their system analysis.

Chapter 2 presents a 1024-element Ku-band phased array transmitter for mobile satellite communications. The array is based on 8-channel transmit (TX) SiGe beamformer chips. Dual-polarized stacked-patch antennas enable the array to synthesize linear, rotated-linear, left-hand and right-hand circular polarization. The array consists of four quadrants of 256-element sub-arrays, each of which has 64 beamformer chips and a driver chip assembled on a printed circuit

board (PCB). The array achieves an effective isotropic radiated power (EIRP) of 75 dBm per polarization (78 dBm circular polarization), and scans to $\pm 75^\circ$ in all planes. This is achieved using an antenna spacing of $\lambda/2$ at 14.4 GHz in an equilateral triangular grid. The array also results in 30 dB cross-polarization rejection up to 60° scan angles. Measured error vector magnitude (EVM) for 50, 100, 200 and 500 MBaud QPSK and 8PSK waveforms result in at most 1.5%rms and 2.5%rms at P1dB and Psat, respectively, at 14 GHz over all scan angles. Also, the adjacent channel power ratio (ACPR) was measured as -32 dB for 200 and 500 MBaud QPSK and 8PSK waveforms at P1dB at 14 GHz. To the authors' knowledge, this work presents a state-of-the-art planar phased-array system with high EIRP for Ku-band SATCOM mobile transmitter terminals.

Chapter 3 presents a 1024-element dual-polarized Ku-band (10.7-12.7 GHz) SATCOM receive (RX) phased-array. The array consists of four 16×16 sub-array tiles, each of which comprises 64 8-channel beamformer chips, 256 dual-channel low-noise amplifiers (LNA) and 256 dual-polarized antennas built on an affordable printed circuit board (PCB). The antennas spaced at $\lambda/2$ spacing at 12.2 GHz in an equilateral triangular grid allow scanning up to $\pm 70^\circ$ in all planes while maintaining a cross-polarization level $<$-30 dB. The use of LNAs just after the antennas enables a low noise operation with an antenna gain-to-noise-temperature (G/T) of 10.5 dB/K (T_{ant}=20 K) at broadside while maintaining a directivity of 34 dB at 11.7 GHz. Also, a 2-pole/2-zero filter is placed between the LNA and the beamformer chip to greatly attenuate any transmit leakage signal at 14-14.5 GHz. The lightweight, low-cost PCB with all silicon chips and a thickness of 3.4 mm presents a viable candidate for Ku-band satellite communications (SATCOM) ground and Satcom-On-The-Move (SOTM) terminals.

Chapter 4 presents a 16×16 dual-polarized Ku-band (10.7-12.7 GHz) SATCOM phased-array receiver with simultaneous dual-beam reception capability. The array incorporates 64 16-channel beamformer chips and 256 dual-polarized antennas. A dual-channel LNA is employed on every antenna to lower the system NF and increase the G/T. The phased-array is built on a low-cost printed circuit board (PCB), with an antenna spacing of $\lambda/2$ at 12.2 GHz in an equilateral

triangular grid to result in $\pm 70^\circ$ scan volume, and is capable of receiving two concurrent data-streams with distinct direction of arrival (DOA) since it employs two 64:1 Wilkinson combiner networks. A transmit band (14-14.5 GHz) filter is also implemented between the LNA and the beamformer chip. The 256-element array has a directivity of 28 dB at mid-band with a G/T of 5 dB/K (T_{ant}=20K), which results in a G/T of 11 dB/K for a 1024-element array. This array is a feasible solution for make-before-brake connections and for multi-satellite reception systems, such as simultaneous TV reception and connectivity.

Chapter 5 concludes the dissertation and discusses future work.

Chapter 2

A 1024-Element Ku-Band SATCOM Phased-Array Transmitter with 45 dBW Single-Polarization EIRP

2.1 Introduction

Mobile satellite communication (SATCOM) provides a feasible solution for broadband internet access to underserved areas [12]. Low-Earth orbit (LEO) satellites constellations, with orbits at 800-1200 kms and a latency of 30 ms, are currently being built and launched for this purpose, and are expected to enter operation in 2021 and 2022. The LEO satellites have a typical rise to set times of 0.5-1 hour, and need to be constantly tracked, and an active electronically scanned array (AESA) is essential for reliable operation (Fig. 2.1a). Also, phased-arrays are promising for ground, maritime, and airborne satellite communications-on-the-move (SOTM) platforms for both LEO and GEO applications since the antenna can be pointed quickly to the satellite and can easily compensate for the platform motion [13–15].

This paper expands on [16] and presents a low cost Ku-band SATCOM ground terminal

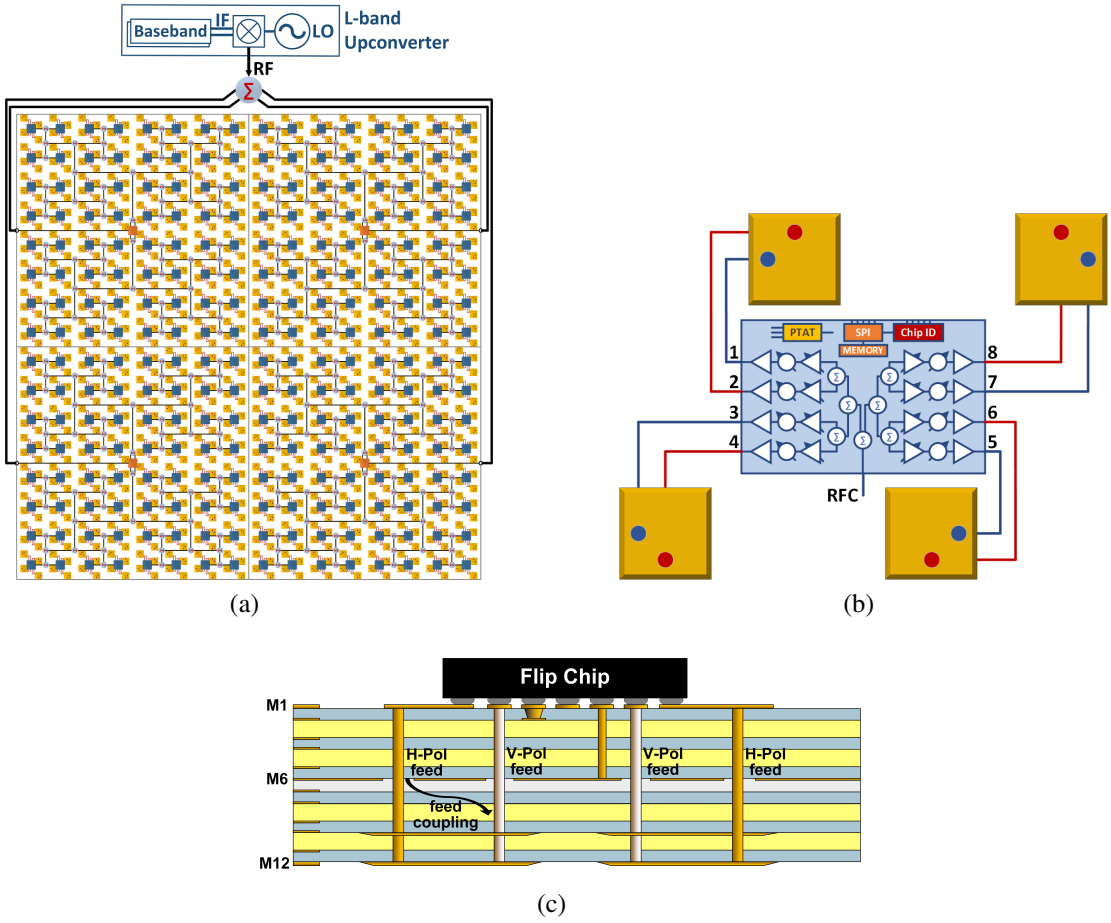

Figure 2.1: (a) A 1024-element dual-polarized SATCOM transmit phased-array based on 8-channel beamformer chips. (b) 2x2 sub-array with an 8-channel Ku-band transmit beamformer chip. (c) 12-layer PCB stackup.

solution, which is a 1024-element dual-polarized transmit phased-array (Fig. 2.1). The array architecture is based on commercial SiGe beamformers feeding dual-polarized stacked patch antennas and assembled on a low-cost printed circuit board (PCB) [17–21]. Compared to previous work in [19], this paper presents a larger array with embedded drivers, a wider scan based on a triangular grid, and detailed analysis and measurements of complex waveform with QPSK, 8-PSK modulation. This work shows that it is possible to build high EIRP phased-arrays for both LEO and GEO SATCOM using SiGe chips. It also shows that using an embedded driver chip does not affect the transmit EVM since the noise due to the L-band upconverter at the input is much higher

than the noise introduced by the driver chips. Complex waveform measurements indicate that the array operates efficiently at the 1-dB compression point with low ACPR, removing the need for back-off.

2.2 1024-Element Phased-Array Design

Fig. 2.1 presents the Ku-band SATCOM transmit phased-array architecture. The 1024-element phased-array is build by combining four 256-element sub-array quadrants, which are cut to the grid to achieve 2xN scalability without grating lobes. An external 1:4 Wilkinson divider feeds the four quadrants, but also, a single transmit beamformer chip can be used instead for RF distribution to the four panels. The RF signal at the input of a 256-element sub-array is first amplified by a driver chip placed at the quadrant center, and then distributed to the beamformer chips using a Wilkinson divider network. The design is based on 8-channel TX beamformer chips which can feed a 2x2 quad of dual-polarized antennas. Each quadrant is built on a multi-layer PCB with antennas on one side and the beamformer chips on the other side.

2.2.1 TX Beamformer Chip

The SiGe beamformer chip contains 8-channels each with a 4-bit variable gain amplifier (VGA), a 6-bit phase-shifter (PS), and a medium power-amplifier (PA). The chip can be controlled by using a serial peripheral interface (SPI) with 50 MHz clock speed. In this work, the first generation Renesas F6501 beamformer chips are used, with a gain of 22-23 dB at 14 GHz, 11 dBm output 1-dB compression point (OP1dB) and a 3-dB bandwidth of 12.4-14.5 GHz. At the output P1dB point, the power consumption per channel is 165 mW from a 2.3 V supply. The 4-bit VGA enables provides more than 20 dB attenuation with a maximum 0.4 dB RMS gain error, and the 6-bit phase shifter has 5.625° steps with less than 3° RMS phase error.

Note that new generation beamformer chips (F6521S) from Renesas consume 100 mW at

Table 2.1: TX SiGe Beamformer Summary

Parameter	Unit	F6501 BF
Frequency	GHz	12.4-14.5
No. of Channels	-	8
Package	-	FC-BGA
Nominal Gain	dB	22-23
OP_{1dB}	dBm	11
Phase Shifter	bit	6
Phase Step	degree	5.625
VGA	bit	4
Gain Control	dB	20
Power/channel	mW	165
Supply Voltage	V	2.3

an OP1dB of 10 dBm and will greatly reduce the power consumption.

2.2.2 PCB and Antenna Design

The 256-element sub-arrays are built on a 12-layer PCB stackup based on Panasonic Megtron6 with ε_r=3.63 and tanδ=0.004 at 14 GHz (Fig. 4.1c). The flip-chip ball-grid-array (FC-BGA) chips are assembled on M1 (RF layer) with M2 as ground, and the RF power at the output of beamformer channels is transmitted to the probe-fed patch antenna on M10 using a plated through hole. A parasitic patch antenna is placed on M12 to enhance the antenna bandwidth, and M6 is designated as the antenna ground. M3, M4 and M5 layers are dedicated to power supply and digital control distribution.

A probe-fed microstrip patch antenna can only provide 2-5% impedance bandwidth and operates with a 500 MHz bandwidth at 14.25 GHz. A stacked patch antenna with double-tuned resonance is used for wider impedance and better scan performance [22].

Fig. 2.2a presents the top (M1) and bottom (M12) layers of the antenna including the

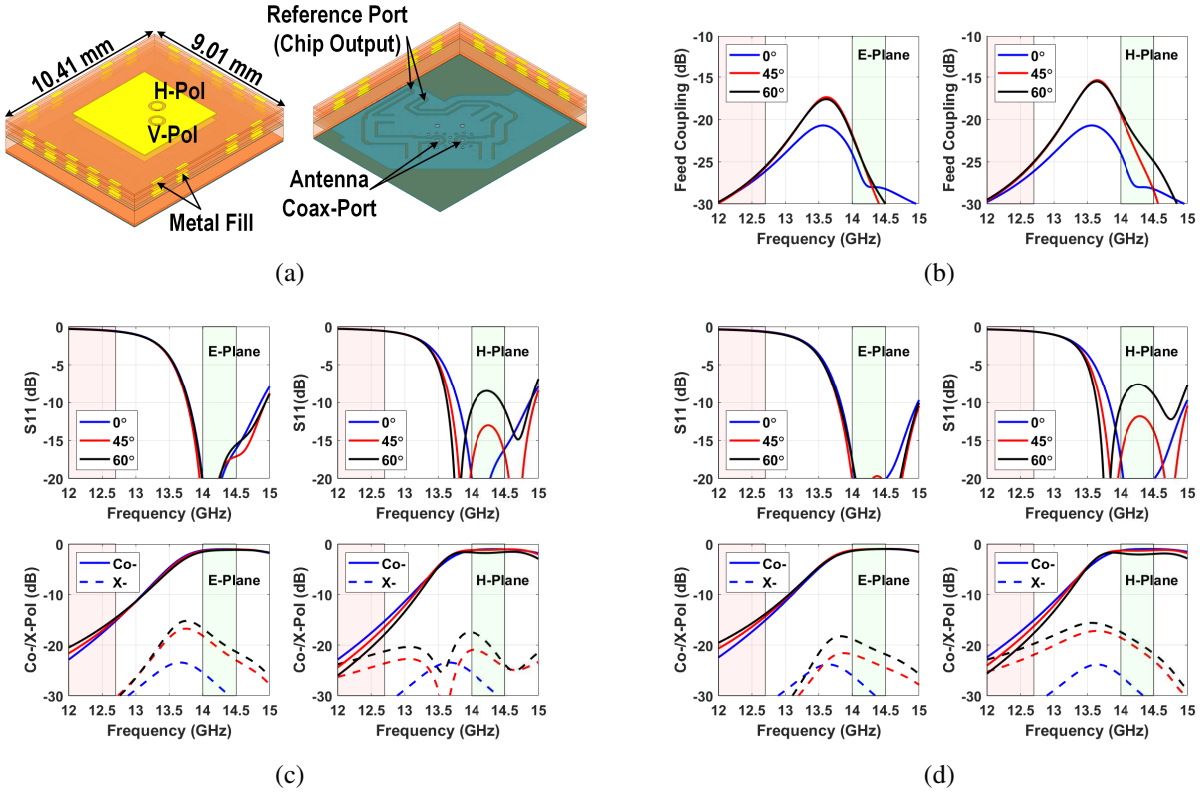

Figure 2.2: (a) 14-14.5 GHz antenna model. (b) Feed coupling (H- to V-pol. or vice versa) vs. scan angle. Simulated S_{11}, co-pol and cross-pol vs. scan angle (0°, 45°, 60°) at the reference port for (c) H-Pol antenna and (d) V-pol antenna.

stacked patch antenna, coaxial feeds and the matching network placed between the chip and the coaxial antenna feed. This model is simulated in ANSYS HFSS, applying primary and secondary lattice pairs with Floquet-port excitation. The lattice pairs and the lattice vectors on the Floquet port are set to impose an equilateral triangular grid for best scan performance. The grating lobes in the H-polarization direction are split into two and are located off-axis when the array-factor in k-space is plotted for a triangular grid [23]. The array employs a grid of 10.41×9.01 mm (D_x=0.5 λ and D_y=0.25$\sqrt{3}$ λ @ 14.4 GHz). This enables a scanning capability in ±80° cone and results in a directivity of 4.25 dB per element at 14.25 GHz (midband):

$$D_{element} = 10\log_{10}\left(\frac{4\pi D_x D_y}{\lambda^2_{@14.25\,GHz}}\right) = 4.25\,dB \tag{2.1}$$

and the 32x32 array achieves a directivity of 34.35 dB at 14.25 GHz with a 3-dB beamwidth of 3.7° under uniform illumination.

$$D_{array} = 10\log_{10}(1024) + D_{element} = 34.35\,dB \tag{2.2}$$

A two-pole matching circuit is used for antenna impedance mathching and also provides enhanced suppression in the Ku-band SATCOM receive band (10.7-12.75 GHz). Fig 3.3c and Fig. 3.3d present the simulated reflection coefficient at the chip output port, and the radiation transfer functions of the horizontally and vertically polarized antenna ports. The dual-polarized antennas have a return loss $>$ 15 dB in the E-plane even for 60° scan angle. Also, the return loss is at least 12 dB and 8 dB for 45° and 60° scan angles, respectively, for the H-plane. The co-polarized response includes the dielectric loss, ohmic losses up to the chip output port, the mismatch and polarization losses, and is 1.1 dB at 14.25 GHz. The antenna has a cross-polarization level $<$-25 dB and -18 dB at broadside and 60° scan angle, respectively.

One of the factors contributing to the cross-polarization level is feed coupling between the V and H probes (Fig. 3.3b). The cross-polarization rejection (CPR) can be further improved by rotating the feed locations in the array. In this design, a 4-fold rotational symmetry (C4 symmetry) is used which is well covered in previous publications [12]. Overall, the antennas with C4 symmetry in a 2x2 sub-array provides a cancellation in both principal planes in cross-polarization caused by the coupling between the orthogonally polarized probe feeds.

2.2.3 Input-P$_{1dB}$ Improvement with the Embedded TX Driver

In order to operate each channel at its OP1dB of 11 dBm and with a chip gain of 23 dB, the Wilkinson divider network should provide -11 dBm ($IP1dB_{BF}$) at the input of every chip. The power at the 256-element array is divided to 64 chips using a 6-stage Wilkinson network with

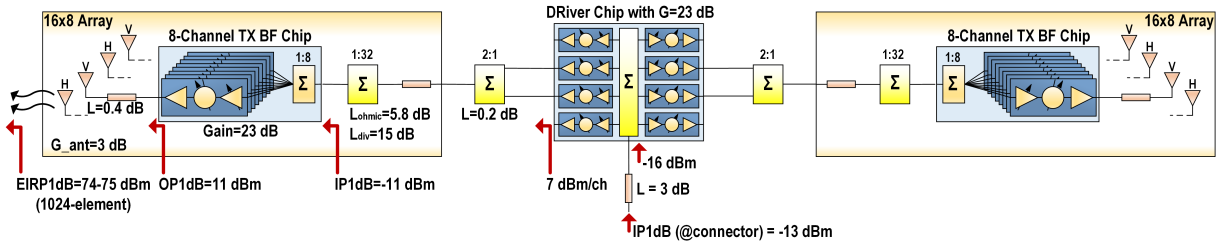

(a)

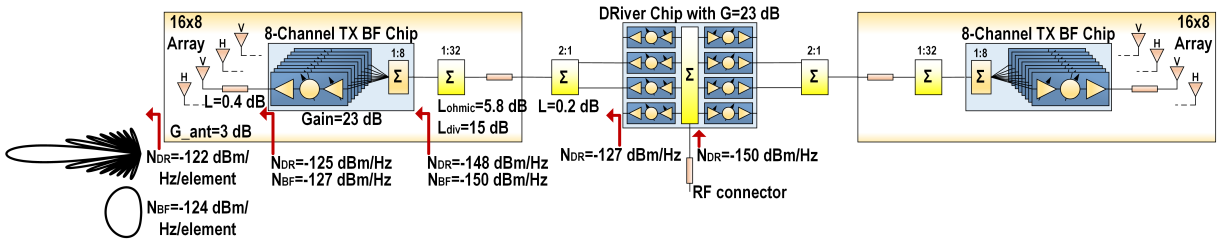

(b)

Figure 2.3: (a) The RF chain of the 256-element phased-array SATCOM transmitter with an embedded driver based on 8-channel TX beamformer chip with 8 channels. (b) Radiated in-band TX noise (N_{DR}: Noise due to driver chip, N_{BF}: Noise due to beamformer chip).

9 dB ohmic loss (L_{ohmic}) and a division loss (L_{div}) of 18 dB. The required array input P1dB is:

$$\begin{aligned} IP1dB_{PCB} &= IP1dB_{BF} + L_{ohmic} + L_{div} \\ &= -11\,dBm + 9\,dB + 18\,dB \\ &= 16\,dBm \end{aligned} \tag{2.3}$$

which is relatively high knowing that 4 sub-arrays need to be driven using an external Wilkinson and 14 GHz cables. Therefore, a transmit beamformer chip (Renesas F6501) is placed at the center of the 256-element array to greatly lower the input power requirements as shown in Fig. 2.3a. Also, two channels are combined together using a Wilkinson network for increased power and redundancy. The input-P1dB of the 256-element quadrant is reduced to -13 dBm at the RF coaxial port, and the transceiver output needs to be only $\sim$3 dBm to feed the 4 quadrant arrays (-13 dBm + 6 dB division loss, 3 dB cable loss and 6 dB headroom above P1dB).

One issue to consider with the embedded driver is the radiated noise from the 256-element

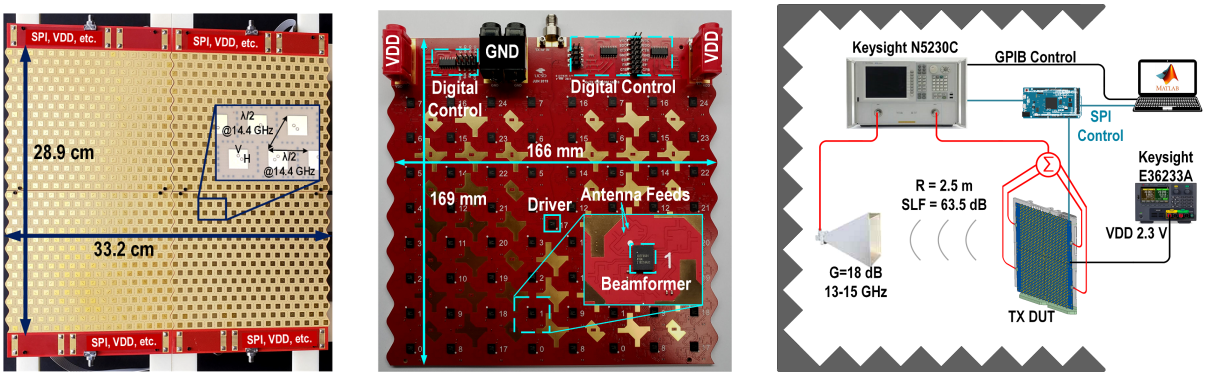

(a) (b) (c)

Figure 2.4: (a) Antenna side of 1024-element Ku-band SATCOM TX array. (b) Chip side of 256-element Ku-band SATCOM TX quadrant. (c) Calibration and measurement setup in an anechoic chamber.

sub-array. The output noise from the driver chip is -127 dBm/Hz per channel and this noise is distributed coherently to the 32 SiGe beamformer chips for half of the array with 21 dB loss (15 dB division loss and 6 dB ohmic loss). This results in a noise power of -148 dBm/Hz (N_{DR} in Fig. 2.3b) at the input of every chip, and an output noise of -125 dBm/Hz from every channel (Gain=23 dB). This coherent noise is comparable to the output noise of -127 dBm/Hz from each beamformer channel (N_{BF} in Fig. 2.3b), which adds up in space incoherently and is element pattern shaped. The difference between the coherent noise and the incoherent noise is that the coherent noise due to the driver will generate a 128-element array pattern and scan with the main beam. Still, knowing that the waveform bandwidth is 40-400 MHz, the equivalent coherent radiated noise is -36 dBm/channel, and is much lower than the radiated power of 10 dBm/channel. This shows that the driver output noise does not contribute to the array EVM and is much lower than the noise arising from the L-band up-converter placed at the common RF port (having a typical SNR of $\sim$40 dB).

2.3 Measurements

The 1024-element phased array was characterized in an anechoic chamber using a Keysight 5230C VNA and a horn antenna (Fig. 4.8a). The array consumes 164 W per polarization when all the V or H-channels are turned on at the P1dB level, and fans are used on the backside for air colling and kept the PCB temperature at $<55°$C. The array was controlled using an Arduino and MATLAB for the serial peripheral interface (SPI) commands. The array is measured at 1/4 far-field distance which is enough if the right calibration is done. Since $2D^2/\lambda$ is based on 22.5° quadrature phase error at the edges of the aperture, and there is around 90° phase error at 2.5 m distance, the calibration was applied to focus the beam at the horn antenna.

Although the array is designed as symmetrical as possible, there are still residual amplitude and phase errors among all the channels due to local transmission line length differences and Wilkinson divider inequalities. The calibration procedure includes two steps. First, the quadrants are calibrated, and the residual errors among the 256-element quadrants are compensated using the driver chips on each quadrant. For every quadrant, the individual channels were turned-on one by one to measure the S_{21} phase and amplitude using the setup in Fig. 4.8a. The phase and amplitude differences between the channels are then compensated by applying the necessary phase shifter settings. The residual errors for H-polarized channels are shown in Fig. 3.8b. The array has 0.65 dB rms amplitude error with 3.87° rms phase error after calibration. Similar results are obtained for V-polarized channels, and are not shown.

After calibration, the broadside frequency response was measured as shown in ig. 4.8b. The frequency response is centered at 13.5 GHz due to the frequency characteristics of the first generation chips (Renesas F6501), but the chip still operates very well at 14-14.5 GHz. Note that the frequency response has been re-centered in new-generation chips.

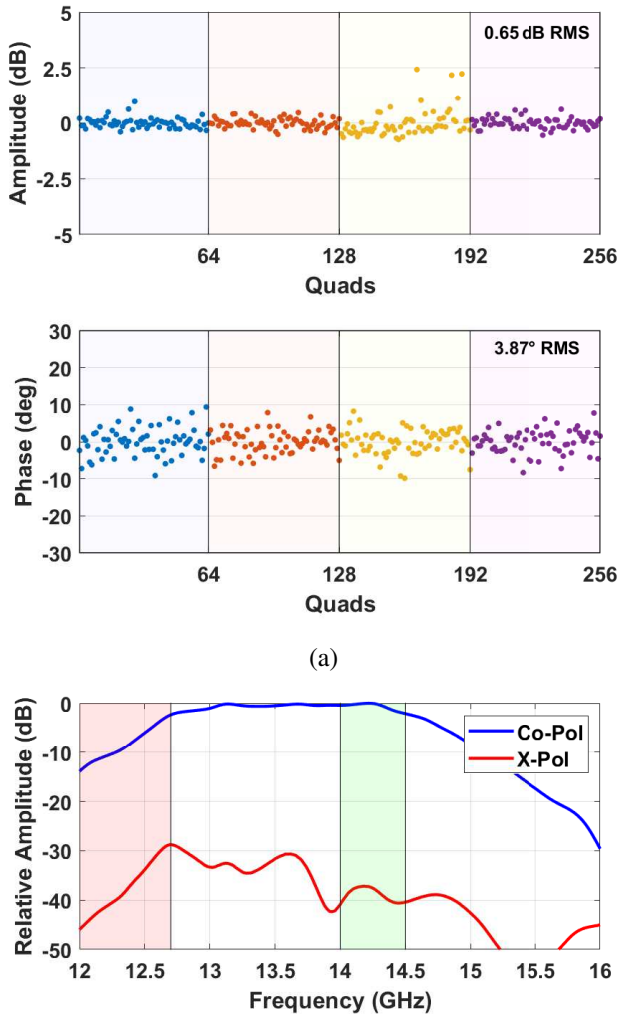

Figure 2.5: (a) Residual amplitude (0.65 dB rms) and phase (3.87° rms) errors of all 2x2 quads in H-polarized individual 256-element array quadrants (Quadrants are shown in different colors). (b) Measured frequency response at broadside for H-polarization. (V-polarization is similar due to symmetry).

2.3.1 Pattern Measurements

The co-and cross-polarization patterns were measured at 14, 14.25 and 14.5 GHz. The array results in >33 dB cross-polarization rejection at broadside across the Ku-band SATCOM transmit band for both uniform illumination and 6 dB cosine-taper amplitude distribution (Fig. 2.6, 2.7). The 6 dB cosine taper shows a first side lobe level (SLL) of -18 dB, and the half power beam width (HPBW) increases from 3.55° to 4.1° for the H-plane of the horizontally polarized

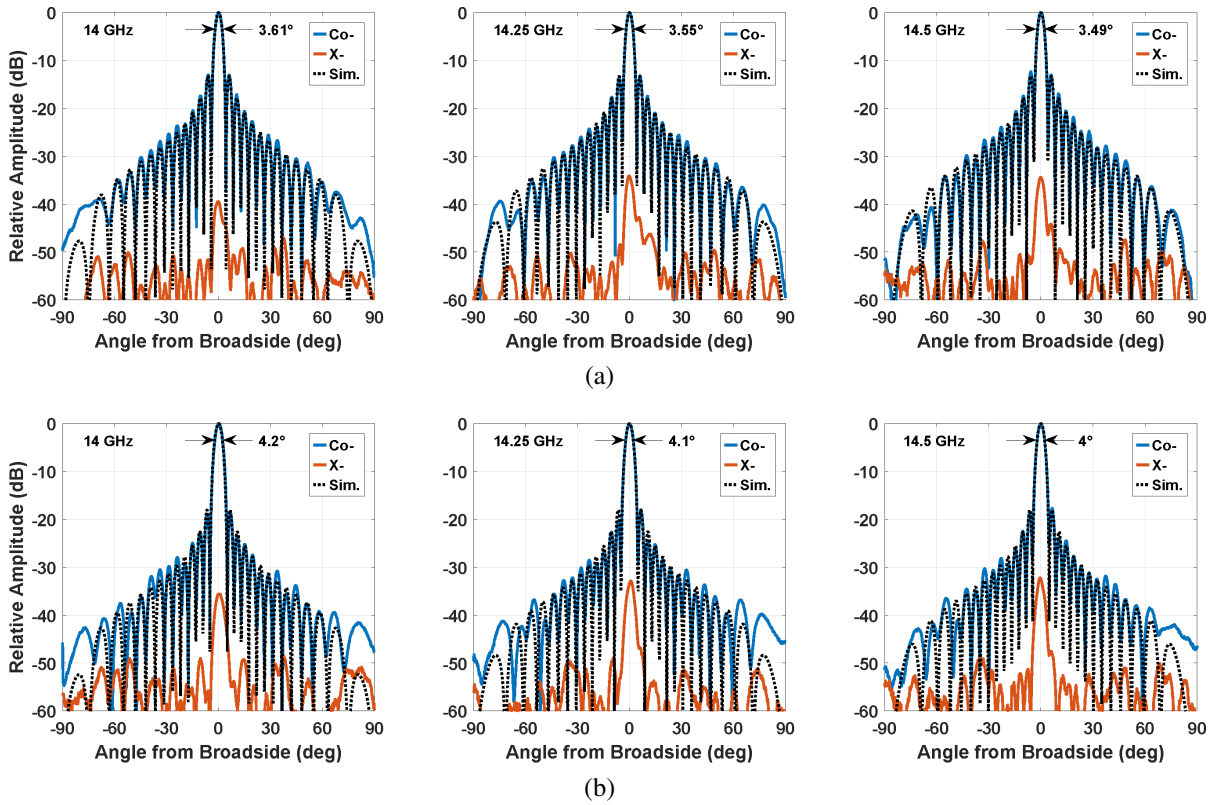

Figure 2.6: Measured co- and cross-polarization for the H-polarized antennas at 14, 14.25 and 14.5 GHz: (a) under uniform illumination, (b) under 6 dB cosine taper.

antennas. Lower side lobe levels can be achieved by applying more aggressive amplitude taper. The increase in the side lobe levels for the scanned beams shown in Fig. 2.8 results from the fact that no additional amplitude correction was applied to correct the phase shifter amplitude error at different scan angles (rms error=0.4 dB). Also, note that the array was measured at $R_{ff}/4$ which is not ideal for large scan angles. Still, the cross-polarization rejection is around 30 dB for the beam scanned to 60° off broadside due to the 2x2 feed rotation.

The array can easily scan up to ±75° while following a $cos\theta$ profile with a 3-dB drop at 60° scan angle (Fig. 2.8). Knowing that the scan loss involves the antenna impedance mismatch, these results verify the analysis in Fig. 2.2 with a well-matched antenna over wide scan angles. Also, under 7 dB cosine taper, the array is scanned in ±60° volume and shows a maximum of -18 dB side lobe level (Fig. 2.7b).

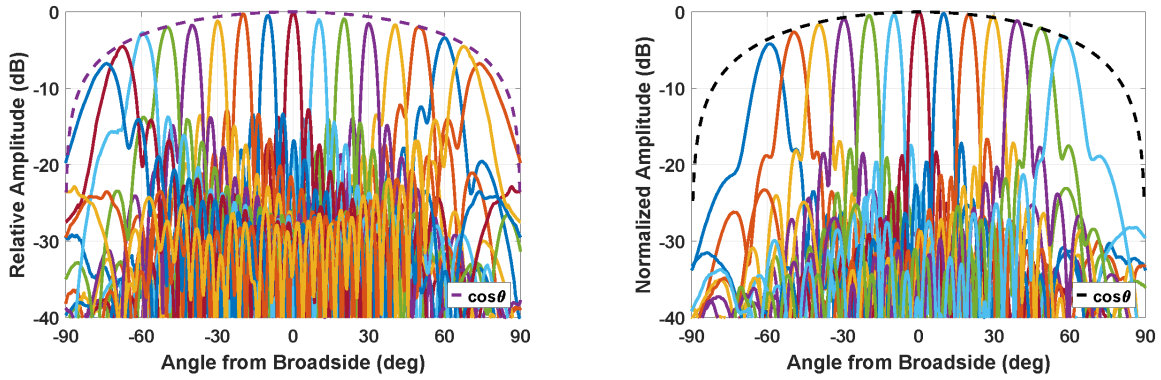

(a) (b)

Figure 2.7: Measured scanned beams at 14.25 GHz: (a) horizontally-polarized under uniform illumination, (b) vertically-polarized under 7 dB cosine taper.

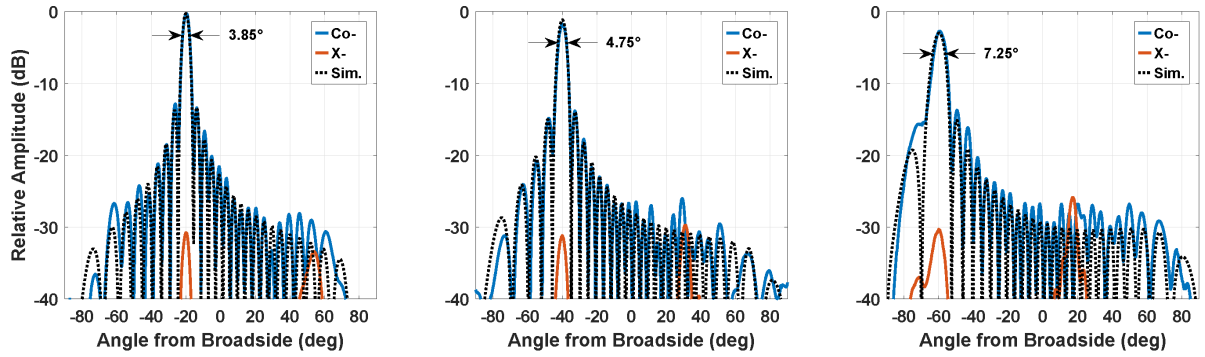

Figure 2.8: Measured co- and cross-polarized beams scanned to 20, 40 and 60° off broadside at 14.25 GHz. (uniform illumination)

The 1024-element array can synthesize rotated linear and circular polarizations with nearly identical patterns and cross-polarization levels. These are not included here for brevity as such measurements were extensively presented in [40] on a Ku-band array.

2.3.2 EIRP Measurements

The 1024-element array EIRP was measured one quadrant at a time in order to eliminate the errors due to the quarter far-field distance. The far-field distance of a quadrant is 2.64 m at 14.25 GHz, and the measurement distance is 2.5 m. Then, 12 dB is added to the measured average EIRP of the quadrants to obtain the 1024-element array EIRP since both the aperture area and

the transmit power are quadrupled (6 dB for the area, 6 dB for the transmit power). An EIRP of 74-75 dBm is achieved per polarization at the 1-dB compression point and Psat (P1dB+3 dB) at 14.1 GHz (Fig. 2.9). The $EIRP_{P1dB}$ is achieved when an RF power of -13 dBm is applied to a 256-element quadrant, and -2 dBm to the sum point at the L-band upconverter (5 dB cable loss and 6 dB division loss) (Fig. 2.3a). This results in a transmit gain ($EIRP/P_{in}$) of 76 dB (referring to the sum point) at 14.1 GHz. The measured EIRP agrees well with the simulated value of:

$$\begin{aligned} EIRP_{P1dB} &= 20log10(N) + G_{antenna} + P_{element} \\ &= 60\,dB + 3\,dB + 11\,dBm \\ &= 74\,dBm \end{aligned} \tag{2.4}$$

where,

$$G_{antenna} = D_{antenna} - Loss_{antenna+TL} = 3\,dB \tag{2.5}$$

where the directivity of a single antenna ($D_{antenna}$) is 4.1 dB at 14.1 GHz for 0.5x0.25$\sqrt{3}$ λ^2 aperture area, and the total loss is 1.1 dB, comprised of the antenna efficiency (0.6 dB), transmission line (TL) loss between the chip and the coaxial antenna input (0.4 dB), and the mismatch loss (0.1-0.2 dB). The drop in the directivity due to residual amplitude and phase errors after calibrations only 0.05 dB and is insignificant [32–36].

The EIRP was also measured on the V-pol. array and the results were within +/-0.3 dB of the H-pol. array (not shown). This means that the array can sustain a 45 dBW EIRP for a rotated linear polarization which is suitable for Ku-band SATCOM LEO and GEO systems. Also, the 1024-element array can radiate 48 dBW at Psat at broadside in circular polarization.

Finally, there is always the question of TTD in large arrays using phase shifters with constant-phase characteristics. Analysis in [40] indicates that 1024-element arrays at 14.25 GHz

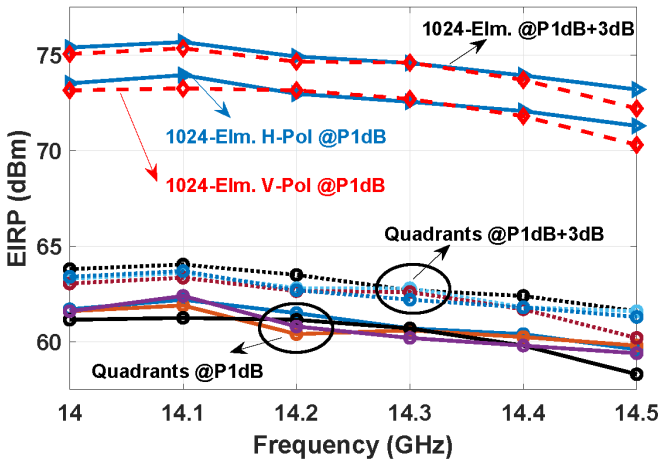

Figure 2.9: Measured EIRP at broadside versus frequency for H polarization. (V-Pol is similar)

can operate at an instantaneous bandwidth of 250 MHz with only a 0.1 dB drop in EIRP at 70° scan angles. Therefore, the 1024-element array does not require any TTD elements for pattern squint corrections.

2.4 Complex Waveform Measurements

2.4.1 Two-Tone Measurements of 2x2 Array

A 2x2 antenna test cell connected to a single beamformer chip is first measured to test the chip characteristics. The measured P_{out} vs. P_{in} curves at 14 GHz for 4 channels connected to the V-polarized antenna ports are shown in Fig. 2.10b, with the antenna gain, horn gain, space loss factor removed to show P_{out}. P_{in} is referenced to the chip input. It is seen that the 4 channels result in a small-signal gain of 23 dB$\pm$1 dB and an OP1dB of 11$\pm$1 dBm, and this could be due to the different channel characteristics and different antenna impedances (the antennas are not in an periodic 2-D environment). The 2x2 array P_{out}, as expected, is 6 dB higher than the individual channels and shows an averaging effect of the different channels.

A two-tone test was done at 14 GHz with a frequency separation of 50 MHz. The measured

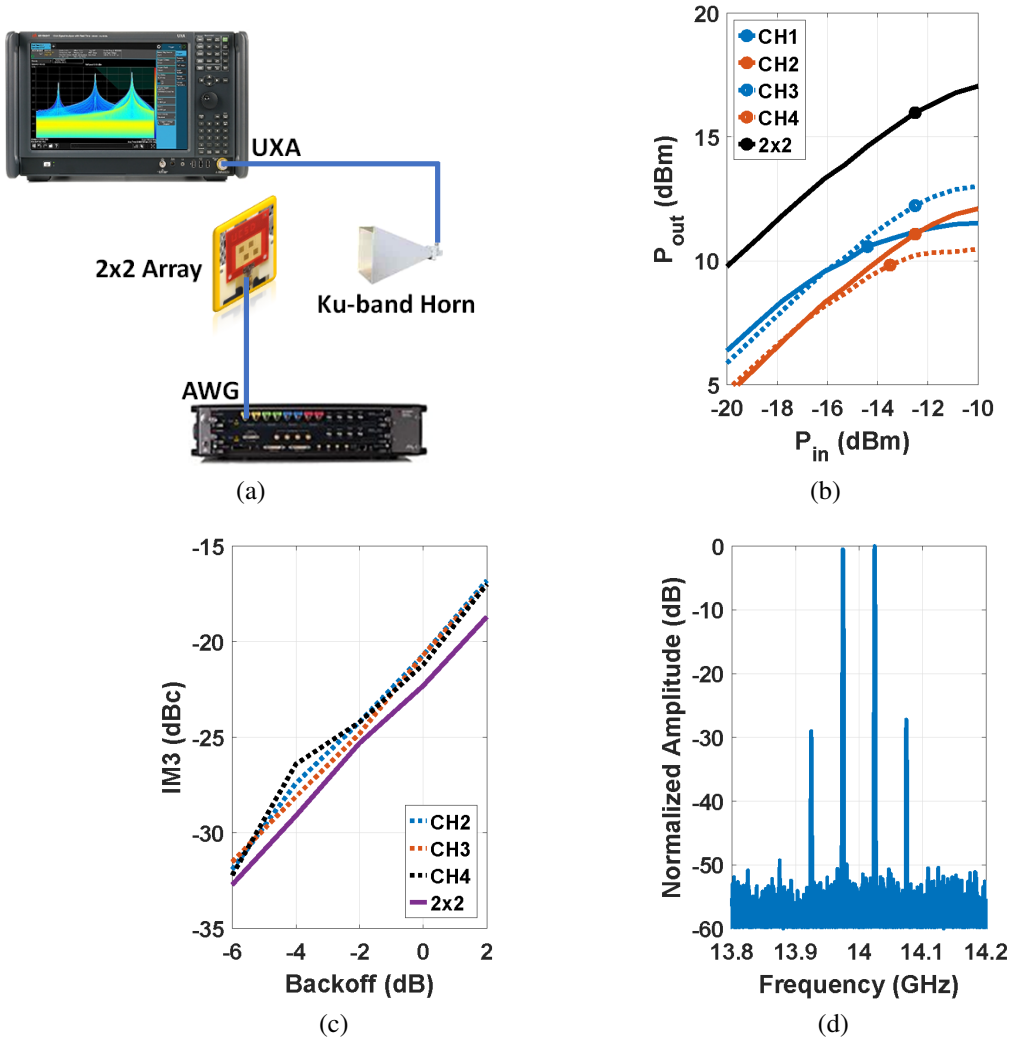

Figure 2.10: (a) Measurement setup of 2x2 TX array. (b) P_{in} vs. P_{out} curves of each channel (referenced to the beamformer input). (c) Measured IM3 levels of 2x2 TX array (50 MHz separation at 14 GHz) for individual channels and the 2x2 array for various backoff, (d) measured spectrum for the 2x2 array at 3 dB backoff from P1dB.

IM3 components vs. P_{in} for the individual channels and the 2x2 array are shown in Fig. 2.10c, and note that when all 4 channels are turned on together, the 2x2 array results in lower IM3 values. This is due to a better antenna impedance and also mutual coupling effects with the four PAs interacting with each other [39].

2.4.2 ACPR Simulation and Measurements

ACPR, which stands for Adjacent Channel Power Ratio, is defined as the ratio of the integrated power in the adjacent channel to the one in the main channel. It is a figure of merit how a communication system interferes with another one using the adjacent channel as its main channel. On the other hand, it means that some portion of the power which is expected to be in the main channel is spilt over to the next channel, resulting in a decrease in the efficiency due to the waste of the energy. Thus, in this section, the ACPR of the phased array is analyzed when complex waveforms are applied.

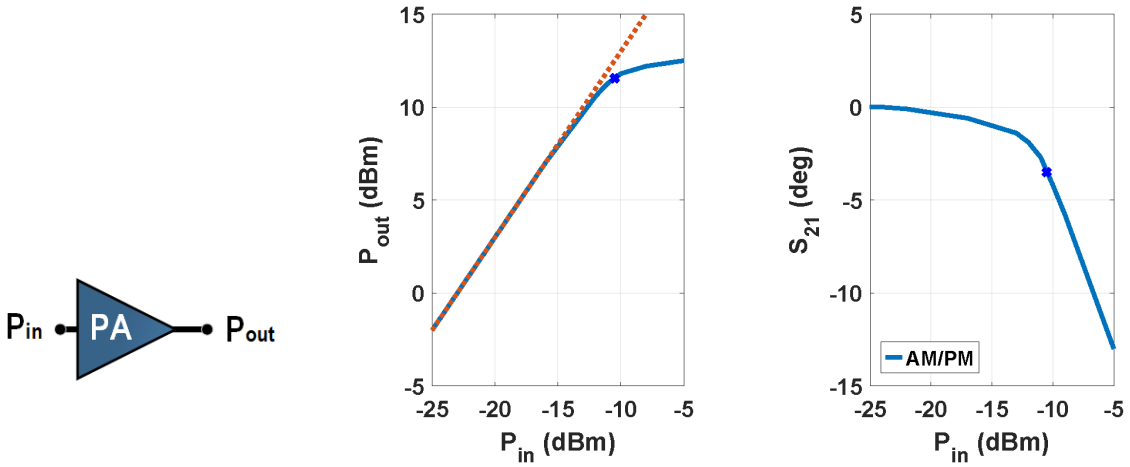

(a) (b) (c)

Figure 2.11: Single connectorized amplifier with the input P1dB of -11 dBm: (a) model, (b) AM-AM and (c) AM-PM characteristics. The dot indicates the P1dB point.

The P_{out} vs. P_{in} and AM-PM curves were first obtained by applying a single tone signal to a connectorized channel, (Fig. 2.11). Next, a single channel is modeled in MATLAB using the comm.MemorylessNonlinearity function with the lookup table of known AM-AM and AM-PM characteristics.

The QPSK and 8PSK waveforms with 100, 200 and 500 MBaud symbol rate centered at 14 GHz ($\alpha = 0.35$ and PAPR = 4 dB) are applied to the single amplifier model in MATLAB and measured on the 2x2 array. For the 2x2 array, two cases are investigated: a single channel is ON,

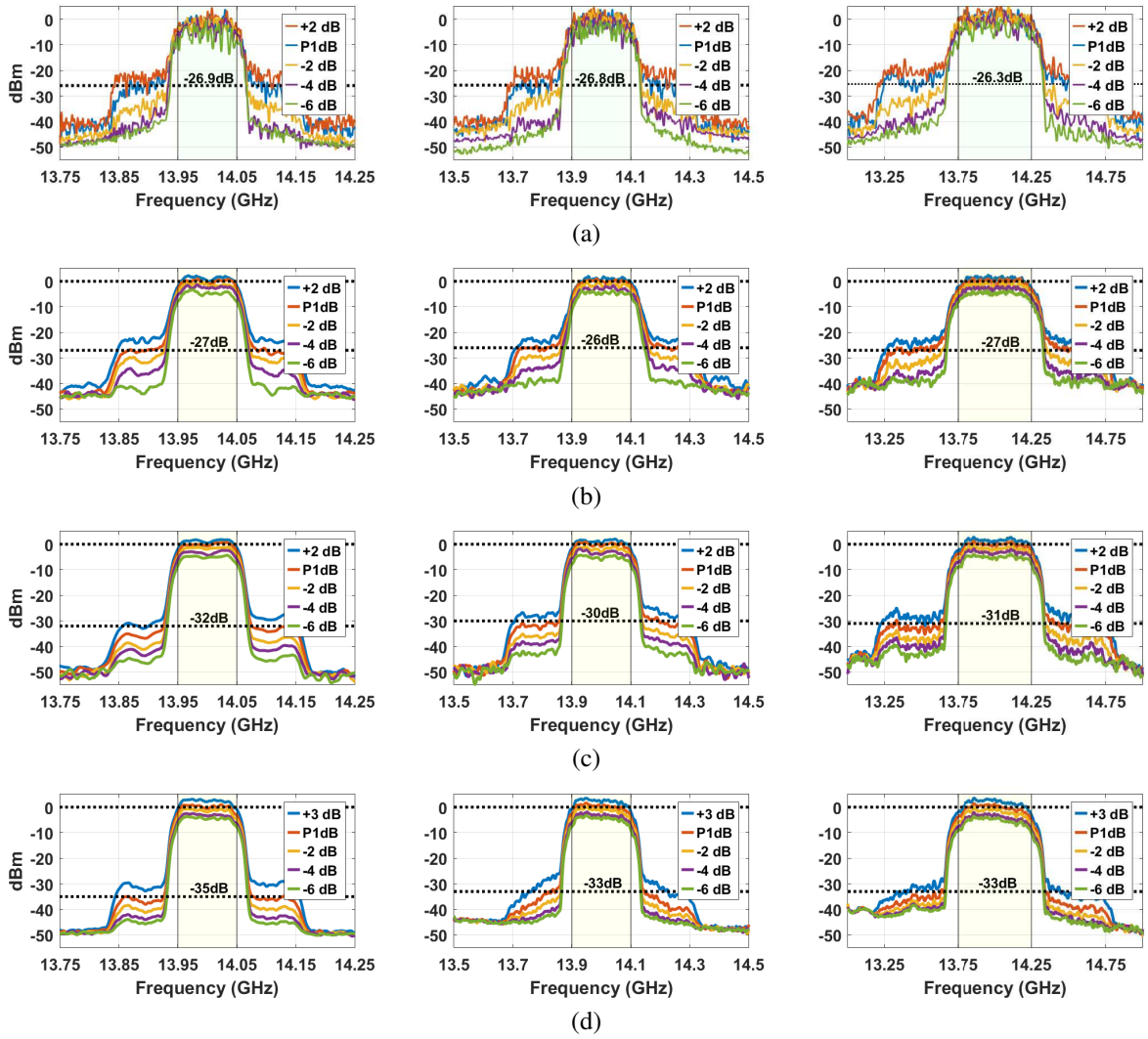

Figure 2.12: ACPR measurements for various backoff with 100, 200 and 500 MBaud QPSK waveforms: (a) Single channel MATLAB simulations, (b) Single channel measurements, (c) 2x2 measurements, (d) 1024-element array measurements.

and all four channels are ON. The measured ACPR of a single channel shown in Fig. 2.12b agree well with the simulated individual channel shown in Fig. 2.12a. However, when all four channels are energized in a 2x2 array, the ACPR at P1dB is seen to improve by $\sim$4 dB regardless of the modulation scheme or the symbol rate (Fig. 2.12c).

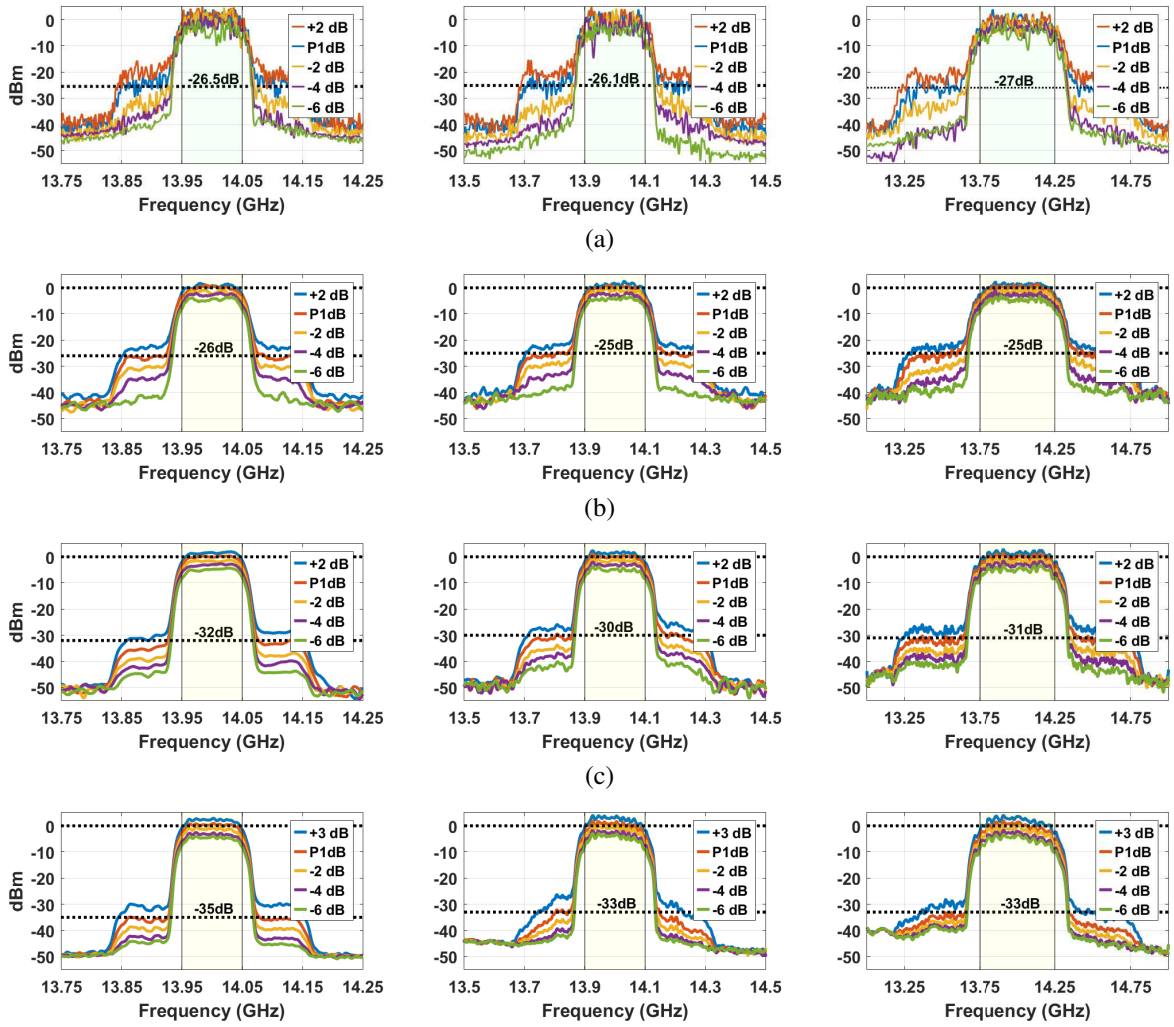

Figure 2.13: ACPR measurements for various backoff with 100, 200 and 500 MBaud 8PSK waveforms: (a) Single channel MATLAB simulations, (b) Single channel measurements, (c) 2x2 measurements, (d) 1024-element array measurements.

2.4.3 ACPR Measurements of 1024-Element Array

The same waveforms are also applied to the 1024-element transmit array (Fig. 2.12d). It is clearly seen that 1024-element achieves a better ACPR compared to the 2x2 array for all QPSK waveforms, and a much better one than the single channel. Again, this was observed before in [39] and further analysis is required to determine the reason for the ACPR improvement versus backoff for large arrays. The ACPR measurements were also done for 8PSK waveforms

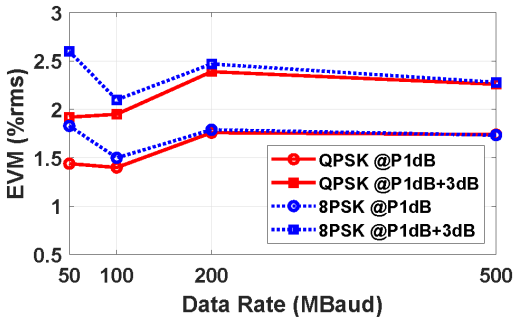

(a)

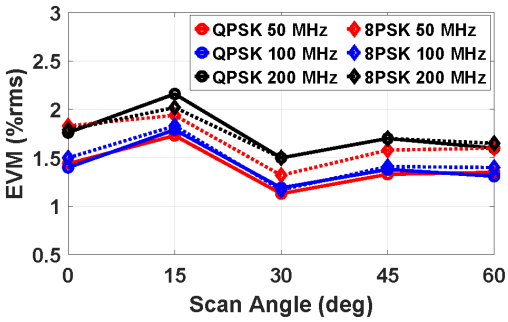

(b)

Constellations at $EIRP_{1dB}$				
Data Rate	50 MBaud	100 MBaud	200 MBaud	500 MBaud
QPSK				
EVM %rms	1.44%	1.40%	1.76%	1.74%
8PSK				
EVM %rms	1.83%	1.50%	1.79%	1.74%

(c)

Figure 2.14: (a) Measured EVM of the 1024-element array at broadside vs. data rate. (b) Measured EVM vs. scan angle at P1dB for QPSK and 8PSK waveforms with 50, 100 and 200 MHz modulation bandwidth. (c) Measured EVM and constellations vs. data rate using QPSK/8PSK waveforms at broadside for -2 dBm input power to the 1024-element phased array. Similar constellations are obtained at Psat.

and α=0.35 with a PAPR=4 dB, and similar results were achieved (Fig. 2.13). It is seen that the array can operate at P1dB and even Psat with very low ACPR (-29 to -30 dBc) for QPSK and 8PSK waveforms. This means that large phased-arrays do not need to be backed-off by 2-3 dB for linearization, which increases the usable EIRP of large phased-arrays and their efficiency.

2.4.4 EVM Measurements of 1024-Element Array

A Keysight M8195A Arbitrary Waveform Generator was used to synthesize various QPSK and 8PSK waveforms at a center frequency of 14 GHz. The signal received was transmitted

to the Keysight UXA N9040B Signal Analyzer, and demodulation is done using the Keysight VSA-89600 Vector Signal Analysis software. All reported EVM values are rms values (Fig. 15). The setup EVM was measured to be 0.8-1%. The EVM is dependent on several factors such as noise, linearity and bandwidth, but in this setup, it is mostly due to the AWG. The EVM_{setup} is removed from the measured EVM to obtain the true phased-array EVM using:

$$EVM_{array}(\%) = \sqrt{(EVM_{meas}(\%))^2 - (EVM_{setup}(\%))^2} \tag{2.6}$$

Fig. 2.14a and Fig. 2.14b present the measured EVM versus data rate and scan angle, respectively. The 1024-element array preforms remarkably well even at P1dB and P1dB+3 dB, with very low EVM and over all scan angles, and correlates well with the measured ACPR. This is further proof of the averaging factor of phased arrays and that large phased-arrays can be operated without any backoff. Fig. 2.14c presents the measured EVM and constellations for increasing data rates using QPSK and 8PSK waveforms centered at 14 GHz at EIRP_{1dB} at broadside for horizontal polarization.

Table I summarizes the performance of the 1024-element dual-polarized array and compares it with other state-of-the-art Ku-band SATCOM transmit phased-arrays.

2.5 Conclusion

A 14-14.5 GHz Ku-band 1024-element phased-array transmitter for mobile SATCOM ground terminals was presented with an EIRP of 44-45 dBW. The array can steer the beam in $\pm$75°cone with a cross-polarization rejection $>$33 dB at broadside and $>$30 dB at 60°scan angle due to the feed rotation in the 2x2 antenna cells. The array consumes 164 W per polarization, but the power drops to 100 W with the use of the Renesas second generation 8-channel SiGe beamformer chips (not available during the design phase of this project). The measured EVM is

Table 2.2: Comparison with State-of-the-Art Ku-band SATCOM Transmit Phased-Arrays

Parameter	This Work	[19] UCSD'18	[38]
Frequency (GHz)	14.0-14.5	13.0-14.6	14.0-14.5
Number of Elements	1024 (32x32)	256 (16x16)	1024 (16x64)
Antenna Type	Patch on PCB	Patch on PCB	WG Horn
Array Grid	Triangular	Rectangular	Rectangular
Polarization	Dual	Dual	Dual
Half-Power BeamWidth @14 GHz	3.6°	6.5°	-
Elevation Scan	150°($\pm$75°)	150°($\pm$75°)	90°(0°to 90°)
Azimuth Scan	150°($\pm$75°)	150°($\pm$75°)	Mechanical
Cross-Pol. Rejection (dB)	$>$33 (broadside)	$>$ 29 (broadside)	$>$40
Size (cm^2)	34x33.2	17x19	28x112
EIRP (dBW) @P1dB	44	34.5	53.5
ACPR (dB) @100MBaud 8PSK	-35	-33	-
Power per channel	165 mW	150 mW	-
Power per Polarization @P1dB	164 W	38.4 W	-

$<$2% for QPSK and 8PSK waveforms, with an ACPR of $<$-29 to -30 dB even at P1dB and Psat EIRP values. Also, the EVM remains below 2% up to 60° scan angles. This increases the array efficiency since a 2-3 dB backoff is not needed, and a phased-array can operate at P1dB or even Psat while still meeting SATCOM out-of-band requirements. The array design with chips on a single PCB results in an affordable solution for Ku-band SATCOM and in excellent performance at P1dB and Psat EIRP values.

2.6 Acknowledgment

The authors thank Renesas Electronics for providing the Ku-band SATCOM transmit beamformer chips, Kyocera International, San Diego, for the assembly of the phased-array boards in their state-of-the-art assembly line, Keysight for the measurement equipment and ADS software, and ANSYS for the HFSS full-wave EM simulation software. This work was supported by Renesas and Qualcomm.

Chapter 2, in part, is a reprint of the material as it appears in: G. Gultepe, S. Zihir, T. Kanar

and G. M. Rebeiz, "A Dual-Polarized 1024-Element Ku-band SATCOM Transmit Phased-Array with $\pm 70°$Scan and 43.5 dBW EIRP," *2020 IEEE/MTT-S International Microwave Symposium (IMS)*, Los Angeles, CA, USA, 2020, pp. 837-840, doi: 10.1109/IMS30576.2020.9223977. The dissertation author was the primary investigator and author of this paper.

Chapter 2, in full, is a reprint of the material as it may appear in: G. Gültepe, T. Kanar, S. Zihir and G. M. Rebeiz, "A 1024-Element Ku-Band SATCOM Phased-Array Transmitter with 45 dBW Single-Polarization EIRP", in *IEEE Transactions on Microwave Theory and Techniques*, accepted. The dissertation author was the primary investigator and author of this paper.

Chapter 3

A 1024-Element Ku-band SATCOM Dual-Polarized Receiver with $>$10 dB/K G/T and Embedded Transmit Rejection Filter

3.1 Introduction

Internet connectivity has become a necessity with the information age. Previously, the commercial market relied on fixed services for homes and businesses provided by geostationary (GEO) satellites [41]. The increase in the demand in ground, maritime, and airborne satellite-communications-on-the-move (SOTM) platforms and the launch of thousands of Low Earth Orbit (LEO) satellites have created a need for affordable ground terminals to track multiple satellites without sacrificing performance.

In the past, most of the SATCOM ground terminals were mechanically steered systems for SOTM applications [42–49]. Since they rely on motors, these terminals are bulky and require

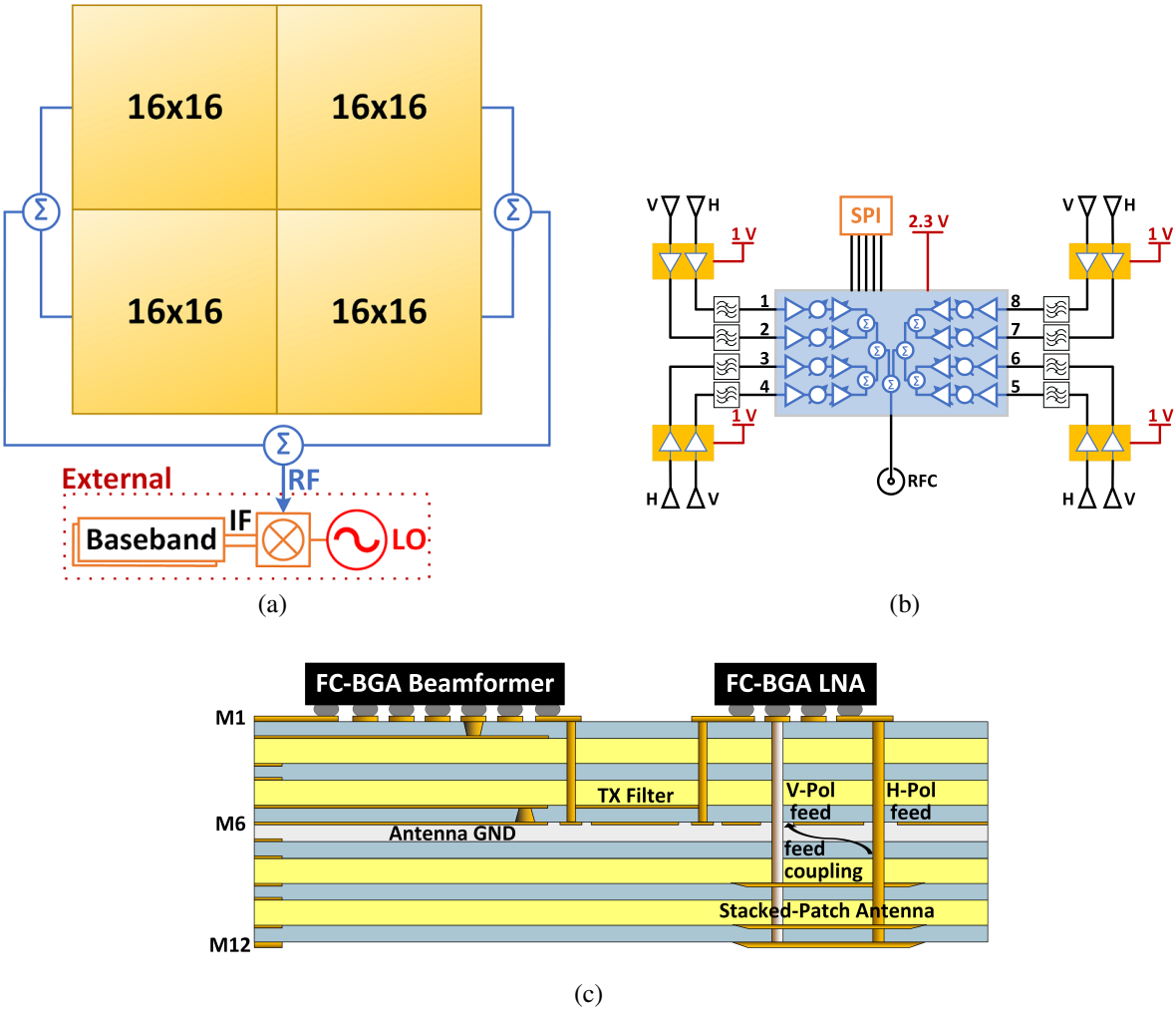

Figure 3.1: (a) A 1024-element dual-polarized SATCOM phased-array receiver based on 16x16 array tiles. (b) 2x2 antenna quad based on 8-channel RX beamformer chips and dual-channel LNAs with embedded transmit filters. (c) 12-layer PCB stackup.

extensive maintenance. They also have a keyhole problem unless they have a third axis of rotation [50]. Although phased-array antennas (PAA) offer a low-profile solution with accurate beam steering capabilities, they were only used in defense systems because of their high cost (Fig. 3.1) [51]. However, advances in silicon beamformer technologies have allowed for very low cost arrays, and these have been used in SATCOM and 5G systems [16–18, 20, 21, 24, 36, 52–58].

This paper expands on [57] and presents an affordable Ku-band receive SATCOM phased array, which incorporates 1024 dual-polarized patch antennas, dual-channel low noise amplifiers

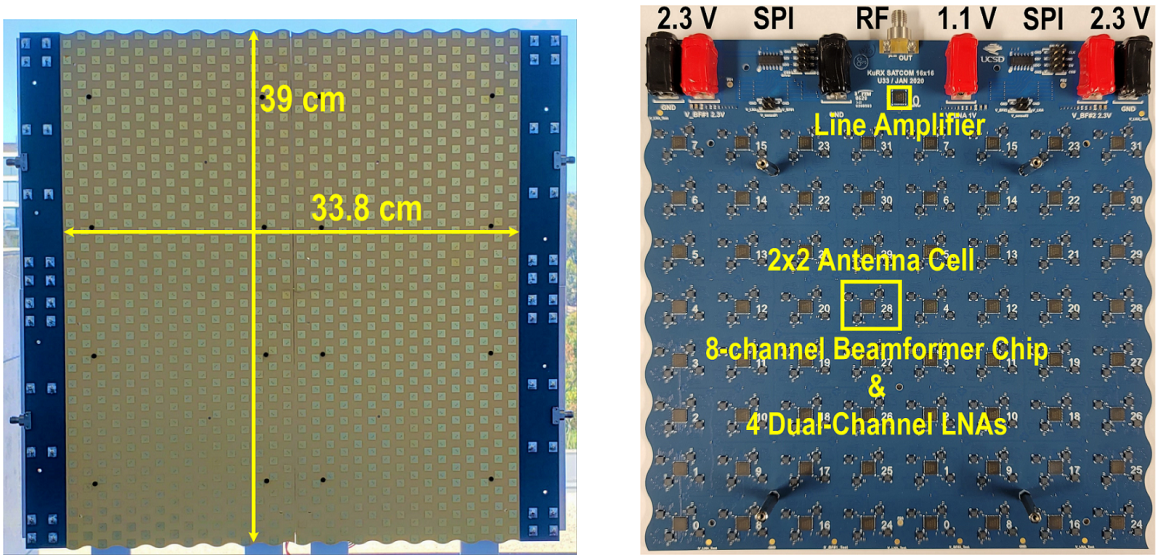

(a) (b)

Figure 3.2: (a) Antenna side of 1024-element Ku-band SATCOM RX array. (b) Component side of 256-element Ku-band SATCOM RX array quadrant.

(LNA), silicon beamformer chips assembled onto a cost-efficient PCB (Fig. 3.1). It further expands on [18] by presenting a 1024-element array with a wider scan range, which employs LNAs for increased G/T, and introduces an embedded filter for reduced transmit leakage.

3.2 1024-Element Phased-Array Design

The 1024-element phased-array is based on four 16x16 sub-array tiles (Fig. 3.2). These tiles are designed to be 2xN scalable by placing all the connectors, including RF, digital control and power, at one side of the PCB. The other sides are cut to follow the antenna boundaries to sustain an equilateral triangular grid. The four 256-element tiles are combined together using a 4:1 Wilkinson combiner, and the received signal is down-converted to IF or baseband and fed to a baseband processor. The use of separate LNAs and beamformer chips, when compared to beamformer chips with an embedded LNA, results in 0.25-0.3 dB lower transmission-line loss between the antenna feed and the LNA, and provides a 0.5-0.6 dB improvement in G/T (Fig.

4.1b). Therefore, one can build a phased array with the same G/T but 10-14% less antennas and chips when external LNAs are used. Also, this design allows for an embedded filter with a notch response in the 14-14.5 GHz transmit band to be placed between the LNA and the beamformer chip so as to avoid beamformer chip saturation. This allows the RX and TX arrays to operate under a shared radome with the RX array being able to handle reflections from the radome at the transmit frequencies.

The 64 beamformer chips in each sub-array are controlled using a standard 4-wire SPI interface with CLK (clock), CS (chip select), SI (signal in) and SO (signal out). Placing SPI drivers (buffers) at the edge of the board, the associated capacitance with the long SPI routings are driven without any issues at 10-50 MHz.

3.2.1 Antenna Design

The array is manufactured using a cost-efficient Panasonic Megtron-6 substrate (ε_r=3.63 and tanδ=0.004 at 12 GHz), and incorporates a 12-layer stack-up (Fig. 4.1c). M1-M6 layers are used for RF routing, power (DC) and SPI routing, and a stacked-patch antenna is placed on M6-M12 layers.

A 3-stack probe-fed dual-polarized square patch antenna is placed on M9 layer and the parasitic patches are placed on M11 and M12, with M6 layer as the antenna ground. Short transmission-line matching networks connect the dual-polarized antenna feed to a dual-channel SiGe low-noise amplifier (LNA), which minimizes the loss before the LNA and improves the array G/T.

The antenna grid is equilateral triangular for better scan performance. The antennas are spaced at $\lambda/2$ at 12.2 GHz to scan to $\pm 70^\circ$ without any grating lobes throughout the antenna bandwidth (10.7-12.7 GHz). The grid size of 480$\times$ 416 mil (D_x=0.5λ and D_y=0.25$\sqrt{3}\lambda$ @ 12.2 GHz)

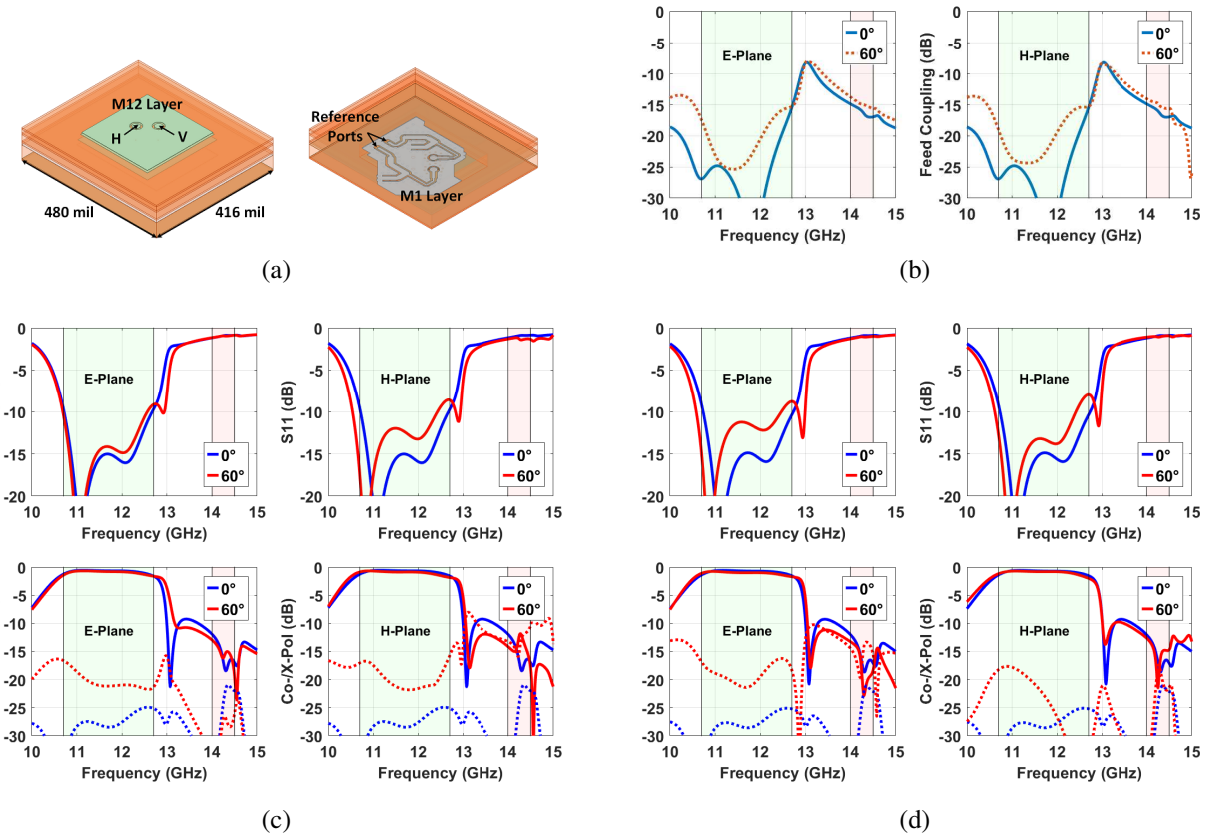

Figure 3.3: (a) 10.7-12.7 GHz antenna model. Simulated S_{11}, co-pol and cross-pol vs. scan angle (0°, 60°) at the reference port: (b) Feed coupling vs. scan angle, (c) H-Pol antenna (d) V-pol antenna.

results in an element directivity of 3.1, 3.9 and 4.6 dB at 10.7, 11.7 and 12.7 GHz, respectively.

$$D_{element} = \frac{4\pi D_x D_y}{\lambda^2_{@11.7\,GHz}} = 3.9\,dB \tag{3.1}$$

The 1024-elemnent array achieves a directivity of 33.2, 34 and 34.7 dB at 10.7, 11.7 and 12.7 GHz, respectively.

The dual-polarized antenna is simulated in Ansys HFSS, imposing master and slave boundaries to assume an infinite array in the desired equilateral triangular grid and terminating the radiation surface with a Floquet port to observe the radiation efficiency in both co- and cross-polarized radiation planes when the antenna is excited from the reference ports, the LNA inputs (Fig. 3.3a). A 1 mm sheet of polystyrene (ε_r=2.6) is used as a wide angle impedance

matching (WAIM) sheet above the PCB to improve the transmission of the antenna in its H-plane by 1 dB when the beam is steered to $\pm 60^\circ$ off broadside at 12-12.7 GHz.

Simulated transmission and reflection coefficients of the horizontally-polarized antenna are shown in Figure 3.3c. The reference ports in Figure 3.3a are the LNA input bumps. It does not show scan blindness at any scan angle (TM_0 onset). The antenna has an S_{11} <-9 dB up to $\pm 60^\circ$ scan angle in both E- and H-planes at 10.7-12.7 GHz. Compared to "in-array" antennas, the edge antennas always have a slightly different performance and a slightly different S_{11}. However, this is tolerable for large arrays. This is because an array with a size larger than $5\lambda \times 5\lambda$ (10×10 array with 0.5λ spacing) can be simulated as an infinite array [59].

The cross-polarization level is <-25 dB at broadside and rises to -17 dB at $\pm 60^\circ$ scan angles. The antenna loss at broadside is 0.6-0.7 dB at 11.7 GHz and includes ohmic loss, dielectric loss and the short transmission-line matching network loss. The loss increases to 0.8 and 1.1 dB at 10.7 GHz and 12.7 GHz due the relatively high S_{11} of $\sim$-12 dB. Note that the antenna transmission response is -12 to -15 dB at 14-14.5 GHz, which helps to protect the LNA from saturation due to transmit signal leakage. The vertically polarized antenna shows similar characteristics due to the symmetrically-fed square patches (Fig. 3.3d).

One of the limiting factors in the cross-polarization level, especially when the antenna is scanned to wide angles, is the V- and H-probes' coupling. Therefore, 2x2 sub-array feed-rotation method is applied to reduce the cross-polarization level, and the feed locations in the 2x2 cell are mirrored around the center point of the sub-array. This leads to the cancellation of the cross-polarized magnetic currents on the non-radiating edges within the 2x2 cell in the principal planes [24].

3.2.2 LNA and RX Beamformer

Each dual-polarized antenna element is connected to a commercial dual-channel LNA (Renesas F6921) with a gain of 19 dB and a noise figure (NF) of 1.5-1.6 dB at 11 GHz, and

Table 3.1: RX SiGe Beamformer and LNA Summary

Parameter	Unit	F6101 BF	F6921 LNA
Frequency	GHz	10.7-12.75	10.7-12.75
No. of Channels	-	8	2
Package	-	QFN	FC-BGA
Typical Gain	dB	15.5	19
Noise Figure	dB	5.5	1.5-1.6
IP_{1dB}	dBm	-23	-23
Phase Shifter (PS)	bit	6	-
PS Phase Step	degree	5.625	-
PS Phase Error	degree rms	2.5	-
VGA	bit	6	-
VGA Step	dB	0.45	-
VGA Gain Control	dB	16	-
VGA Gain Error	dB rms	0.25	-
Power/channel	mW	55	15
Supply Voltage	V	2.3	0.9-1.1

consuming 15 mW per channel at 1.1 V. The LNA gain drops to only 15 dB at 14 GHz, and is therefore still high in the transmit band. The LNA input 1-dB compression point (IP1dB) is -23 and -19 dBm at 11.7 and 14 GHz, respectively.

The 2x2 LNA outputs are fed to a commercial 8-channel SiGe beamformer chip (Renesas F6101) with a single-port output (Fig. 4.1b). Each channel has a 6-bit phase shifter with a phase-step of 5.625° steps. It also has two variable gain amplifiers (VGA) with a linear attenuation range of 0-16 dB. The SiGe beamformer has an electronic gain of 15.5 dB at 11.7 GHz with a NF of 5.5 dB and an IP1dB of -23 dBm. The definition of the electronic gain is S_{21}+9 dB when only one channel is energized and all the others are terminated. The 9 dB compensates for the additional Wilkinson loss which does not exist when all channels are powered up. The electronic gain drops to 9.5 dB at 14.25 GHz in the transmit band with an IP1dB of -20 dBm. This chip consumes 55 mW per channel at 2.3 V, but newer generations (F6121S) consume only 35 mW per channel.

The combined LNA and SiGe beamformer have a total electronic gain and NF of 34.5 dB

and 1.66 dB at 11.7 GHz, and with an IP1dB of -44 dBm at 11.7 GHz and -37 dBm at 14 GHz referenced to the LNA input. Note that the IP1dB is determined by the SiGe beamformer chip since the LNA can handle -19 dBm at 14 GHz.

3.2.3 Transmit-Leakage and Embedded Transmit Filter

The 1024-element RX array will be mounted on a platform near a 1024-element phased-array transmitter such as the one described in [16]. As the TX/RX array pair will probably share the same radome, the transmit array will most likely saturate the receive beamformers during simultaneous transmit/receive operation. This can be analyzed using the LNA and beamformer described above (Fig. 3.4a).

The average coupling between a transmit and receive antenna is around -60 dB in large arrays with few wavelengths separation between the TX and RX apertures, including the receive antenna response, reflections from the radome and near-field coupling. Since every transmit antenna can radiate up to 10 dBm, the transmit signal available at the receive antenna port is -50 dBm. However, a receive antenna at the phased-array edge, located close to the transmit array, will capture electromagnetic fields generated by $>$100 transmit antennas in the worse case scenario. This increases the transmit leakage by $>$20 dB, and the total transmit signal impinging on each LNA input is -30 dBm. Since the LNA IP1dB is -19 dBm at 14 GHz, the LNA operates at 11 dB back-off and in linear mode. However, the transmit signal is amplified by the LNA and becomes -15 dBm at the beamformer input thus saturating the beamformer chip. It is therefore necessary to insert a low-pass filter between the LNA and beamformer to suppress the transmit leakage by at least 15-20 dB.

A low-pass filter can also be placed between the antenna and the LNA, but the 1 dB in-band filter loss will increase the NF by 1 dB and reduce the G/T by 2 dB, and is not acceptable. Instead, if the filter is placed after the LNA, the filter in-band loss will not affect the system NF due to high LNA gain, and will prevent the beamformer from being saturated by the transmit-leakage.

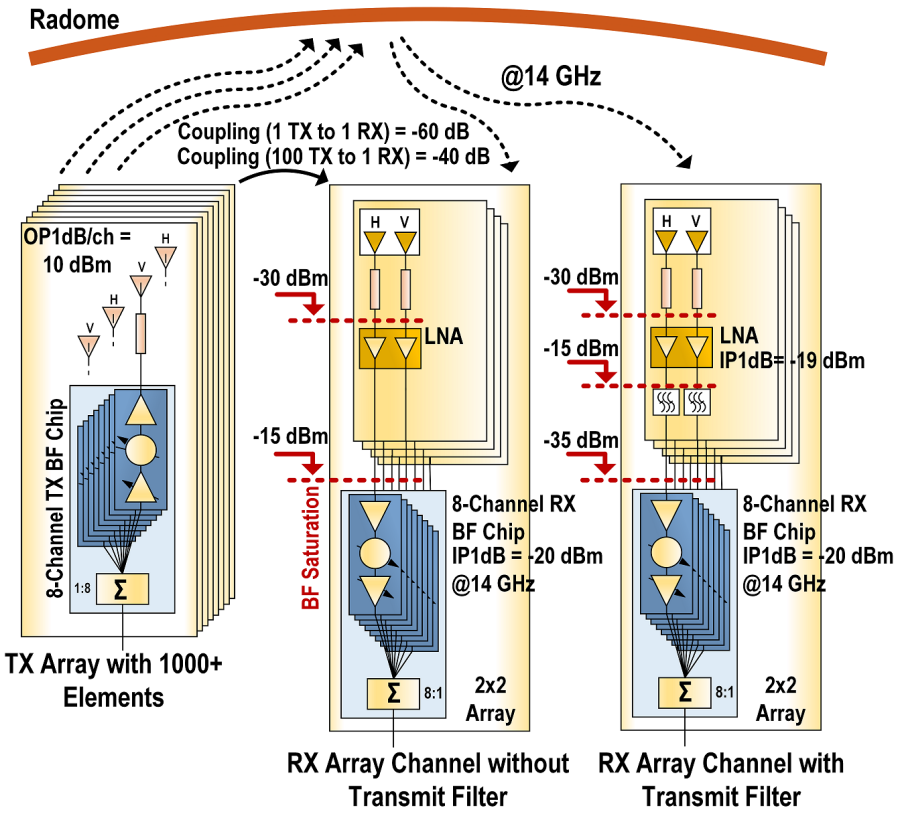

(a)

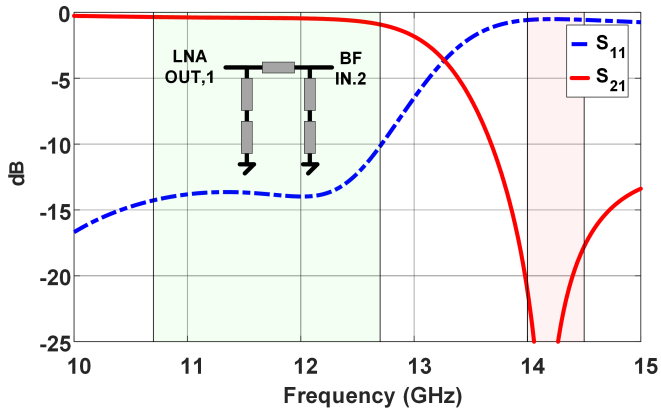

(b)

Figure 3.4: (a) Transmit leakage analysis when TX and RX arrays are placed side by side and shared a radome. (b) Embedded filter response.

A third-order elliptic low-pass filter with two LC-stubs is placed between the LNA and SiGe beamformer. Due to the lack of space on the M1 layer and the physical size of the filter, it is implemented on the M5 layer in a stripline mode. The low-pass filter is designed with

S_{11}<-10 dB, an in-band loss <1 dB at 10.7-12.7 GHz, and with a transmit signal rejection of 20-25 dB at 14-14.5 GHz (Figure 3.4b). The simulations, referenced to the LNA output and the beamformer input on M1 layer, include the effect of the RF transitions between M1 and M5 layers.

3.2.4 Connectorized Channel Test Board

An RF board with connectors is first used to measure the channel gain and NF (Fig. 3.5a). A dual-channel LNA is connected to beamfomer channels 2 and 3 on the left side through the embedded transmit filter. Similarly, another LNA is connected to channels 6 and 7 using a short 50 Ω transmission line on the right side (Fig. 3.5b). The line loss between the RF connectors and the LNA ports are de-embedded out of the measurements. The channel electronic gain (G_{ch}) is:

$$\begin{aligned} G_{ch} &= G_{LNA} - L_{LPF} + G_{BF} \\ &= 19 - 0.7 + 15.5 \\ &= 33.8\,dB \end{aligned} \tag{3.2}$$

LNA gain can also be 21 dB if biased at a higher current level, resulting in a channel gain of ∼36 dB. Measurements with and without a filter show a filter response having <1 dB loss at 12.7 GHz and with 25 dB suppression at 14 GHz. The channel NF is measured using the Keysight PNA-X and is 1.68 dB at 11.7 GHz (Fig. 4.5d). This agrees well with the simulated NF of 1.66 dB, given by:

$$\begin{aligned} F_{ch} &= F_{LNA} + \frac{L_{LPF} - 1}{G_{LNA}} + \frac{F_{BF} - 1}{G_{LNA}/L_{LPF}} \\ &= 1.47\,(NF_{ch} = 1.66\,dB) \end{aligned} \tag{3.3}$$

and knowing that there is a ±0.1 dB error in the NF measurements. The filter has no effect on the channel NF in the receive band as its in-band loss is <1 dB, and it is after the LNA gain of 20 dB.

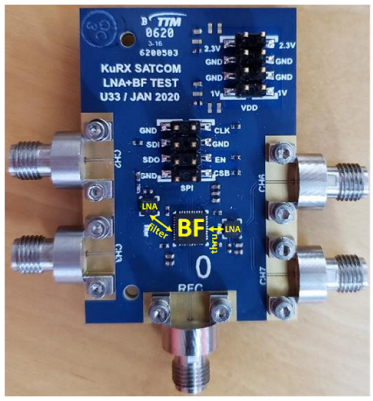

(a)

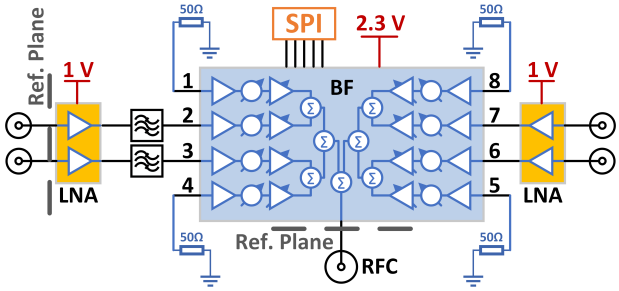

(b)

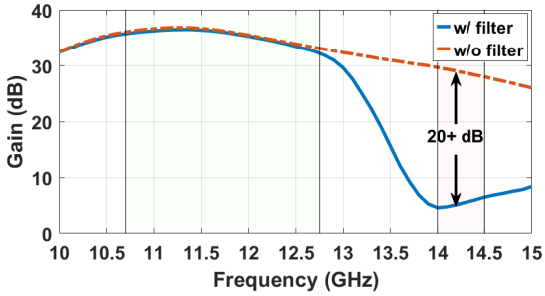

(c)

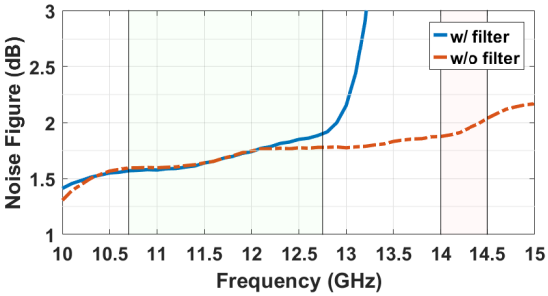

(d)

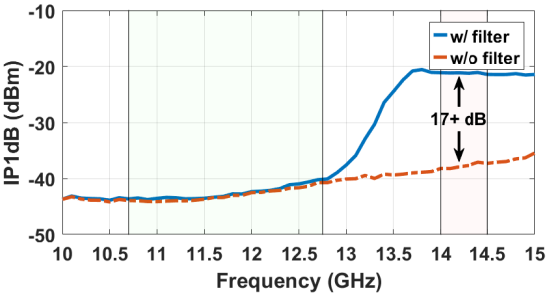

(e)

Figure 3.5: (a) PCB and (b) Schematic of the connectorized channel test board. (c) Gain, (d) NF and (e) IP1dB of an RF channel with and without the transmit filter between the LNA and a beamformer channel.

Finally, the measured IP1dB for the LNA and beamformer with and without the filter shows a 17-18 dB improvement, as expected (Fig. 4.5e).

3.2.5 Wilkinson Combiner Network

The signals received by the 256-element antennas are combined using a 6-stage Wilkinson combiner network. The Wilkinson combiner is implemented on the M1 layer with a ground plane on M2, and employs 0201 packaged 100 Ω isolation resistors on M1. The Wilkinson combiner loss is 0.2-0.3 dB, with a simulated isolation and return loss of >20 dB at 10.7-12.7 GHz. The 6-stage Wilkinson combiner network has a total ohmic loss of 9 dB.

A RX beamformer chip is placed at the edge of a 256-element sub-array tile to boost the received signal before the RF output connector, and acts as a line amplifier with amplitude and phase control (Fig. 3.6b). A Wilkinson divider is inserted before the line amplifier to use two beamformer channels on the PCB. By doing so, the line amplifier will remain functional in case one channel fails. Since only 2 beamformer channels are excited with the others terminated, the line amplifier results in an electronic gain of 9.5 dB instead of 15.5 dB due to the 6 dB excess loss in the on-chip Wilkinson network (the other channels are not energized).

3.2.6 Receiver Noise Figure and G/T

The RX electronic gain and NF (NF_{rec}) of the entire 1024-element array are calculated using Fig. 3.6b:

$$\begin{aligned} G_{RX_{electronic}} &= G_{ch} - L_{WN} + G_{LA} - L_{conn} \\ &= 35 - 9 + 9.5 - 5 \\ &= \sim 30\,dB \end{aligned} \tag{3.4}$$

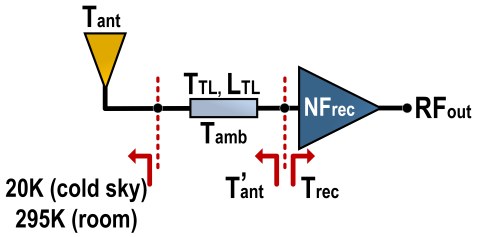

(a)

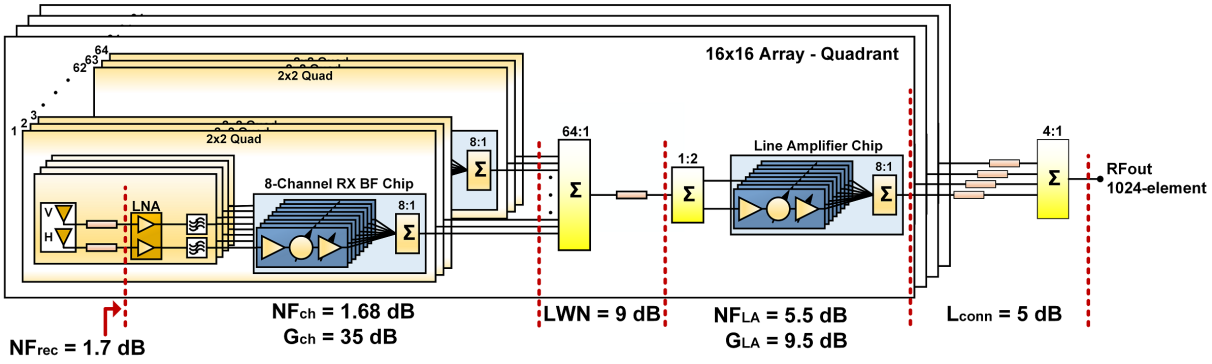

(b)

Figure 3.6: (a) RF chain for G/T calculation. Simulated (b) RF chain of the 1024-element array consisting of 4 sub-array tiles based on 8-channel RX beamformer chips and dual-channel LNAs.

$$F_{rec} = F_{ch} + \frac{L_{WN} - 1}{G_{ch}} + \frac{F_{LA} - 1}{G_{ch}/L_{WN}} + \frac{L_{conn} - 1}{G_{ch}G_{LA}/L_{WN}}$$
$$= 1.48\,(NF_{rec} = 1.7\,dB) \tag{3.5}$$

where G_{ch} and F_{ch} are the measured channel gain and NF (Fig. 4.5c and 4.5d). L_{WN} accounts for the 6-stage Wilkinson network loss, and F_{LA} and G_{LA} denote the NF and gain of the beamformer chip used as a line amplifier. L_{conn} includes loss of the external 4:1 Wilkinson combiner and cables which bring together the four 256-element quadrants.

A 1024-element array is modeled in MATLAB^{TM} to predict NF_{rec} and G/T versus frequency (Fig. 7). The G/T is a figure-of-merit for a satellite system to calculate the carrier-to-noise density (C/N) and signal-to-noise (SNR) ratios for the link budget analysis. The G/T of the array is calculated when the antenna looks at the cold sky during satellite reception (T_{ant}=20 K)

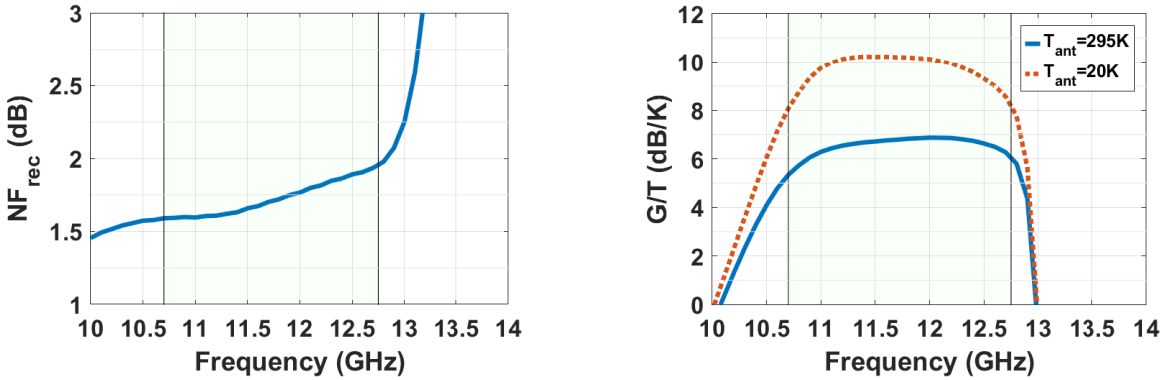

(a) (b)

Figure 3.7: Simulated (a) receiver NF and (b) G/T of the 1024-element array.

and when it is in an anechoic chamber at room temperature for measurements (T_{ant}=295 K).

The antenna gain-to-noise temperature (G/T) is defined as:

$$G/T = G_{ant} - 10\log_{10}(T_S) \tag{3.6}$$

where G_{ant} denotes the array antenna gain including the antenna dielectric, metal and transmission-line loss L_{TL} before the LNA and the matching and cross-polarization losses (ML) when the antenna is connected to the LNA.

$$G_{ant} = 10\log_{10}(1024) + (D_{ant_{elm}} - L_{TL} - ML) \tag{3.7}$$

where $D_{ant_{elm}}$ is the directivity of a single antenna element defined by the unit cell area and the frequency of reception. For instance, at 11.7 GHz, the array antenna gain (G_{ant}) is:

$$\begin{aligned} G_{ant} &= 10\log_{10}(1024) + (D_{ant_{elm}} - L_{TL} - ML) \\ &= 30.1 + (3.9 - 0.6 - 0.2) \\ &= 33.2\,dB \end{aligned} \tag{3.8}$$

The receiving system noise temperature (T_S) is a combination of the antenna noise temperature (T_{ant}), the transmission-line output noise temperature (T_{TL}) and the effective input noise temperature of the receiver (T_{rec}).

$$T_S = T_{ant}^{'} + T_{rec} \tag{3.9}$$

$$T_{ant}^{'} = T_{ant}/L_{TL} + T_{TL} \tag{3.10}$$

$$T_{TL} = T_{amb}\,(1 - 1/L_{TL}) \tag{3.11}$$

$$T_{rec} = T_0(F_{rec} - 1) \tag{3.12}$$

where T_0=290 K and T_{amb}=295 K are the reference temperature for the noise figure measurement and the ambient temperature of the lossy elements of the line, respectively. When all the values are substituted into (4.7), the receiving system noise temperature (T_S) is calculated as for T_{ant}=20 K:

$$\begin{aligned} T_S &= T_{ant}/L_{TL} + T_{TL} + T_{rec} \\ &= (20\,(10^{\frac{-0.6}{10}}) + 295\,(1 - 10^{\frac{-0.6}{10}})) + 139.2 \\ &= 194.7\,K \end{aligned} \tag{3.13}$$

If (4.6) and (4.10) are substituted into (4.4), G/T for T_{ant}=20 K:

$$\begin{aligned} G/T &= 33.2 - 10\log_{10}(194.7) \\ &= 10.3\,dB/K \end{aligned} \tag{3.14}$$

3.3 Measurements

All measurements were performed in an anechoic chamber using a Keysight N5245B PNA-X Microwave Network Analyzer and a Ku-band horn antenna (Fig. 4.8a). The measurement

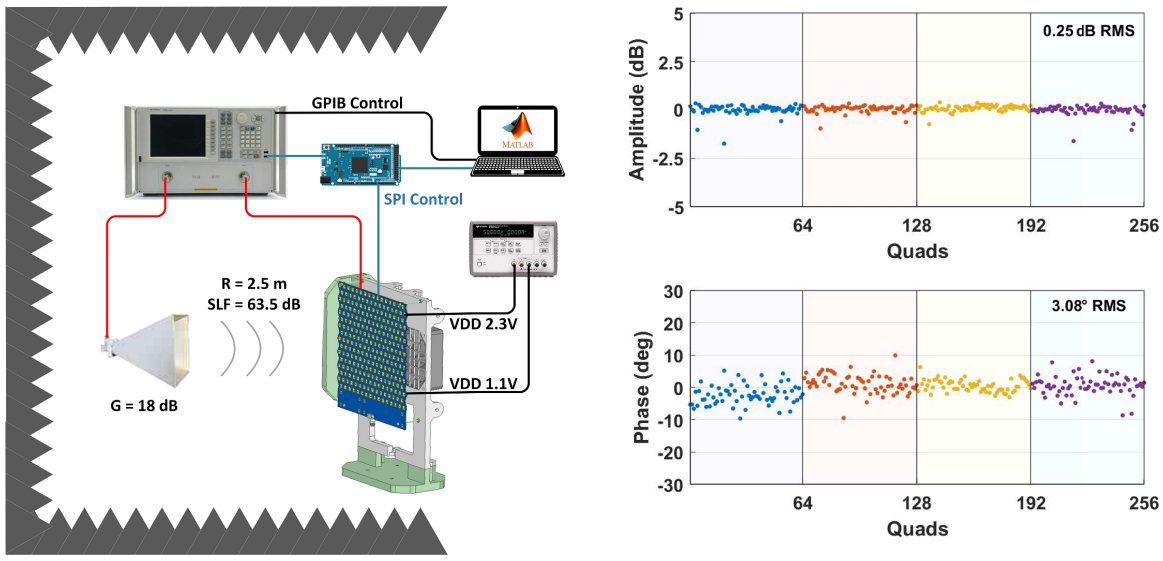

(a) (b)

Figure 3.8: (a) Calibration and measurement setup in an anechoic chamber. (b) Residual amplitude (0.25 dB rms) and phase (3.08° rms) errors of all 2x2 quads in 1024-element array after calibration at 11.7 GHz. (Quadrants are shown in different colors.)

distance was 2.5 m. Since the far-field distance ($2D^2/\lambda$) is $\sim$12 m, the measurements were taken in the radiating mid-field by focusing the beam to the horn antenna to get rid of the added quadrature phase error. For the 1024-element array, the beamformer chips consume 56 W per polarization while the LNAs require 15 W per polarization. Therefore, the 1024-element array consumes at most 142 W for dual-polarized reception (70 mW/channel). Small fans are mounted on the back side of the array during operation. The measured temperature is 40$\pm$5°C across the entire array.

3.3.1 Calibration

The calibration was performed in 2 steps. First, the S_{21} of the received signal, transmitted from the horn antenna, was recorded by turning on only one channel at a time, which takes $\sim$10 ms per element. The difference between the channels was calibrated out using the phase shifter of each channel. The amplitudes were then equalized by applying the necessary VGA

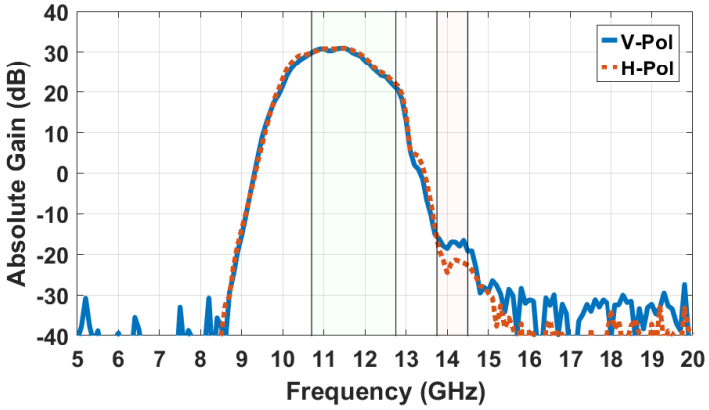

Figure 3.9: Frequency response of the 1024-element RX array. Ku-band SATCOM RX (10.7-12.7 GHz) and TX (14-14.5 GHz) bandwidths are shaded in green and red, respectively.

settings of each beamformer chip. Then, the line amplifiers were used to balance the average phase and gain level of the four 256-element quadrants. Since only one channel is energized at a time, the mutual coupling effects are not compensated.

Fig. 3.8b presents the residual amplitude and phase errors after the calibration described above. The H-polarized channels has 0.25 dB rms amplitude and 3.08° rms phase errors. The residual rms errors are similar for the V-polarized channels, and not shown for brevity.

3.3.2 Frequency Response

Fig. 4.8b presents the measured S_{21} response for the V and H-polarization between the horn antenna and the RF common port, with the horn gain and space-loss factor normalized out. The array electronic gain is 30 dB at 11.7 GHz as predicted by (4) and drops by ∼9 dB at 12.7 GHz due to 4-5 dB decrease in the channel gain (LNA, filter, beamformer) as shown in Fig. 4.5c, coupled with another 2 dB drop in the line amplifier gain and a 1 dB additional Wilkinson network loss. The transmit band at 14-14.5 GHz is rejected by ∼50 dB as compared to the RX band response. This is due to the antenna response (13-17 dB suppression), gain drop in the LNA (4 dB), filter rejection (20-25 dB), gain decrease in the beamformer and line amplifier (5-7 dB each), and additional Wilkinson network loss (2 dB) at 14 GHz.

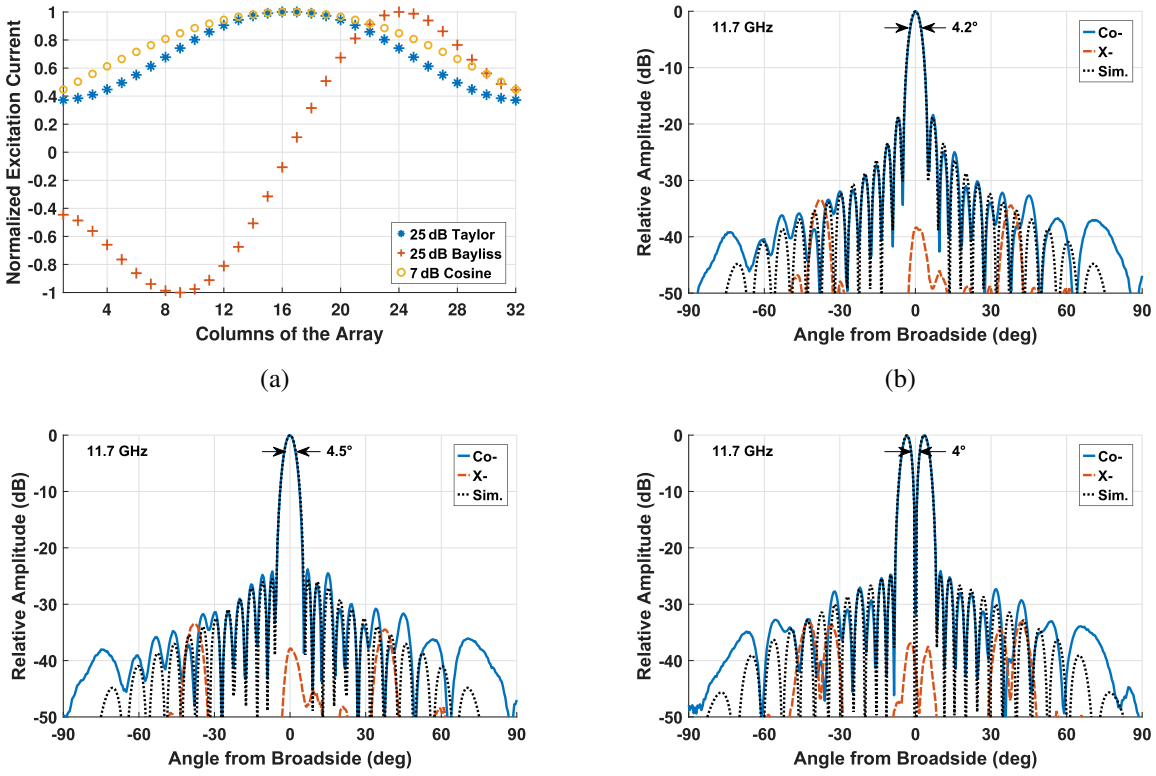

Figure 3.10: (a) Normalized currents applied to the 1024-element RX array for 7 dB Cosine and 25 dB Taylor and Bayliss amplitude distributions. Measured co- and cross-pol. of the 1024-element RX array under (b) 7 dB Cosine, (c) 25 dB Taylor and (d) 25 dB Bayliss amplitude taper.

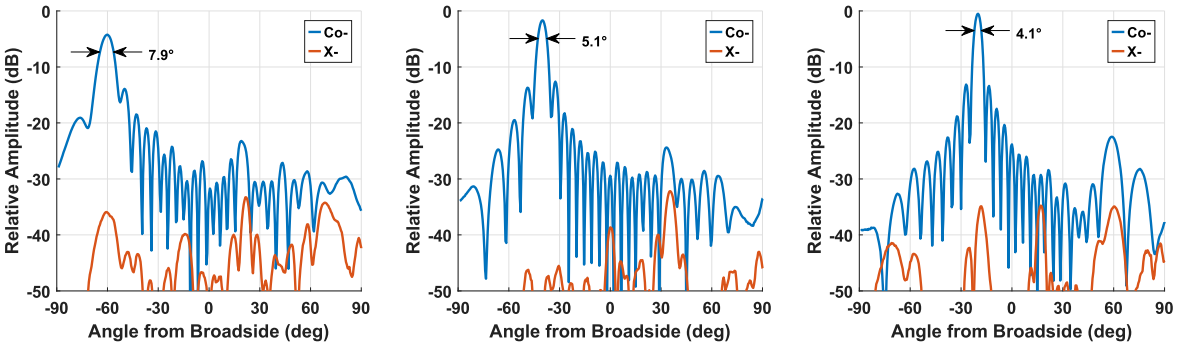

Figure 3.11: Measured co- and cross-polarized beams scanned to 20, 40 and 60° off broadside at 11.7 GHz. (uniform illumination)

3.3.3 Pattern Measurements

Fig. 3.10a presents the normalized current distributions for 7 dB cosine (-19 dB side lobe level, SLL), 25 dB Taylor amplitude taper for sum beams and 25 dB Bayliss amplitude and phase

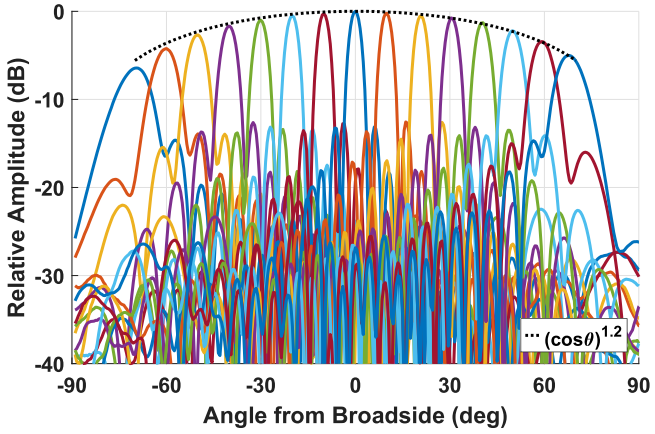

(a)

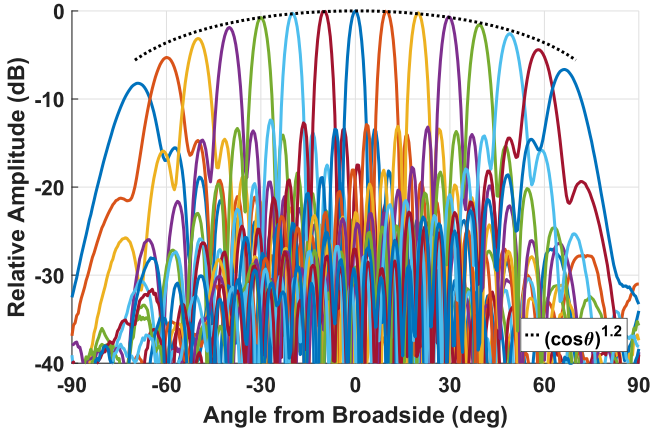

(b)

Figure 3.12: Measured patterns vs. scan angle at 11.7 GHz under uniform illumnitaion: (a) E-Plane, (b) H-Plane.

distribution to generate a difference pattern for monopulse operation. The measured patterns agree well with the simulated patterns for all three cases. Half-power beam widths for the 7 dB cosine and 25 dB Taylor amplitude tapers are 4.2° and 4.5°, respectively, compared to 3.83° for uniform illumination (-13 dB SLL) at 11.7 GHz at broadside:

$$\begin{aligned} HPBW_{azimuth} &= 50.76^{\circ}\left(\frac{\lambda}{L\cos(\phi_{scan})}\right) \\ &= 3.83^{\circ} \end{aligned} \tag{3.15}$$

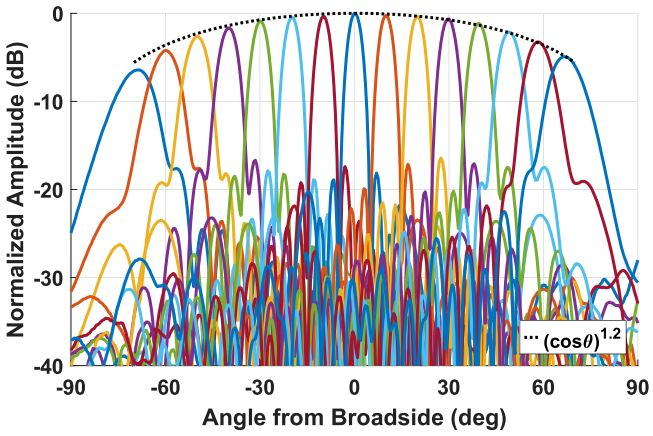

Figure 3.13: Measured E-plane patterns vs. scan angle at 11.7 GHz under 7 dB cosine taper.

The cross-polarization level is very low and is -39 dB for both sum patterns with -19 dB and -25 dB SLL.

Fig. 3.11 presents the measured co- and cross-polarized beams steered to 20°, 40° and 60° off broadside with beam widths of 4.1°, 5.1° and 7.9°, respectively, under uniform illumination. The increase in the 3-dB beam width follows $1/\cos(\phi_{scan})$ in (3.15). The array achieves a cross-polarization rejection of >35 dB even for 60° scan angle. The increase in the SLL around the grating lobe location is due to the non-ideal phase shifter characteristics, namely phase shifter amplitude error. To steer the beam, only an progressive phase shift was applied to each element on top of the broadside calibration at 11.7 GHz, and the resultant amplitude error was not corrected (phase shifter rms amplitude error = 1 dB).

The array can scan to ±70° in H-pol. E-plane (Fig. 3.12a) and V-pol. H-plane (Fig. 3.12b) under uniform illumination. The scanned patterns has a $\cos(\theta_{scan})^{1.2}$ roll-off with 3.6 dB drop at 60° scan angle. At wide scan angles in the H-plane, there is a bit more gain drop, and this is because the WAIM sheet was not used during measurements.

The main beam was also scanned with a 7 dB cosine amplitude distribution is applied to lower the SLL (Fig. 3.13). As the gain drop vs. scan angle follows a $\cos(\theta_{scan})^{1.2}$ curve, and the SLL remains below -17 dB.

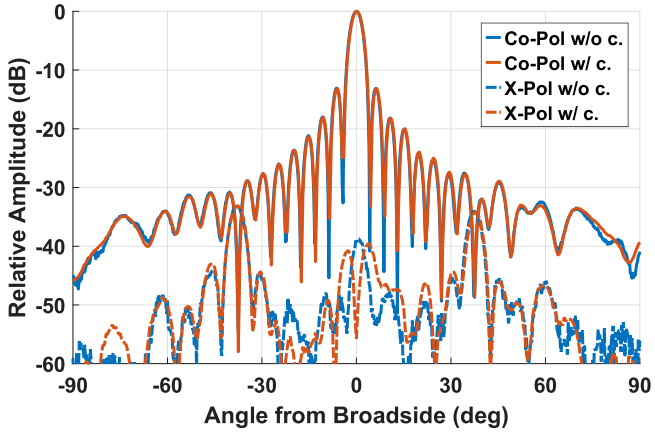

Figure 3.14: Measured co- (V-pol.) and cross-pol. (H-pol.) of the 1024-element RX array before and after cross-polarization cancellation technique is applied at 11.7 GHz.

3.3.4 Patterns and Cross-Polarization

As the array has individual V- and H-polarized channels with 0.2-0.3 dB gain and 5.625° phase resolution, it is possible to synthesize +45° slant, -45° slant left-hand or right-hand circular polarizations by setting the phase difference between the V- and H-polarized channels to 0°, 180°, 90° or -90°, respectively. The slant-linear and circular polarized patterns are identical to Fig. 3.10 and are not shown for brevity (details of such patterns have been extensively shown in [61]).

The polarization purity can be also improved by balancing the gain of the orthogonally-polarized channels. An example is shown in Fig. 3.14 where the cross-polarization was reduced from -39 dB to -56 dB using gain and phase balancing between the V and H-channels. Note that the array itself results in excellent cross-polarization response without tuning over all scan angles meeting SATCOM requirements (-23 dB), and this is shown here for completeness.

3.3.5 Antenna Gain-to-Noise-Temperature

The G/T of the 1024-element array was measured using the setup in Fig. 4.8a with a Keysight PNA-X G/T software module. During the measurements in the anechoic chamber, the antenna temperature (T_{ant}) was the room temperature, 295 K, as the array was facing towards a

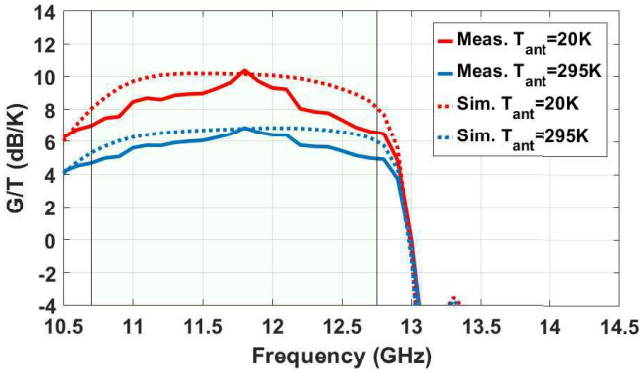

(a)

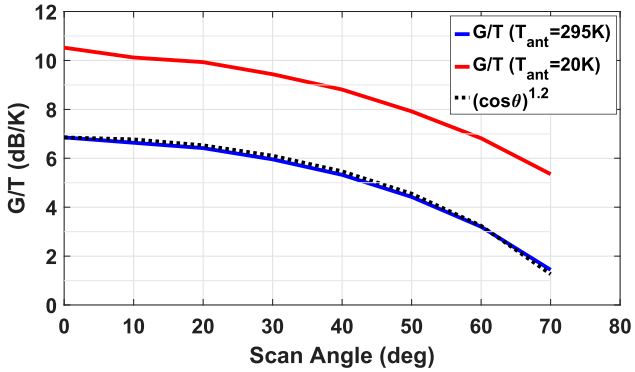

(b)

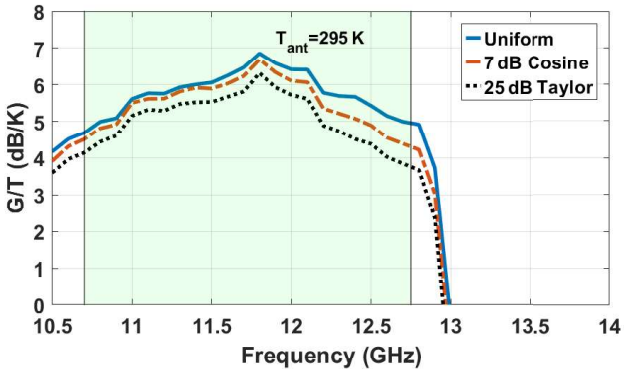

(c)

Figure 3.15: (a) Measured G/T at broadside when T_{ant}=295 K and its correspondance when the array looks at the cold sky (T_{ant}=20 K). (b) Measured G/T vs. scan angle (T_{ant}=295 K) at 11.8 GHz. (c) Measured G/T under uniform illumination, 7 dB cosine and 25 dB Taylor amplitude distribution at broadside when T_{ant}=295 K.

Ku-band horn antenna. Then, the G/T is calculated for the case in which the array looks at the cold sky (T_{ant}= 20 K) during satellite reception. The G/T improves by:

$$G/T_{imp} = \frac{T_S}{T_S - (295-20)/L_{TL}} \tag{3.16}$$

where L_{TL} denotes the total loss before the LNA. Fig. 3.15a presents the measured G/T when T_{ant}=295 K and its correspondence for T_{ant}=20 K. The 1024-element array with a directivity of 34 dB (and a gain of 33.2 dB) achieves a G/T of 10.5 dB/K around the calibration frequency of 11.7 GHz, and agrees well with simulations. The decrease in G/T at 12.7 GHz is mainly due to the embedded transmit filters with an aggressive response. As there are 8 filters with different shapes in a 2x2 cell, and the corner frequency of some of them may have shifted a bit to lower frequencies. In the future, a less aggressive filter with a rejection of 15 dB may be a better choice. The decline in G/T at 10.7 GHz is mostly due to the antenna impedance bandwidth. It is important to note again that the array is calibrated at 11.7 GHz, and needs to be calibrated again at 10.7 and 12.7 GHz since the 2x2 sub-arrays have unequal line lengths and filter routings. Still, the measured G/T when T_{ant}=295 K only drops by 1 dB at 12.7 GHz even if the array electronic gain drops by 9 dB due to the high LNA gain. The measured G/T versus scan angle follows the $\cos(\theta_{scan})^{1.2}$ response observed during the pattern measurements (Fig. 3.15b).

The G/T is also measured when an amplitude taper is applied to lower the SLL. Fig. 3.15c presents the measurements under uniform illumination, 7 dB cosine and 25 dB Taylor amplitude taper. Compared to the case under uniform illumination at 11.7 GHz, the G/T under 7 dB cosine and 25 dB Taylor amplitude distributions drop by 0.2 dB and 0.6 dB, respectively. Since the directivity decreases theoretically by 0.4 and 0.8 dB for these two aperture taper distributions, the measurements are within 0.2 dB and consistent. As the LNAs are closer to the antenna terminals, and the LNA gain is fixed, the attenuation applied to the VGAs in the beamformers to achieve the tapered distributions does not increase the system NF and therefore has no effect on the G/T. It is

Table 3.2: Comparison with State-of-the-Art Ku-band SATCOM Phased-Array Receivers

Parameter	This Work	[18] UCSD 2018	[60] 2017	[55] 2013
Frequency (GHz)	10.7-12.7	10.6-12.5	10.7-12.7	10.7-12.75
No. of Elements	1024 (32x32)	256 (16x16)	256 (16x16)	156
Antenna Type	Patch (PCB)	Patch (PCB)	Patch (PCB)	Patch (PCB)
Array Grid	Triangular	Rectangular	Rectangular	Triangular
Polarization	Dual-Linear	Dual-Linear	Linear	Dual-Linear
HPBW @11.7 GHz	3.83°	6.7°	-	-
Elevation Scan	140°(±70°)	140°(±70°)	Fixed at 23°	140°(±70°)
Azimuth Scan	140°(±70°)	140°(±70°)	40°(±20°)	140°(±70°)
X-Pol. Reject. (dB)	>35	>23	>20	>17
Size (cm^2)	39x34	22.2x19.7	25x37	$\pi\times11^2$
G/T (dB/K)	10.5	-	7	0.3
Power per Channel	65-70 mW	53 mW (No LNA)	-	208 mW
Power Consumption	142 W (dual-pol.)	27.2 W (dual-pol.)	-	65 W

clear that the G/T reduction is solely due to a reduction in aperture directivity for the different distributions.

Table I summarizes the 1024-element dual-polarized phased-array receiver with embedded transmit filter, and compares it with the other state-of-the-art Ku-band SATCOM receive phased-arrays.

3.4 Conclusion

This chapter presented a low-profile and low-cost 1024-element Ku-band phased array receiver for SATCOM ground terminals and SOTM (Satcom-On-The-Move) applications. Equipped with dual-polarized antennas, the array can synthesize linear, rotated linear and circular polarizations to maintain a link with LEO and GEO satellites by steering the beam to ±70° in all planes with very low cross-polarization at 10.7-12.7 GHz. The array achieves a G/T of 10.5 dB/K

with the use of high-performance LNAs placed at the antenna feeds before the 8-channel silicon beamformer chips. The receive array also employs embedded filters to protect the beamformer chips from being saturated from the transmit array under the same radome. To the authors' knowledge, this is the first time that a phased-array achieved >10 dB/K G/T while being built by using all-silicon commercial chips and a cost-effective, planar, multilayer PCB. Note that if the array is designed to operate up to $\pm 45^{\circ}$ scan angles, as is common in many LEO applications, then the antenna unit cell area would increase by 29%, and the 1024 element array gain will become 35.1 dB at 11.7 GHz (1.1 dB increase). This will increase the G/T to 11.4 dB/K for the same design. The G/T will be further improved by employing the next-generation LNAs and beamformer chips from Renesas (available today) with lower noise figure and much lower DC power consumption, and optimizing the transmit rejection filter.

3.5 Acknowledgment

The authors thank Renesas Electronics for providing the Ku-band SATCOM receive beamformer chips, Kyocera International, San Diego, for the assembly of the phased-array boards in their state-of-the-art assembly line, Keysight for the measurement equipment and ADS software, and ANSYS for the HFSS full-wave EM simulation software. This work was supported by Renesas.

Chapter 3, in part, is a reprint of the material as it appears in: G. Gultepe, S. Zihir, T. Kanar and G. M. Rebeiz, "A Dual-Polarized 1024-Element Ku-band SATCOM Phased-Array with Embedded Transmit Filter and >10 dB/K G/T," presented at 2021 IEEE/MTT-S International Microwave Symposium (IMS), Atlanta, GA, USA, Jun. 10, 2021. The dissertation author was the primary investigator and author of this paper.

Chapter 3, in full, is a reprint of the material as it may appear in: G. Gültepe, T. Kanar, S. Zihir and G. M. Rebeiz, "A 1024-Element Ku-band SATCOM Dual-Polarized Receiver with >10

dB/K G/T and Embedded Transmit Rejection Filter", in *IEEE Transactions on Microwave Theory and Techniques*, accepted. The dissertation author was the primary investigator and author of this paper.

Chapter 4

A 256-Element Dual-Beam Polarization-Agile SATCOM Ku-Band Phased-Array with 5 dB/K G/T

4.1 Introduction

Satellite communications have relied on geosynchronous (GEO) satellites for many years. Covering a large area on the Earth's surface, consumers have accessed them through parabolic dishes and mechanically steered antenna systems [41–49]. Although the demand for the global internet connectivity has been soaring day by day, low-earth-orbit (LEO) and medium-earth-orbit (MEO) satellites could not take the place of the traditional systems due to the high user-terminal cost. Deploying thousands of rapidly moving satellites in the lower orbits requires inexpensive ground terminals which can electronically track the satellites without moving parts. With the deployment of 5G, the cost of phased-array antennas (PAA) has dropped drastically, and low-cost silicon beamformer chips have enabled the commercial use of silicon beamformers in SATCOM and 5G systems [16–18, 20, 21, 24, 36, 51–58, 60–63]. Multi-satellite reception has also become a

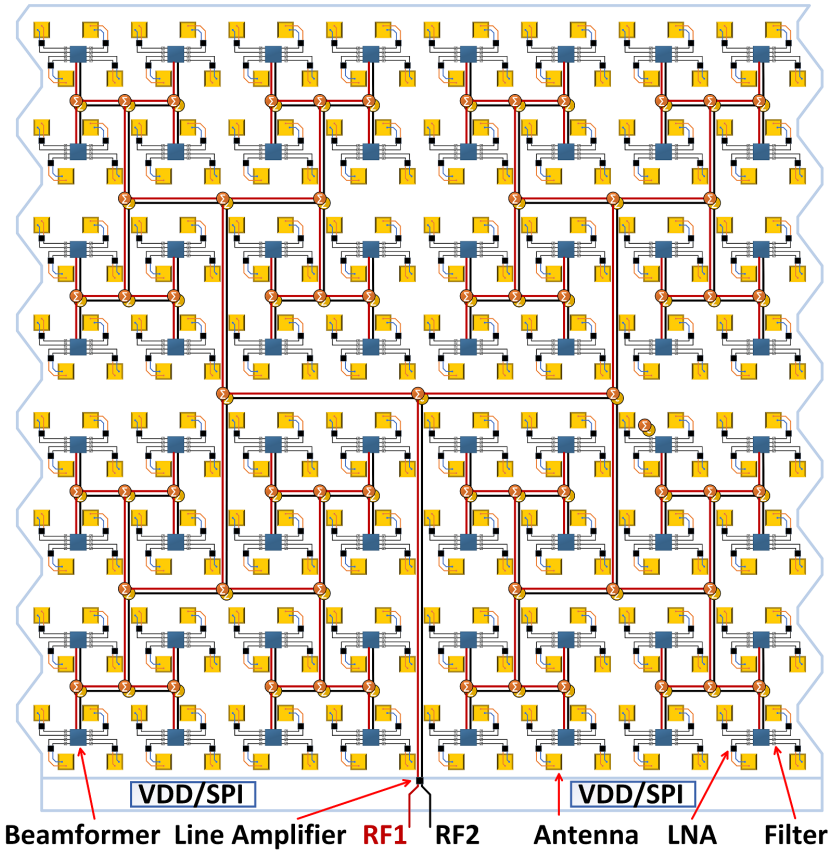

(a)

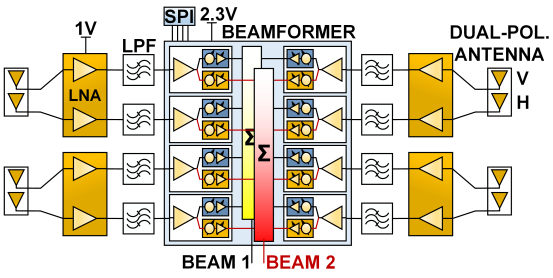

(b)

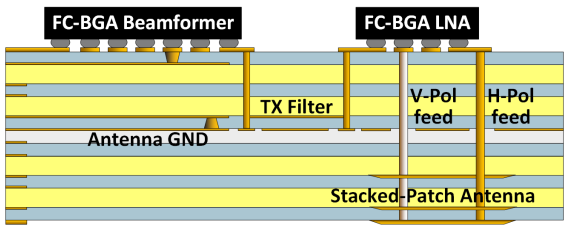

(c)

Figure 4.1: (a) A 256-element dual-beam dual-polarized Ku-band SATCOM phased-array receiver tile. (b) 2x2 antenna quad based on 16-channel RX beamformer chips and dual-channel LNAs. (c) 12-layer, cost-efficient PCB stackup.

requirement for some LEO constellations for make-before-break systems.

This paper is an expanded version of [56] and presents an cost-efficient Ku-band SATCOM phased array receiver with dual-beam reception capability (Fig. 4.1). The paper is also an extended

version of [62] showing a dual-beam capability in a 256-element array. Details related to the dual-beam design, and measurements of both beams and their G/T performance, are presented.

4.2 16x16 Phased-Array Receiver Design

The physical structure of the 16x16 phased array receiver tile is shown in Fig. 4.1. The planar printed circuit board (PCB) is designed as $2\times$N scalable since all the connectors (SPI, power and RF) are placed on one side of the PCB, and the tile boundaries follow the triangular antenna grid. It can be used as a standalone receiver by downconverting and processing the signals at the two RF outputs, or the array size can be grown using an external Wilkinson combiner.

The PCB is built on a low-cost 12-layer stack-up with Panasonic Megtron-6 substrate (ε_r=3.63 and tanδ=0.004 at 12 GHz) (Fig. 4.1c). RF routing, power (DC) and SPI routing are between M1-M6 layers whereas M6-M12 layers are allocated for the antenna.

In this design, LNAs are placed at the antenna ports to reduce the transmission line loss between the antenna and the chip. (Fig. 4.1b). For every 0.1 dB decrease in the line loss, the G/T improves by $\sim$0.2 dB. The LNA placed at the antenna feeds results in a 0.5-0.6 dB improvement in G/T without increasing the array size.

A transmission line filter is also placed after the LNA to suppress the transmit band signals at 14-14.5 GHz which may saturate the beamformer chip. This is important especially when the transmit and receive array pairs are on the same platform. Details of this filter and its system effects have been covered in [62] and are not repeated here for brevity.

4.2.1 Antenna Design

A stacked-patch antenna is designed considering its affordable implementation while maintaining a relatively wide bandwidth (Fig. 4.1c). A driven patch is etched on M9 with M6 as the antenna ground, which couples to the two parasitic patches on M11 and M12 to

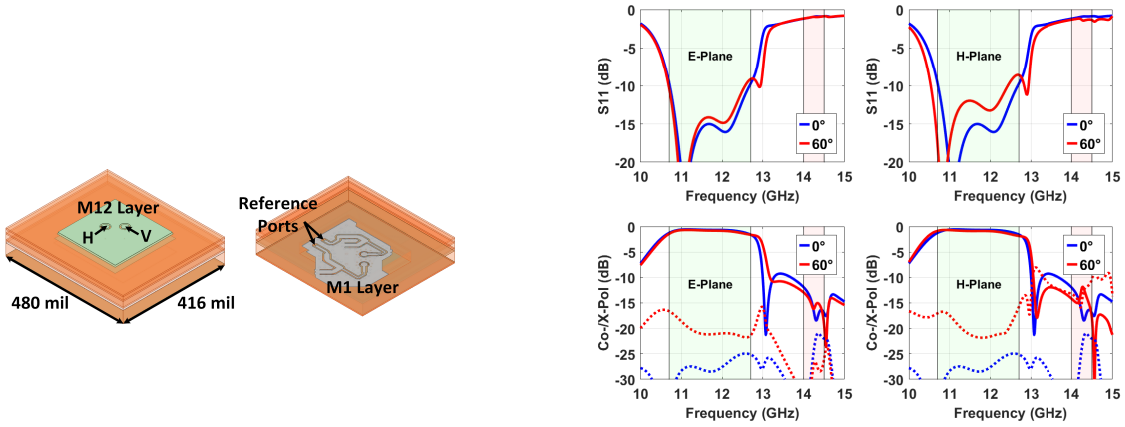

(a) (b)

Figure 4.2: (a) 2x2 cell on PCB (M1 and M12 only) [62]. (b) Simulated S_{11}, co-pol and cross-pol vs. scan angle (0°, 60°) referenced to the LNA input [62].

enhance impedance bandwidth. The patches are square and fed by two orthogonal probes for dual-polarization. A short transmission line matching circuit connects the antenna to the LNA. This ensures that the antenna is well-matched in the receive band though it introduces 0.1-0.2 dB loss before the LNA. Still, the ohmic loss is lower than the matching loss and the matching circuit is required for best performance.

The antenna spacing is $\lambda/2$ at 12.2 GHz in an equilateral triangular grid (Fig. 4.2a). This allows a grating lobe free scan range of $\pm 70°$ up to 12.7 GHz. The antenna element directivity is 3.9 dB at 11.7 GHz, which translates in to an antenna directivity of 28 dB for the 256-element array.

$$D_{array} = \frac{4\pi 256 A_{element}}{\lambda^2_{@11.7\,GHz}} = 28\,\text{dB} \tag{4.1}$$

The antenna is simulated in Ansys HFSS, including the coaxial transition between M1-M6 and the short matching network before the signal is fed to the LNA. The lattice pairs are adjusted to impose the desired triangular grid with a Floquet port excitation under an infinite-array assumption.

Fig. 4.2b shows that the antenna has a reflection coefficient below -9 dB in both E- and H-planes even for $\pm 60^\circ$ scan angle at 10.7-12.7,GHz, and further simulations can be found in [62]. The cross-polarization level is below -17 dB when the antenna is scanned to $\pm 60^\circ$ off broadside. To further decrease the cross-polarization level, a feed-rotation technique is employed in a 2x2 cell. This method helps cancel the magnetic currents on the non-radiating edges of the patches in the principal planes and results in $<$-30 dB cross-polarization levels [24].

The antenna loss before the LNA is 0.6-0.7 dB at 11.7 GHz and rises to 0.8 and 1.1 dB at 10.7 GHz and 12.7 GHz, respectively. This increase is caused by the relatively high reflection coefficient at the receive band edges. The antenna also suppresses the undesired transmit signals (14-14.5 GHz) by -12 to -15 dB and protects the LNA from being saturated by the transmit leakage.

4.2.2 LNA and Dual-Beam RX Beamformer

In order to lower to system noise figure, a commercial dual-channel LNA (Renesas F6921v2) is placed just after the dual-polarized antenna with a gain and a noise figure (NF) of 19 dB and 1.4-1.5 dB at 11 GHz. The input 1-dB compression point (IP1dB) of the LNA is -23 and -19 dBm at 11.7 and 14 GHz, respectively, and it consumes 15 mW per channel at 1 V.

The 4 LNAs in a 2x2 antenna cell feed a SiGe beamformer chip (Renesas F6121) with 8 RF input ports and 16 channels. Each 8 channels are combined into one RF output, enabling a dual-beam reception (Fig. 4.1b). The beamformer has an electronic gain of 12 dB at 11.7 GHz, which is S_{21}+9 dB, where S_{21} is the gain obtained by energizing only one channel and terminating all the others. The 9 dB compensates the excess Wilkinson loss due to the other channels turned off. Each channel has a 6-bit variable gain amplifier (VGA) with 30 dB linear attenuation range and a 6-bit phase shifter with a phase-step of 5.625° steps. The beamformer chip has a NF of 5.6-6 dB in the receive band with an IP1dB of -33 dBm and -27 dBm at 11.7 and 14 GHz, respectively. This chip consumes 30-34 mW per channel at 2.3 V.

Table 4.1: RX SiGe Beamformer and LNA Summary

Parameter	Unit	F6121 BF	F6921v2 LNA
Frequency	GHz	10.7-12.75	10.7-12.75
No. of Channels	-	8x2	2
Package	-	FC-BGA	FC-BGA
Typical Gain	dB	12	19
Noise Figure	dB	5.6	1.4-1.5
IP_{1dB}	dBm	-33	-23
Phase Shifter	bit	6	-
Phase Step	degree	5.625	-
Phase Error	degree rms	3	-
VGA	bit	6	-
VGA Step	dB	0.4-0.45	-
Gain Control	dB	30	-
Gain Error	dB rms	0.2-0.3	-
Power/channel	mW	30-34	15
Supply Voltage	V	2.3	0.9-1.1

The combined gain and NF of the LNA and the 16-channel beamformer are 31 dB and 1.6 dB at 11.7 GHz. The IP1dB is -52 dBm at 11.7 GHz, and rises to -42 dBm at 14 GHz due to the lower LNA gain and higher IP1dB of the beamformer chip at 14 GHz.

4.2.3 Filtering Out the Transmit-Leakage

An important point to consider in a simultaneous transmit and receive system is the unwanted near-field coupling of the transmit signal to the receiver. This may lead to the saturation of the receiver unless necessary precautions are taken (Fig. 4.3a and 4.3b). Assuming an average coupling of -60 dB from a TX antenna with 10 dBm radiated power, the power incident to the LNA input will be -30 dBm considering a combination of 100 TX antennas (20 dB) in the vicinity of the receive antenna. The LNA will safely operate as its IP1dB is -19 dBm at 14 GHz.

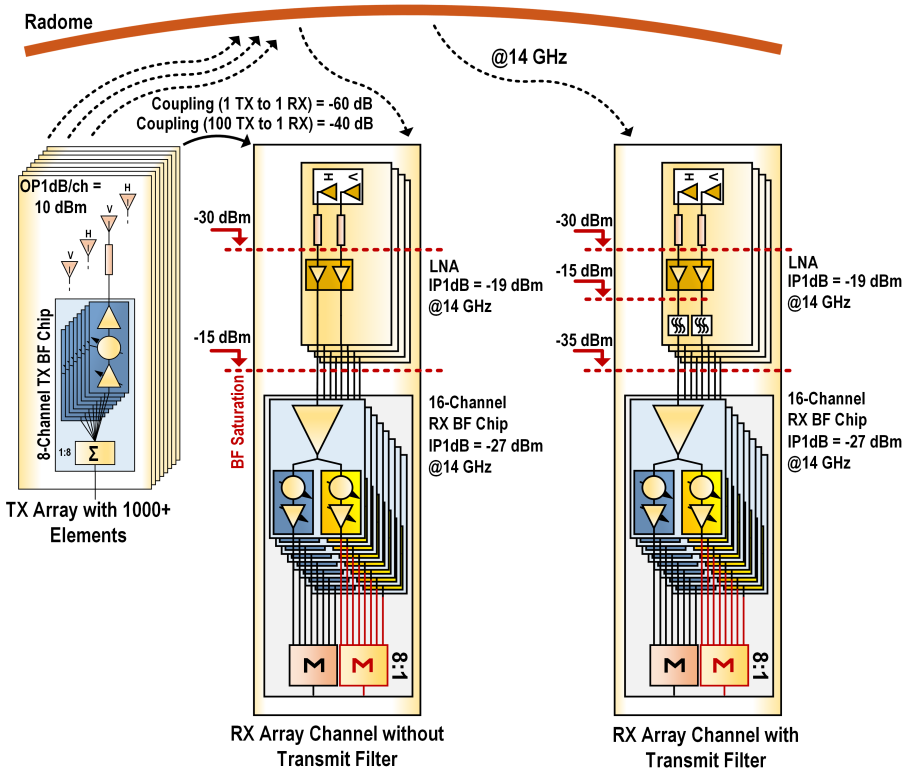

(a)

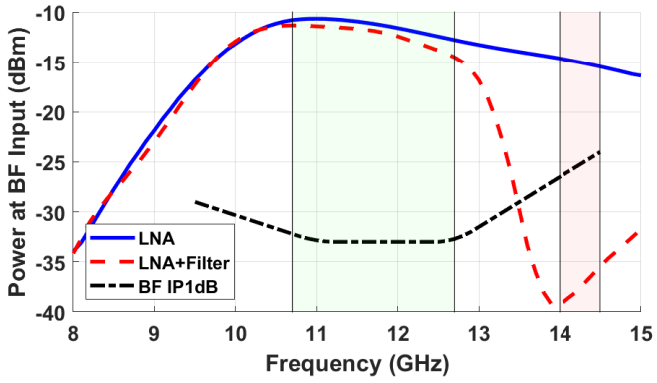

(b)

Figure 4.3: (a) Transmit leakage analysis when TX and RX arrays are placed side by side and shared a radome. (b) Power level at the beamformer input for a signal of -30 dBm impinging on the LNA.

To protect the beamformer from saturation due to the amplified TX leakage signal (from the LNA), a filter with a suppression of 20-25 dB is embedded in the PCB stack-up. Note that the in-band filter loss will not worsen the system NF as it is placed after the LNA with 19 dB gain. More details can be found in [62].

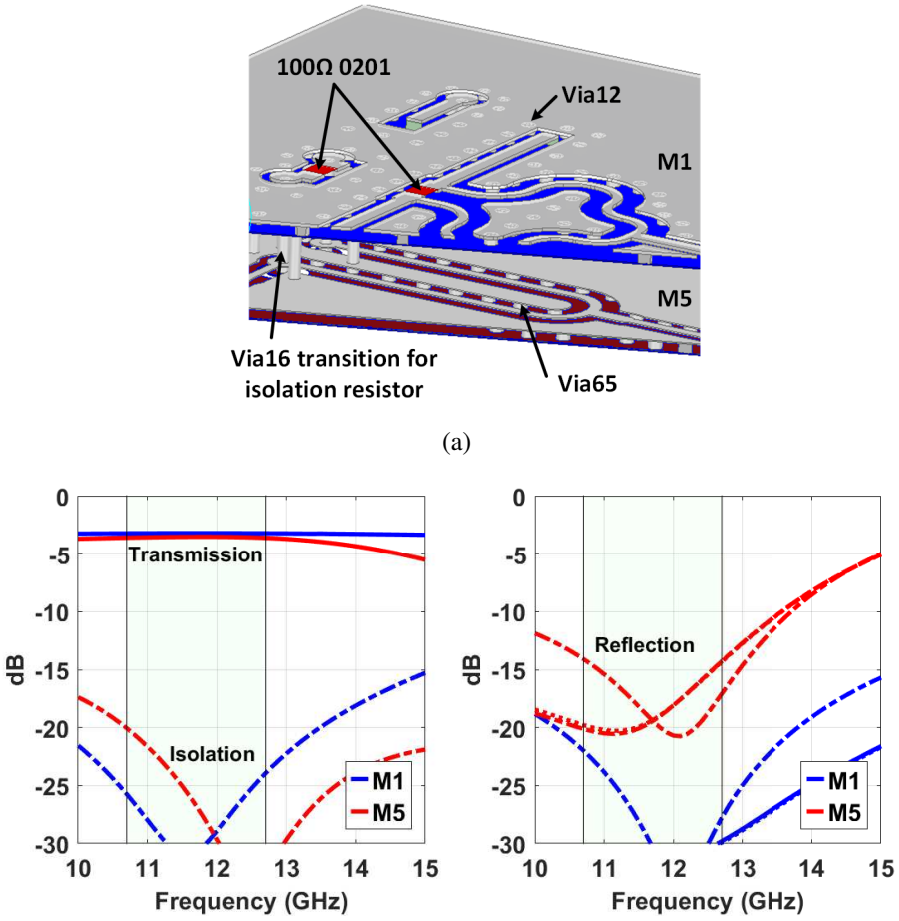

Figure 4.4: (a) Wilkinson models with 0201 resistors on M1 layer. (b) Simulated reflection, isolation and transmission of the Wilkinson combiners.

4.2.4 Wilkinson Combiner Network

The output ports of 64 the beamformer chips are combined using two separate 6-stage Wilkinson networks. One of the networks is implemented on M1 layer with M2 as ground, and the other Wilkinson network is routed on M5 layer (Fig. 4.4a). The latter is a quasi stripline with the ground planes on M5 and M6 connected with via65. Both Wilkinson combiners are designed with a characteristic impedance of 50 Ω and use 0201 packaged 100 Ω isolation resistors on M1. The simulated insertion loss of the Wilkinson combiners on M1 and M5 are 0.25 and 0.5 dB, respectively, at 10.7-12.7 GHz. Both of them show an isolation of >20 dB (Fig. 4.4b).

A dual-channel LNA is placed before the RF connectors to increase RX electronic gain of the array. This LNA acts as a line amplifier and amplifies the signal by 19 dB and compensates for the PCB line and Wilkinson network losses.

4.2.5 Connectorized Channel Test Board

A connectorized RF board with a 16-channel RX beamformer and two dual-channel LNAs is first used to test the RF performance and extract the channel gain and NF (Fig. 4.5). An embedded transmit fiter is also placed between the LNA on the left side and the beamformer RF input ports 2 and 3. On the right side, the LNA output ports are directly connected to the 5th and 6th RF input ports of the beamformer. This measures the filter response and its effect on the RF performance on the channel. The channel electronic gain (G_{ch}) is measured as 32 dB:

$$\begin{aligned} G_{ch} &= G_{LNA} - L_{LPF} + G_{BF} \\ &= 21 - 0.7 + 12 \\ &= 32.3\,\text{dB} \end{aligned} \tag{4.2}$$

With a higher reference current, the LNA provides a gain of 21 dB at 11 GHz. The measurements with and without the filter show that the filter has an in-band loss of 0.7 dB at 11.7 GHz and $\sim$1.5 dB at 12.7 GHz, and that it suppresses the signal by 25 dB at 14 GHz.

The measured channel NF is 1.57 dB at 11.7 GHz (Fig. 4.5d). The $\pm$0.1 dB difference between the NF measurements for beam-1 and beam-2 is due to the measurement error since measuring such a low NF with a PNA-X needs a pretty accurate calibration. The simulated NF is 1.51 dB, for an LNA NF of 1.4 dB:

$$\begin{aligned} F_{ch} &= F_{LNA} + \frac{L_{LPF} - 1}{G_{LNA}} + \frac{F_{BF} - 1}{G_{LNA}/L_{LPF}} \\ &= 1.42\,(NF_{ch} = 1.51\,\text{dB}) \end{aligned} \tag{4.3}$$

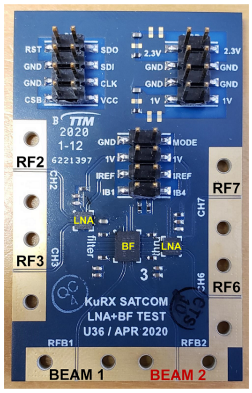

(a)

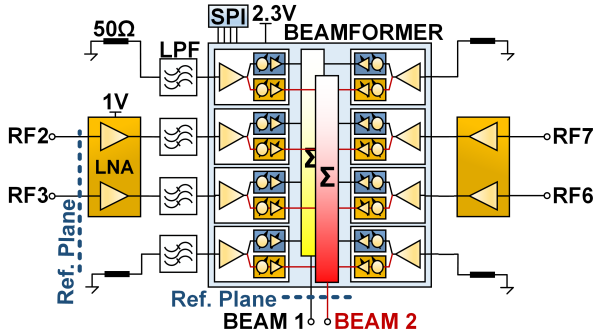

(b)

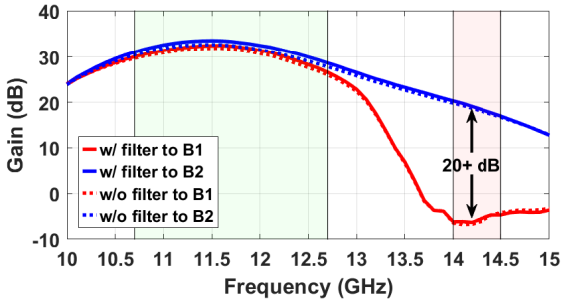

(c)

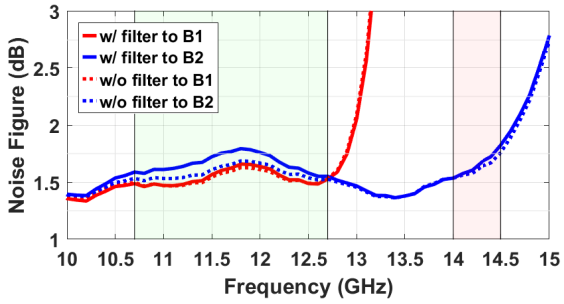

(d)

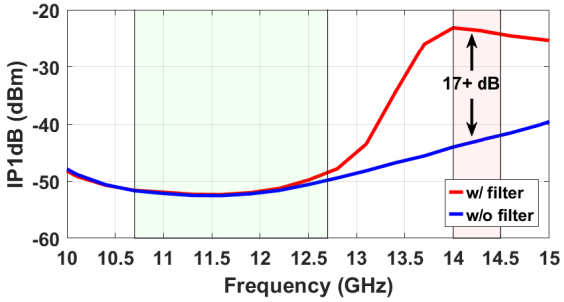

(e)

Figure 4.5: (a) PCB and (b) Schematic of the connectorized channel test board. (c) Gain, (d) NF and (e) IP1dB of an RF channel with and without the transmit filter between the LNA and a beamformer channel.

which is within 0.1 dB compared to measurements performed using a Keysight PNA-X. As expected the filter has a negligible impact on the channel NF.

Fig. 4.5e shows that the filter improves the channel IP1dB at 14 GHz to -27 dBm. Without this filter, the channel has an IP1dB of -44 dBm and can be saturated by the TX coupling.

4.2.6 Receiver Noise Figure and G/T

Fig. 4.6 presents the equivalent RF chain of the 256-element array. As the array has 2 different Wilkinson networks, the second of which has a bit more loss, the NF of each beam is also slightly different:

$$\begin{aligned} F_{rec} &= F_{ch} + \frac{L_W - 1}{G_{ch}} + \frac{F_{LA} - 1}{G_{ch}/L_W} + \frac{L_{conn} - 1}{G_{ch}G_{LA}/L_W} \\ NF_{recB1} &= 1.55\,\text{dB} \\ NF_{recB2} &= 1.57\,\text{dB} \end{aligned} \tag{4.4}$$

Since D_{array} is 28 dB at 11.7 GHz from (1), the array gain can be calculated for 0.6 dB antenna ohmic and transmission-line loss and 0.1 dB matching loss:

$$\begin{aligned} G_{array} &= D_{array} - L_{TL} - ML \\ &= 28\,\text{dB} - 0.6\,\text{dB} - 0.1\,\text{dB} \\ &= 27.3\,\text{dB} \end{aligned} \tag{4.5}$$

The array G/T can be calculated as:

$$G/T = G_{array} - 10\log_{10}(T_S) \tag{4.6}$$

where T_S is the receiving system noise temperature. Its contributors are the effective antenna

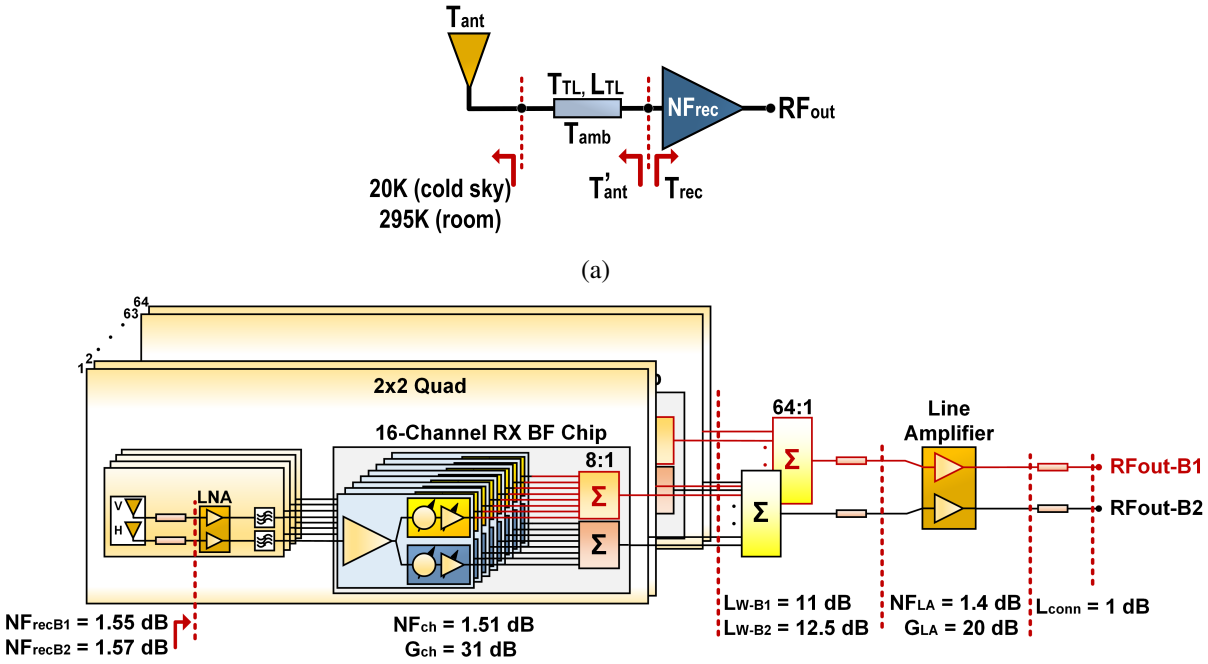

Figure 4.6: (a) RF chain for G/T calculation. (b) RF chain of the 256-element dual-beam receive phased array.

noise temperature (T'_{ant}) and the effective input noise temperature of the receiver (T_{rec}).

$$T_S = T'_{ant} + T_{rec} \tag{4.7}$$

where T'_{ant} includes the temperature of the antenna and the transmisiion line with a loss of L_{TL}, connecting it to the receiver input (LNA).

$$T'_{ant} = T_{ant}/L_{TL} + T_{TL} \tag{4.8}$$

$$T_{TL} = T_{amb}\,(1 - 1/L_{TL}) \tag{4.9}$$

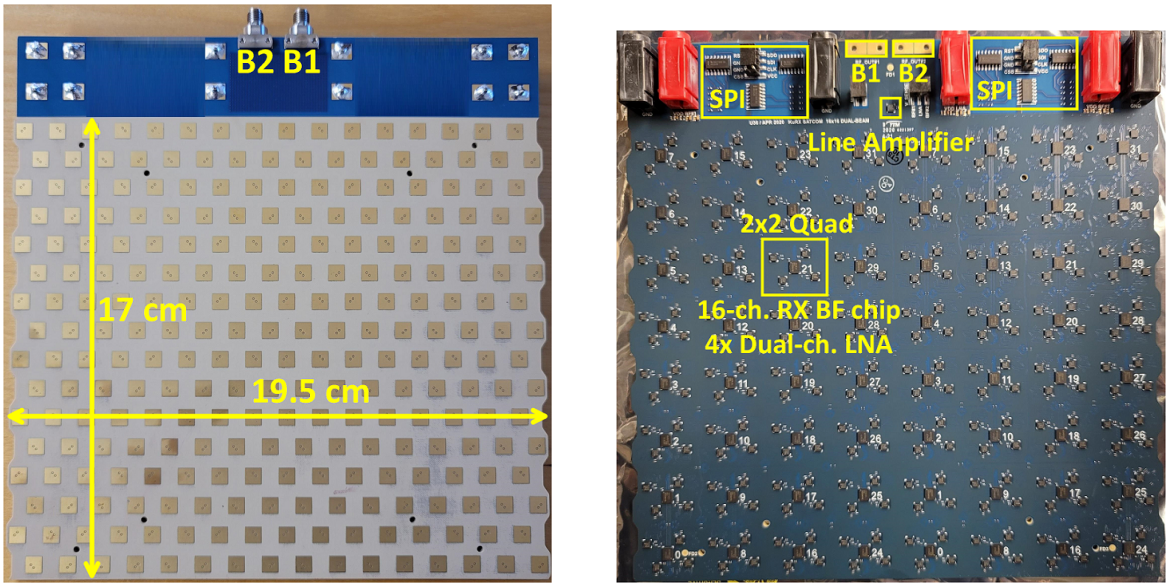

(a) (b)

Figure 4.7: (a) Antenna side of 256-element dual-beam Ku-band SATCOM RX array. (b) Component side of 256-element array.

When the antenna faces the sky (T_{ant}=20 K) and L_{TL}=0.6 dB, T_S is 180 K and 182 K for beam-1 and beam-2, respectively, and the G/T at 11.7 GHz is:

$$\begin{aligned} G/T &= 27.3\,dB - 10\log_{10}(T_S) \\ &= 4.75\,\text{dB/K}\ beam-1 \\ &= 4.7\,\text{dB/K}\ beam-2 \end{aligned} \tag{4.10}$$

4.3 Measurements

The 256-element array is tested in an anechoic chamber with a 4-port Keysight PNA-X Microwave Network Analyzer (Fig. 4.7 and 4.8a). The array patterns are measured at 2.5 m, which is nearly the far-field distance (2.96 m).

The power consumption is 75 mW/antenna/polarization for dual-beam operation (LNA: 15 mW, 2 RX beamformer channels: 30 mW/channel) The 256-element array consumes 38.4 W

for dual-beam operation. Fans are used at the back of the array to keep it at <45°C.

4.3.1 Calibration and Frequency Response

The calibration is done at 11.7 GHz, the mid-band frequency. Energizing one channel at a time, the phase and gain of each channel are adjusted at broadside after comparing their S21 responses between the RF connector of the array and the horn antenna at the far-field. This procedure is performed iteratively for the beam-1 channels. As the beam-1 and beam-2 channels share the same RF chain except for the Wilkinson network, the coefficients found for beam-1 are applied to the phase shifter and variable gain amplifier for each channel in beam-2 to reduce the calibration time by a half. This method results from the fact that the F6121 beamformer channels are nearly identical and have very low rms amplitude and phase errors. The array achieves a 0.2 dB and 1.2° rms amplitude and phase errors after calibration state for each beam.

Fig. 4.8b presents the frequency response for beam-1 and beam-2. The array gain drops by 10 dB at 12.7 GHz since the channel gain (LNA, filter, beamformer) dops by 5-6 dB at 12.7 GHz (Fig. 4.5c), and the line amplifier (LNA) gain decreases by 2 dB. Adding the ∼1 dB additional loss for the Wilkinson network, this 10 dB drop is reasonable if a small shift in the antenna and filter responses is also taken into account. This might be caused by the ε_r and thickness changes across the PCB. Note that the frequency response drop at 12.7 GHz has a minor effect on the array G/T since it occurs mostly after the LNA gain.

There are some ripples in beam-2. Those are mostly due to the coupling between the transmit filters and the second Wilkinson network. Because of the space limitations in the PCB layout, the RF lines on M5 could not be isolated from the filters using dense shielding vias. This results in an increased coupling between the filters and the main RF network line due to the evanescent parallel plate modes. A new design with more PCB layer would solve this problem.

The array response results in an excellent rejection in the transmit band (14-14.5 GHz). The 55 dB rejection is due to ∼15 dB suppression by the antenna, ∼35 dB drop in the channel

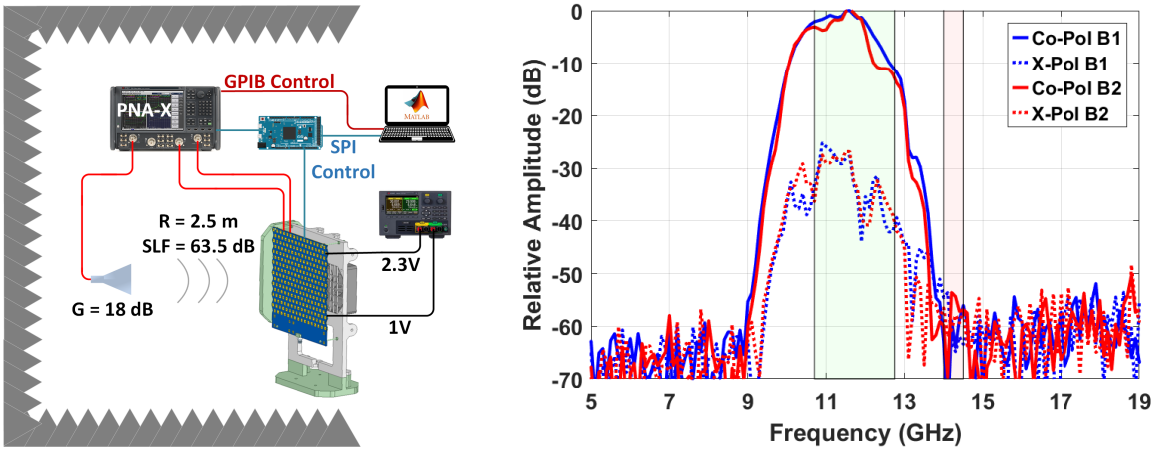

(a) (b)

Figure 4.8: (a) Calibration and measurement setup in an anechoic chamber. (b) Frequency response of the 256-element dual-beam RX array. Ku-band SATCOM RX (10.7-12.7 GHz) and TX (14-14.5 GHz) bandwidths are shaded in green and red, respectively.

gain (Fig. 4.5c) with respect to the receive band, 4 dB decline in the line amplifier (LNA) gain and 2 dB additional loss of the Wilkinson network at 14-14.5 GHz.

4.3.2 Pattern and G/T Measurements

To test the validity of the calibration method that the same calibration coefficients are loaded to both beams under uniform illumination. Fig. 4.9a shows that both beams have almost identical broadside patterns with -30 dB cross-polarization level.

Then, a 180° phase shift is applied to a half of the beam-2 channels to synthesize a difference pattern and a null at broadside. A monopulse pattern is obtained for direction of arrival (DOA) estimation by comparing the phases of beam-1 and beam-2. This is also a rigorous test to determine beam-1 to beam-2 coupling, including coupling effects due to on-chip channels and the two Wilkinson networks. This is because beam-1 has a maximum signal, whereas beam-2 has almost zero signal at the same frequency. Fig. 4.9a shows a -30 dB null, which indicates a superb isolation.

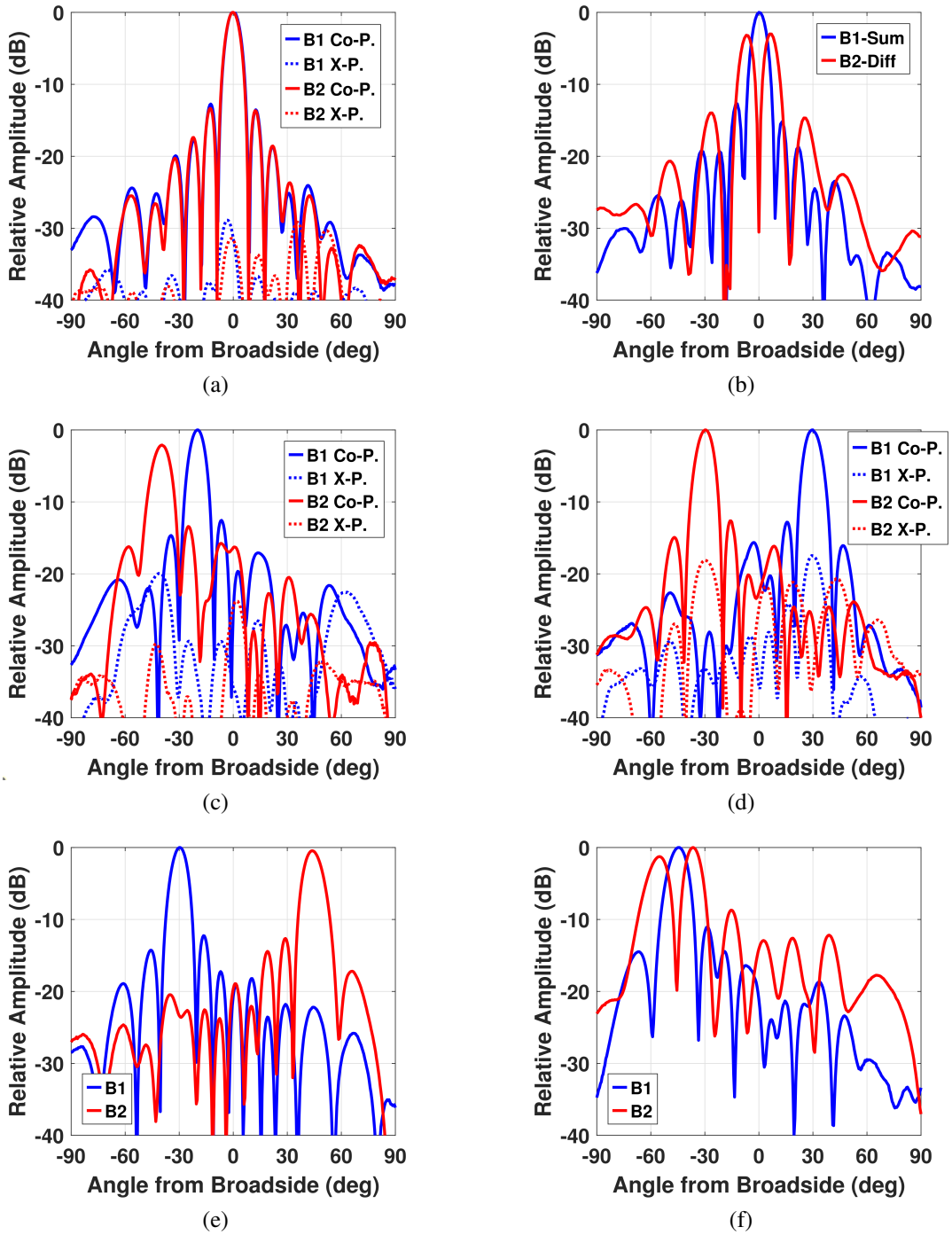

Figure 4.9: Uniform illumination at 11.7 GHz: (a) Beam-1: V-pol. sum at broadside, Beam-2: V-pol. sum at broadside, (b) Beam-1: V-pol. sum at broadside, Beam-2: V-pol. difference at broadside, (c) Beam-1: V-pol. sum at -20° scan, Beam-2: H-pol. sum at -40° scan, (d) Beam-1: V-pol. sum at +30° scan, Beam-2: H-pol. sum at -30° scan, (e) Beam-1: H-pol. sum at -30° scan, Beam-2: H-pol. sum at +45° scan, (f) Beam-1: V-pol. sum at -45° scan, Beam-2: V-pol. difference at -45° scan.

Beam-1 and beam-2 are then steered to different angles, while having the same or different polarizations, to receive data streams from different transmitters. This is a significant feature for make-for-break systems. All measurements are done without any further calibration (done for broadside only) (Fig. 4.9c, 4.9d and 4.9e). Also, a difference is applied at -45° scan angle, and a 20 dB null is achieved for location finding (Fig. 4.9f).

An amplitude taper with -7 dB raised cosine is also applied to both beams. The sidelobes are lowered to >-18 dB while maintaining different DoA for the two beams (Fig. 4.10). The scan loss follows a $(cos\theta)^{1.2}$ with a 3.6 dB at ±60° scan angles, and the scan patterns are not plotted due to brevity. The reader can refer to [62] for representative patterns from a single beam design.

The G/T is measured for the 2 individual beams in the 256-element array. The measurement is done in an anechoic chamber where T_{ant} is 295 K. Then the G/T is calculated when the antenna faces towards the sky. The G/T increase for T_{ant}=20 K is given by:

$$G/T_{@20K} = G/T_{@295K} + 10log_{10}(\frac{T_S}{T_S - 275/L_{TL}}) \tag{4.11}$$

where T_S is the receiving system noise temperature (T_{ant}=295 K). The max G/T is 5 dB/K at 11.7 GHz when it points towards the cold sky. Beam-2 has a 0.3 dB lower G/T due the lossier embedded Wilkinson network. Around 12.7 GHz, the decrease in G/T is due to the sharp transmit-filter filter response and the LNA gain drop. The G/T at the lower band edge suffers from the additional matching and cross-polarization losses of the antenna. Also, the calibration is done at 11.7 GHz, and there is an additional drop in the antenna gain due to the fact that the 2x2 cells are not completely symmetrical. A higher G/T at 10.7 GHz and 11.7 GHz would have been achieved if the array was calibrated in 300 MHz steps over the entire 10.7-12.7 GHz range.

The G/T versus scan angle was measured in the anechoic chamber and follows a $cos(\theta)^{1.2}$ curve, which is the expected scan loss (Fig. 4.11b). The G/T for a 7 dB cosine taper for lower

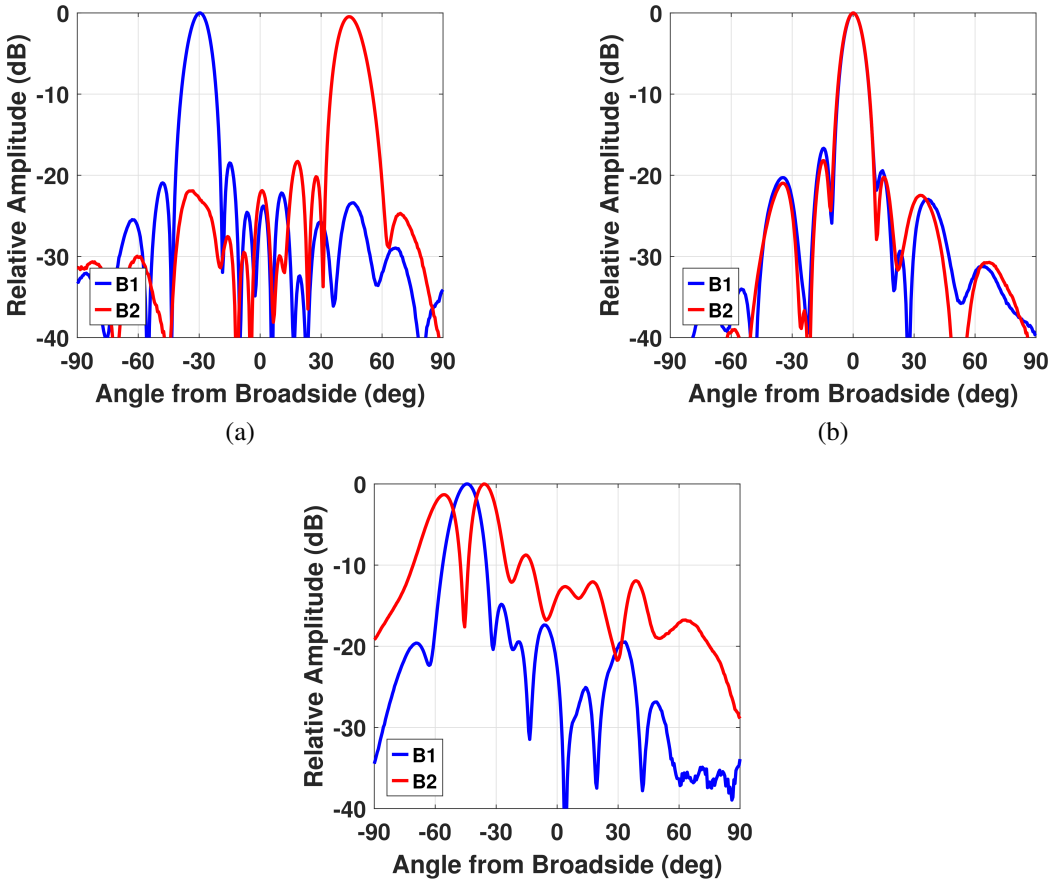

Figure 4.10: 7 dB cosine taper at 11.7 GHz, (a) Beam-1: V-pol. sum at -30° scan, Beam-2: V-pol. sum at +45° scan, (b) Beam-1: V-pol. sum at broadside, Beam-2: V-pol. sum at broadside, (c) Beam-1: V-pol. sum at -45° scan, Beam-2: V-pol. difference at -45° scan.

side lobes drops by 0.3 dB (Fig. 4.11c). This is very close to the theoretical aperture efficiency of 90% (0.46 dB). The LNAs with fixed gain at the front preserves the low noise operation even after a 7 dB amplitude taper is applied in the beamformer chips.

Table I provides a summary of the 256-element dual-polarized dual-beam phased-array receiver with embedded transmit filter, and a comparison with the state-of-the-art Ku-band SATCOM phased-arrays receivers.

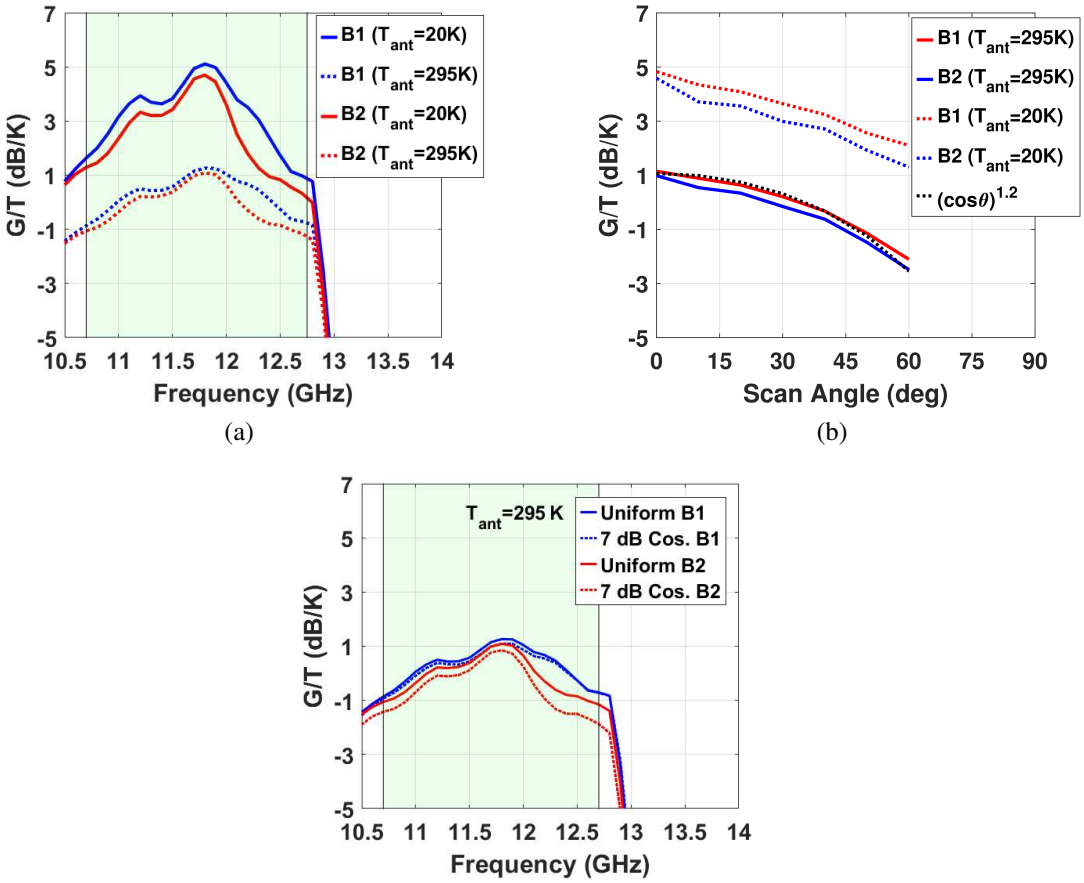

Figure 4.11: (a) Measured G/T at broadside when T_{ant}=295 K and its correspondence when the array looks at the cold sky (T_{ant}=20 K). (b) Measured G/T vs. scan angle (T_{ant}=295 K) at 11.7 GHz. (c) Measured G/T under uniform illumination and 7 dB cosine at broadside when T_{ant}=295 K.

4.4 Conclusion

This chapter presented a low-profile, planar, scalable, 256-element Ku-band phased array receiver with dual-beam reception. It proves that a multi-beam receiver can be built on the same low-cost PCB with high isolation. Beamformers with 16 channels and silicon LNAs with very low NF result in an affordable, high performance and lower power multi-satellite arrays. To the author's knowledge, this is the first time such work with all silicon chips, dual-beam and high G/T is demonstrated.

Table 4.2: Comparison with State-of-the-Art Ku-band SATCOM Phased-Array Receivers

Parameter	This Work	[18] UCSD'18	[60] 2017	[55] 2013
Frequency (GHz)	10.7-12.7	10.6-12.5	10.7-12.7	10.7-12.75
No. of Elements	256 (16x16)	256 (16x16)	256 (16x16)	156
# of Beams	Dual-Beam	Single	Single	Single
Antenna Type	Patch (PCB)	Patch (PCB)	Patch (PCB)	Patch (PCB)
Array Grid	Triangular	Rectangular	Rectangular	Triangular
Polarization	Dual-Linear	Dual-Linear	Linear	Dual-Linear
HPBW @11.7 GHz	7.6°	6.7°	-	-
Elevation Scan	140°(±70°)	140°(±70°)	Fixed at 23°	140°(±70°)
Azimuth Scan	140°(±70°)	140°(±70°)	40°(±20°)	140°(±70°)
X-Pol. Reject. (dB)	>19	>23	>20	>17
Size (cm^2)	19.5x17	22.2x19.7	25x37	$\pi\times11^2$
G/T (dB/K)	5	-	7	0.3
Power Consumption	25 W (single beam)	27.2 W	-	65 W

4.5 Acknowledgment

The authors thank Renesas Electronics for providing the Ku-band SATCOM dual-beam receive beamformer chips, Kyocera International, San Diego, for the assembly of the phased-array boards in their state-of-the-art assembly line, Keysight for the measurement equipment and ADS software, and ANSYS for the HFSS full-wave EM simulation software.

Chapter 4, in part, is a reprint of the material as it appears in: G. Gultepe and G. M. Rebeiz, "A 256-Element Dual-Beam Dual-Polarization Ku-Band Phased-Array with 5 dB/K G/T for Simultaneous Multi-Satellite Reception," presented at 2021 IEEE/MTT-S International Microwave Symposium (IMS), Atlanta, GA, USA, Jun. 10, 2021. The dissertation author was the primary investigator and author of this paper.

Chapter 4, in full, is a reprint of the material as it may appear in: G. Gültepe and G. M. Rebeiz, "A 256-Element Dual-Beam Polarization-Agile SATCOM Ku-Band Phased-Array

with 5 dB/K G/T", in *IEEE Transactions on Microwave Theory and Techniques*, submitted. The dissertation author was the primary investigator and author of this paper.

Chapter 5

Conclusion and Future Work

5.1 Conclusion

This dissertation presented transmit and receive planar phased-array systems for Ku-band SATCOM ground and SOTM terminals. All the arrays are based on 2x2 antenna cells with all-silicon 8- or 16- channel transmit or receive beamformer chips, and operate with high performance (EIRP or G/T). There are also other AESAs from Cobham, Starlink, Phasor, Rockwell Collins and Facebook, and they use the same approach with beamformer chips assembled onto a flat-panel PCB with microstrip antennas. By this way, each antenna element has an individual control of radiation phase and amplitude.

In chapter 2, a 14-14.5 GHz Ku-band 1024-element phased-array transmitter with an EIRP of 44-45 dBW was presented for mobile SATCOM ground terminals. The array can steer the beam in $\pm 75°$cone with a cross-polarization rejection $>$33 dB at broadside and $>$30 dB at 60°scan angle due to the feed rotation in the 2x2 antenna cells. The array consumes 164 W per polarization, the power drops to 100 W with the use of the Renesas second generation 8-channel SiGe beamformer chips. The measured EVM is $<2\%$ for QPSK and 8PSK waveforms, and an ACPR of $<$-29 to -30 dB even at P1dB and Psat EIRP values, and the EVM remains below 2%

(a)

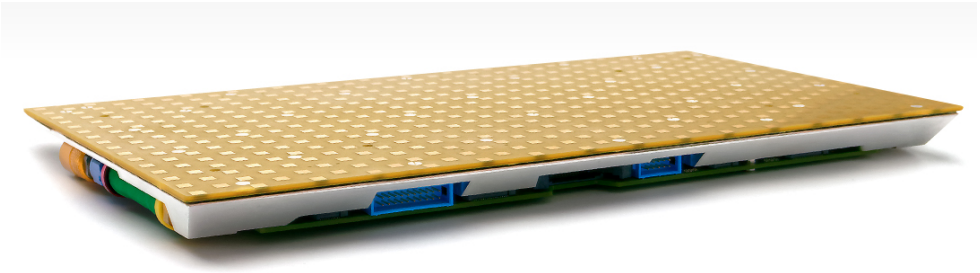

(b)

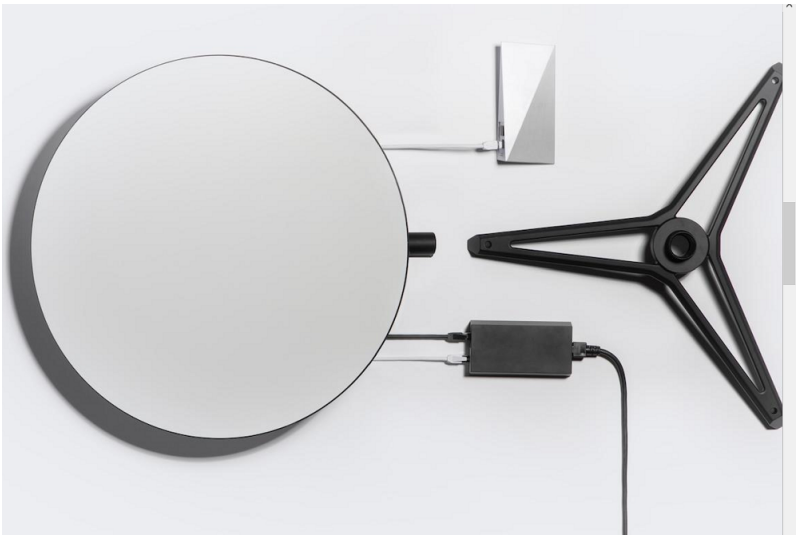

(c)

Figure 5.1: Low-profile, flat-panel AESA examples: (a) Cobham's HGA-7001 High Gain SATCOM Antenna [64]. (b) Hanwha-Phasor's phased array antenna [65]. (c) Starlink commercial consumer AESA terminal for high-speed internet over its LEO satellite network based on beamformer chips and LNAs [66].

up to 60°scan angles. This increases the array efficiency since a 2-3 dB backoff is not needed, and a phased-array can operate at P1dB or even Psat while still meeting SATCOM out-of-band requirements. The array design with chips on a single PCB results in an affordable solution for Ku-band SATCOM and in excellent performance at P1dB and Psat EIRP values.

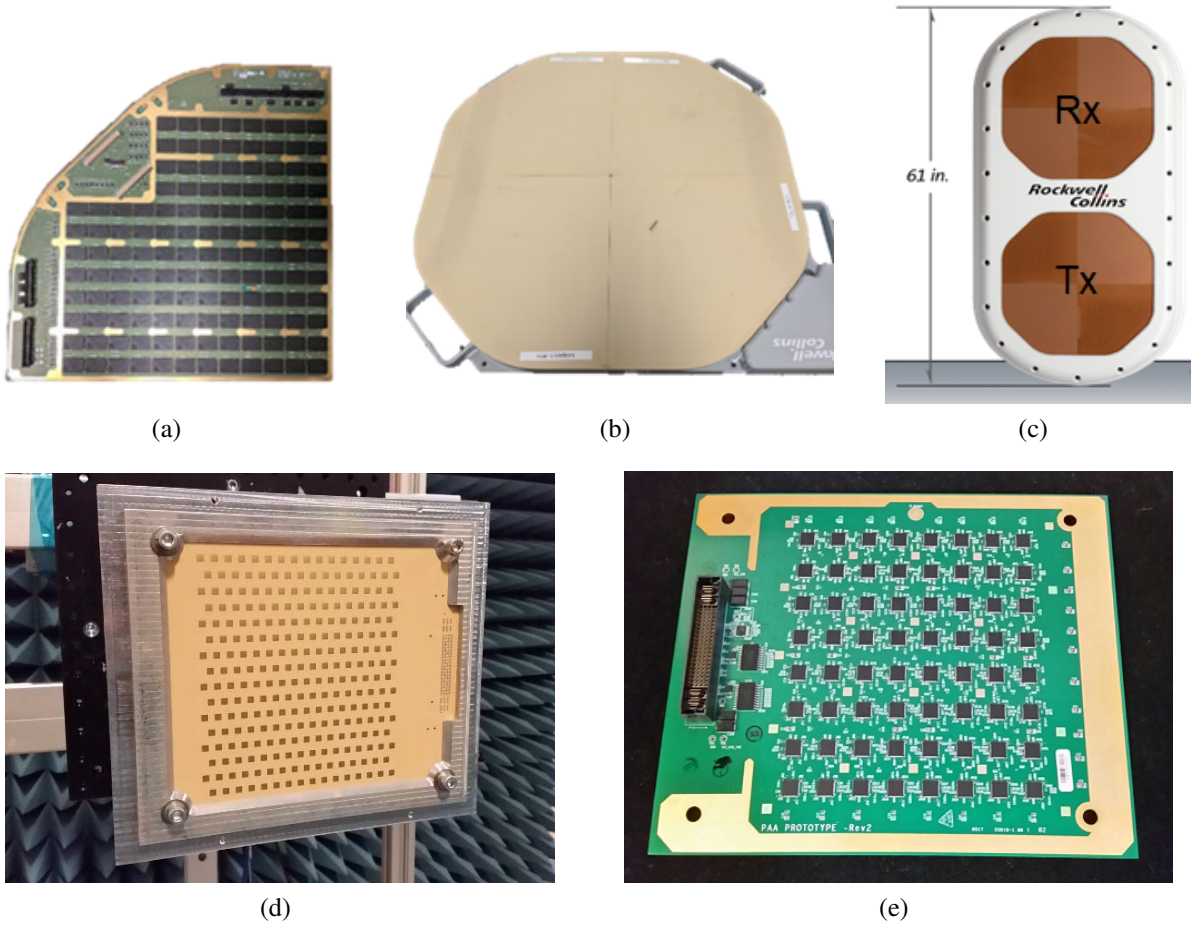

(a) (b) (c)

(d) (e)

Figure 5.2: Rockwell Collins' 2000+ element AESA [67]: (a) A quadrant, (b) Full array prototype, (c) TX and RX array aray pairs. Facebook's 256-element K-band RX array [68]: (d) Front view, (e) Backside view.

In chapter 3, a low-profile and low-cost 1024-element Ku-band phased array receiver is presented for SATCOM ground terminals and SOTM (Satcom-On-The-Move) applications. Equipped with dual-polarized antennas, the array can synthesize linear, rotated linear and circular polarizations to maintain a link with LEO and GEO satellites by steering the beam to $\pm 70°$ in all planes with very low cross-polarization at 10.7-12.7 GHz. The array achieves a G/T of 10.5 dB/K with the use of high-performance LNAs placed at the antenna feeds before the 8-channel silicon beamformer chips. The receive array also employs embedded filters to protect the beamformer

chips from being saturated from the transmit array under the same radome. To the authors' knowledge, this is the first time that a phased-array achieved >10 dB/K G/T while being built by using all-silicon commercial chips and a cost-effective, planar, multilayer PCB. Note that if the array is designed to operate up to ±45° scan angles, as is common in many LEO applications, then the antenna unit cell area would increase by 29%, and the 1024 element array gain will become 35.1 dB at 11.7 GHz (1.1 dB increase). This will increase the G/T to 11.4 dB/K for the same design.

In chapter 4, a low-profile, planar, scalable, 256-element Ku-band phased array receiver with dual-beam reception is presented. It proves that a multi-beam receiver can be built on the same low-cost PCB with high isolation. Beamformers with 16 channels and silicon LNAs with very low NF result in an affordable, high performance and lower power multi-satellite arrays. To the author's knowledge, this is the first time such work with all silicon chips, dual-beam and high G/T is demonstrated.

5.2 Future Work

The Ku-band SATCOM phased-array systems presented in this dissertation may be expanded improved in a few aspects:

1) For the TX array, the power consumption will be decreased by using the next-generation beamformer chips from Renesas (available today). This will also improve the frequency response of the array, and make it centered at 14.25 GHz.

2) For the RX arrays, the G/T can be further improved by employing the next-generation LNAs and beamformer chips from Renesas (available today) with lower noise figure and much lower DC power consumption, designing an antenna with a wider bandwidth and optimizing the transmit rejection filter.

3) For the RX arrays, beamformer chips with 4-beam capability can be employed. By

this way, it can operate as a multi-purpose antenna. For example, 2 of the beams can be used in monopulse mode for accurate angular detection, while the others are used track or establish a link with LEO/GEO satellites or other flying objects.

4) For both TX and RX arrays, built-in-self-test (BIST) can be employed either on the chip or on the array element itself. This will enable cost-efficient online calibration for the terminals deployed.

5) For the RX arrays, beamformer chips with 32 channels can be used to feed 16 antennas (4x4). Still, the LNAs will be placed at the dual-polarized antenna terminals to preserve high G/T. This will lower the cost due to the beamformer chips, but create hotter spots on the PCB than before. Also, the longer transmission lines will cause feed line length differences around one wavelength and a lower instantaneous bandwidth.

Bibliography

[1] Intellian, "Intellian v85NX," *Intellian*. [Online]. Available: https://intelliantech.com/products/nx-maritime-vsat/v85nx/#. [Accessed: 03-Mar-2021].

[2] Viasat, "GAT-5530," *Viasat*. [Online]. Available: https://www.viasat.com/products/terminals-and-radios/gat-5530/. [Accessed: 03-Mar-2021].

[3] ThinKom, "Technology," *ThinKom*. [Online]. Available: https://www.thinkom.com/technology/. [Accessed: 03-Mar-2021].

[4] J. Gao, X. Lei, G.-H. Chen, Y. Zhang, and J.-M. Wu, "Design of the Variable Inclination Continuous Transverse Stub Antenna Based on Rectangular Grating Slow-Wave Structure," *International Journal of Antennas and Propagation*, vol. 2018, pp. 1-7, 2018.

[5] ALCAN Systems, "Technical Paper," *ALCAN Systems*. [Online]. Available: https://www.alcansystems.com/technical-paper/. [Accessed: 03-Mar-2021].

[6] Kymeta, "METAMATERIAL-SURFACE FLAT-PANEL ANTENNA TECHNOLOGY," *Kymeta*. [Online]. Available: https://www.kymetacorp.com/wp-content/uploads/2019/06/Metamaterial-Surface-Antenna-Technology.pdf. [Accessed: 03-Mar- 2021].

[7] R. Stevenson, M. Sazegar, A. Bily, M. Johnson, and N. Kundtz, "Metamaterial surface antenna technology: Commercialization through diffractive metamaterials and liquid crystal display manufacturing," *2016 10th International Congress on Advanced Electromagnetic Materials in Microwaves and Optics (METAMATERIALS)*, 2016.

[8] P. Hindle, "Comprehensive Survey of Commercial mmWave Phased Array Companies," *Microwave Journal*. [Online]. Available: https://www.microwavejournal.com/articles/33357-comprehensive-survey-of-commercial-mmwave-phased-array-companies. [Accessed: 03-Mar-2021].

[9] Isotropic Systems, "Solution," *Isotropic Systems*. [Online]. Available: https://www.isotropicsystems.com/solution. [Accessed: 03-Mar-2021].

[10] C. Daehnick, I. Klinghoffer, B. Maritz, and B. Wiseman, "Large LEO satellite constellations: Will it be different this time?," *McKinsey & Company*, 04-May-2020. [Online]. Available: https://www.mckinsey.com/industries/aerospace-and-defense/our-insights/large-leo-satellite-constellations-will-it-be-different-this-time#. [Accessed: 28-Feb-2021].

[11] Union of Concerned Scientists, "UCS Satellite Database," *Union of Concerned Scientists*, 01-Jan-2021. [Online]. Available: https://www.ucsusa.org/resources/satellite-database. [Accessed: 28-Feb-2021].

[12] S. Vaccaro, L. Diamond, D. Runyon and M. C. Vigano, "Ka-band mobility terminals enabling new services," *The 8th European Conference on Antennas and Propagation (EuCAP 2014)*, The Hague, 2014, pp. 2617-2618, doi: 10.1109/EuCAP.2014.6902358.

[13] D. Wilcoxson, B. Sleight, J. O'Neill and D. Chester, "Helicopter Ku-band SATCOM On-the-Move," *MILCOM 2006 - 2006 IEEE Military Communications Conference*, Washington, DC, 2006, pp. 1-7, doi: 10.1109/MILCOM.2006.302291.

[14] D. Wilcoxson, B. Sleight, D. Buchman and R. Vandermeulen, "Ku-band SATCOM on-the move network," *MILCOM 2005 - 2005 IEEE Military Communications Conference*, Atlantic City, NJ, 2005, pp. 231-237 Vol. 1, doi: 10.1109/MILCOM.2005.1605691.

[15] S. Vaccaro, F. Tiezzi, D. LLorens, M. F. Rua and C. D. G. de Oro, "Ku-Band Low Profile Antennas for Mobile Satcom," *2008 4th Advanced Satellite Mobile Systems*, Bologna, 2008, pp. 24-28, doi: 10.1109/ASMS.2008.11.

[16] G. Gultepe, S. Zihir, T. Kanar and G. M. Rebeiz, "A Dual-Polarized 1024-Element Ku-band SATCOM Transmit Phased-Array with $\pm 70°$Scan and 43.5 dBW EIRP," *2020 IEEE/MTT-S International Microwave Symposium (IMS)*, Los Angeles, CA, USA, 2020, pp. 837-840, doi: 10.1109/IMS30576.2020.9223977.

[17] L. Paulsen *et al.*, "Fabrication and Measurement of a Large, Monolithic, PCB-Based AESA," *2016 IEEE International Symposium on Phased Array Systems and Technology (PAST)*, Waltham, MA, 2016, pp. 1-7, doi: 10.1109/ARRAY.2016.7832654.

[18] A. H. Aljuhani, T. Kanar, S. Zihir and G. M. Rebeiz, "A Scalable Dual-Polarized 256-Element Ku-Band Phased-Array SATCOM Receiver with $\pm 70°$ Beam Scanning," *2018 IEEE/MTT-S International Microwave Symposium (IMS)*, Philadelphia, PA, 2018, pp. 1203-1206, doi: 10.1109/MWSYM.2018.8439257.

[19] A. H. Aljuhani, T. Kanar, S. Zihir and G. M. Rebeiz, "A Scalable Dual-Polarized 256-Element Ku-Band SATCOM Phased-Array Transmitter with 36.5 dBW EIRP Per Polarization," *2018 48th European Microwave Conference (EuMC)*, Madrid, 2018, pp. 938-941, doi: 10.23919/EuMC.2018.8541746.

[20] K. K. Wei Low, A. Nafe, S. Zihir, T. Kanar and G. M. Rebeiz, "A Scalable Circularly-Polarized 256-Element Ka-Band Phased-Array SATCOM Transmitter with $\pm 60°$ Beam

Scanning and 34.5 dBW EIRP," *2019 IEEE/MTT-S International Microwave Symposium (IMS)*, Boston, MA, USA, 2019, pp. 1064-1067, doi: 10.1109/MWSYM.2019.8701112.

[21] W. M. Abdel-Wahab *et al.*, "A Modular Architecture for Wide Scan Angle Phased Array Antenna for K/Ka Mobile SATCOM," *2019 IEEE/MTT-S International Microwave Symposium (IMS)*, Boston, MA, USA, 2019, pp. 1076-1079, doi: 10.1109/MWSYM.2019.8700842.

[22] D. M. Pozar, "Microstrip antennas," in *Proceedings of the IEEE*, vol. 80, no. 1, pp. 79-91, Jan. 1992, doi: 10.1109/5.119568.

[23] R. J. Mailloux, *Phased Array Antenna Handbook*, 2nd ed. Norwood, MA: Artech House, 2005, pp. 84âĂŞ87.

[24] A. Nafe, M. Sayginer, K. Kibaroglu and G. M. Rebeiz, "2x64 Dual-Polarized Dual-Beam Single-Aperture 28 GHz Phased Array with High Cross-Polarization Rejection for 5G Polarization MIMO," *2019 IEEE MTT-S International Microwave Symposium (IMS)*, Boston, MA, USA, 2019, pp. 484-487, doi: 10.1109/MWSYM.2019.8701105.

[25] M. Mirmozafari, G. Zhang, C. Fulton, and R. J. Doviak, "Dual-polarization antennas with high isolation and polarization purity: a review and comparison of cross-coupling mechanisms," in *IEEE Antennas Propag. Mag.*, vol. 61, no. 1, pp. 50-63, Feb. 2019, doi: 10.1109/MAP.2018.2883032.

[26] P. K. Mishra, D. R. Jahagirdar, and G. Kumar, "A Review of Broadband Dual Linearly Polarized Microstrip Antenna Designs with High Isolation [Education Column]," in *IEEE Antennas and Propagation Magazine*, vol. 56, no. 6, pp. 238-251, Dec. 2014, doi: 10.1109/MAP.2014.7011064.

[27] K. Ghorbani and R. B. Waterhouse, "Dual polarized wide-band aperture stacked patch antennas," in *IEEE Transactions on Antennas and Propagation*, vol. 52, no. 8, pp. 2171-2175, Aug. 2004, doi: 10.1109/TAP.2004.832484.

[28] S. D. Targonski and D. M. Pozar, "Design of wideband circularly polarized aperture-coupled microstrip antennas," in *IEEE Transactions on Antennas and Propagation*, vol. 41, no. 2, pp. 214-220, Feb. 1993, doi: 10.1109/8.214613.

[29] C. Sim, C. Chang, and J. Row, "Dual-Feed Dual-Polarized Patch Antenna With Low Cross Polarization and High Isolation," in *IEEE Transactions on Antennas and Propagation*, vol. 57, no. 10, pp. 3321-3324, Oct. 2009, doi: 10.1109/TAP.2009.2028702.

[30] T. Chi, J. S. Park, S. Li and H. Wang, "A Millimeter-Wave Polarization-Division-Duplex Transceiver Front-End With an On-Chip Multifeed Self-Interference-Canceling Antenna and an All-Passive Reconfigurable Canceller," in *IEEE Journal of Solid-State Circuits*, vol. 53, no. 12, pp. 3628-3639, Dec. 2018, doi: 10.1109/JSSC.2018.2878823.

[31] C. Thakkar, A. Chakrabarti, S. Yamada, D. Choudhury, J. Jaussi and B. Casper, "A 42.2-Gb/s 4.3-pJ/b 60-GHz Digital Transmitter With 12-b/Symbol Polarization MIMO," in *IEEE Journal of Solid-State Circuits*, vol. 54, no. 12, pp. 3565-3576, Dec. 2019, doi: 10.1109/JSSC.2019.2943924.

[32] J. Ruze, "The effect of aperture errors on the antenna radiation pattern," *Il Nuovo Cimento*, vol. 9, no. 3, pp. 364âĂŞ380, 1952.

[33] R. J. Mailloux, *Phased Array Antenna Handbook*, 3rd ed. Norwood, MA, USA: Artech House, 2018.

[34] J. L. Allen, "The theory of array antennas (with emphasis on radar applications)," *Massachusetts Inst. Technol. Lincoln Lab.*, Lexington, MA, USA, Tech. Rep. TR-323, Jul. 1963.

[35] R. Hansen, *Phased Array Antennas*, Hoboken, NJ, USA: Wiley, 1998.

[36] K. Kibaroglu, M. Sayginer, T. Phelps and G. M. Rebeiz, "A 64-Element 28-GHz Phased-Array Transceiver With 52-dBm EIRP and 8-12-Gb/s 5G Link at 300 Meters Without Any Calibration," in *IEEE Transactions on Microwave Theory and Techniques*, vol. 66, no. 12, pp. 5796-5811, Dec. 2018, doi: 10.1109/TMTT.2018.2854174.

[37] M. Vigilante, E. Mccune, and P. Reynaert, "To EVM or Two EVMs?: An Answer to the Question," in *IEEE Solid-State Circuits Magazine*, vol. 9, no. 3, pp. 36-39, Summer 2017, doi: 10.1109/MSSC.2017.2714398.

[38] H. T. Zhang, W. Wang, M. -P. Jin, X. -P. Lu, "A dual-polarized array antena for on-the-move applications in Ku-band," *2016 IEEE-APS Topical Conference on Antennas and Propagation in Wireless Communications (APWC)*, Cairns, QLD, Australia, 2016, pp. 5-8, doi: 10.1109/APWC.2016.7738102.

[39] B. Rupakula, A. H. Aljuhani and G. M. Rebeiz, "ACPR Improvement in Large Phased Arrays With Complex Modulated Waveforms," in *IEEE Transactions on Microwave Theory and Techniques*, vol. 68, no. 3, pp. 1045-1053, March 2020, doi: 10.1109/TMTT.2019.2944824.

[40] A. H. Aljuhani, T. Kanar, S. Zihir and G. M. Rebeiz, "A 256-Element Ku-band Polarization Agile SATCOM Transmit Phased-Array with Wide-Scan Angles, Low Cross-Polarization, Deep Nulls and 36.5 dBW EIRP Per Polarization," in *IEEE Transactions on Microwave Theory and Techniques* (accepted).

[41] L. Baggen and S. Holzwarth, "Satcom-on-the-move: Digital beam forming versus phased array," *The 8th European Conference on Antennas and Propagation (EuCAP 2014)*, The Hague, 2014, pp. 2610-2614, doi: 10.1109/EuCAP.2014.6902356.

[42] R. S. Wexler, D. Ho and D. N. Jones, "Medium data rate (MDR) satellite communications (SATCOM) on the move (SOTM) prototype terminal for the army warfighters," *MILCOM*

2005-2005 IEEE Military Communications Conference, Atlantic City, NJ, 2005, pp. 1734-1739 Vol. 3, doi: 10.1109/MILCOM.2005.1605924.

[43] A. R. Weily and N. Nikolic, "Dual-Polarized Planar Feed for Low-Profile Hemispherical Luneburg Lens Antennas," in *IEEE Transactions on Antennas and Propagation*, vol. 60, no. 1, pp. 402-407, Jan. 2012, doi: 10.1109/TAP.2011.2167941.

[44] S. Yamamoto, S. Nuimura, T. Mizuno, Y. Inasawa and H. Miyashita, "Low sidelobe compact reflector antenna using backfire primary radiator for Ku-band mobile satellite communication system on board vessel," *2013 Proceedings of the International Symposium on Antennas & Propagation,* Nanjing, 2013, pp. 653-656.

[45] A. I. Zaghloul, R. K. Gupta, E. C. Kohls, L. Q. Sun and R. M. Allnutt, "Low cost flat antennas for commercial and military SATCOM terminals," *2001 MILCOM Proceedings Communications for Network-Centric Operations: Creating the Information Force (Cat. No.01CH37277)*, McLean, VA, USA, 2001, pp. 795-799 vol.2, doi: 10.1109/MILCOM.2001.985951.

[46] I. Stoyanov, V. Boyanov, B. Marinov, Z. Dergachev, and A. Toshev, "Mobile Antenna system for satellite communications," U.S. Patent 6 999 036, Feb. 14, 2006.

[47] F. Tiezzi and S. Vaccaro, "Hybrid phased array antenna for mobile Ku-band DVB-S services," *2006 First European Conference on Antennas and Propagation*, Nice, 2006, pp. 1-4, doi: 10.1109/EUCAP.2006.4584587.

[48] S. Vaccaro, F. Tiezzi, M. F. Rúa and C. D. G. De Oro, "Ku-Band Low-Profile Rx-only and Tx-Rx antennas for Mobile Satellite Communications," *2010 IEEE International Symposium on Phased Array Systems and Technology*, Waltham, MA, 2010, pp. 536-542, doi: 10.1109/ARRAY.2010.5613316.

[49] F. Tiezzi, S. Vaccaro, D. Llorens, C. Dominguez and M. Fajardo, "Ku-band hybrid phased array antennas for mobile satellite communication systems," *2013 7th European Conference on Antennas and Propagation (EuCAP)*, Gothenburg, 2013, pp. 1605-1608.

[50] A. Catalani, G. Toso, P. Angeletti, M. Albertini, and P. Russo, âĂIJDevelopment of Enabling Technologies for Ku-Band Airborne SATCOM Phased-Arrays,âĂİ *Electronics*, vol. 9, no. 3, p. 488, 2020.

[51] G. M. Rebeiz and L. M. Paulsen, "Advances in SATCOM phased arrays using silicon technologies," *2017 IEEE MTT-S International Microwave Symposium (IMS)*, Honololu, HI, 2017, pp. 1877-1879, doi: 10.1109/MWSYM.2017.8059022.

[52] Y. Yin *et al.*, "A 37-42-GHz 8x8 Phased-Array With 48-51-dBm EIRP, 64-QAM 30-Gb/s Data Rates, and EVM Analysis Versus Channel RMS Errors," in *IEEE Transactions on Microwave Theory and Techniques*, vol. 68, no. 11, pp. 4753-4764, Nov. 2020, doi: 10.1109/TMTT.2020.2998183.

[53] B. Rupakula, A. Nafe, S. Zihir, Y. Wang, T. Lin and G. Rebeiz, "63.5âĂŞ65.5-GHz Transmit/Receive Phased-Array Communication Link With 0.5âĂŞ2 Gb/s at 100âĂŞ800 m and $\pm 50^{\circ}$ Scan Angles," in *IEEE Transactions on Microwave Theory and Techniques*, vol. 66, no. 9, pp. 4108-4120, Sept. 2018, doi: 10.1109/TMTT.2018.2839185.

[54] B. Rupakula, S. Zihir and G. M. Rebeiz, "Low Complexity 54-63-GHz Transmit/Receive 64- and 128-element 2-D-Scanning Phased-Arrays on Multilayer Organic Substrates With 64-QAM 30-Gbps Data Rates," in *IEEE Transactions on Microwave Theory and Techniques*, vol. 67, no. 12, pp. 5268-5281, Dec. 2019, doi: 10.1109/TMTT.2019.2952579.

[55] L. Baggen, S. Vaccaro, D. Llorens del Río, J. Padilla and R. T. Sánchez, "A compact phased array for satcom applications," *2013 IEEE International Symposium on Phased Array Systems and Technology*, Waltham, MA, 2013, pp. 232-239, doi: 10.1109/ARRAY.2013.6731833.

[56] J. -C. S. Chieh *et al.*, "Development of Flat Panel Active Phased Array Antennas Using 5G Silicon RFICs at Ku- and Ka-Bands," in *IEEE Access*, vol. 8, pp. 192669-192681, 2020, doi: 10.1109/ACCESS.2020.3032841.

[57] G. Gultepe, S. Zihir, T. Kanar and G. M. Rebeiz, "A Dual-Polarized 1024-Element Ku-band SATCOM Phased-Array with Embedded Transmit Filter and $>$10 dB/K G/T," presented at 2021 IEEE/MTT-S International Microwave Symposium (IMS), Atlanta, GA, USA, Jun. 6, 2021.

[58] G. Gultepe and G. M. Rebeiz, "A 256-Element Dual-Beam Dual-Polarization Ku-Band Phased-Array with 5 dB/K G/T for Simultaneous Multi-Satellite Reception," presented at 2021 IEEE/MTT-S International Microwave Symposium (IMS), Atlanta, GA, USA, Jun. 6, 2021.

[59] H. Holter and H. Steyskal, "On the size requirement for finite phased-array models," in *IEEE Transactions on Antennas and Propagation*, vol. 50, no. 6, pp. 836-840, June 2002, doi: 10.1109/TAP.2002.1017665.

[60] N. B. Buchanan, V. F. Fusco and A. Pal, "Squinted elevation antenna for Ku band DVB satellite reception with electronically steered azimuth," *2017 11th European Conference on Antennas and Propagation (EUCAP)*, Paris, 2017, pp. 3437-3440, doi: 10.23919/EuCAP.2017.7928538.

[61] A. H. Aljuhani, T. Kanar, S. Zihir and G. M. Rebeiz, "A 256-Element Ku-band Polarization Agile SATCOM Receive Phased-Array with Wide-Angle Scanning and High Polarization Purity," in *IEEE Transactions on Microwave Theory and Techniques* (accepted).

[62] G. Gultepe, T. Kanar, S. Zihir and G. M. Rebeiz, "A 1024-Element Ku-band SATCOM Dual-Polarized Receiver with $>$10 dB/K G/T and Embedded Transmit Rejection Filter," in *IEEE Transactions on Microwave Theory and Techniques* (accepted).

[63] G. Gultepe, T. Kanar, S. Zihir and G. M. Rebeiz, "A 1024-Element Ku-Band SATCOM Phased-Array Transmitter with 45 dBW Single-Polarization EIRP," in *IEEE Transactions on Microwave Theory and Techniques* (accepted).

[64] Cobham Aerospace Communications. [Online]. Available: https://www.cobhamaerospacecommunications.com/aircraft-satcom-systems/aircraft-satcom-antennas/high-gain-antennas-hga-class-6-432kbps/aviator-hga-7001/aviator-hga-7001-data-sheet/docview/. [Accessed: 03-Mar-2021].

[65] Hanwha-Phasor. [Online]. Available: https://www.hanwha-phasor.com/. [Accessed: 03-Mar-2021].

[66] Starlink. [Online]. Available: https://www.starlink.com/. [Accessed: 03-Mar-2021].

[67] L. Paulsen, "Single Panel Phased-Arrays for SATCOM and Low Power Radars," presented at 2018 IEEE/MTT-S International Microwave Symposium - IMS, Philadelphia, PA, USA, Jun. 11, 2018.

[68] W. Theunissen, V. Jain and G. Menon, "Development of a Receive Phased Array Antenna for High Altitude Platform Stations using Integrated Beamformer Modules," *2018 IEEE/MTT-S International Microwave Symposium - IMS*, Philadelphia, PA, USA, 2018, pp. 779-782, doi: 10.1109/MWSYM.2018.8439255.

[69] G. Gultepe and G. M. Rebeiz, "A 256-Element Dual-Beam Polarization-Agile SATCOM Ku-Band Phased-Array with 5 dB/K G/T," in *IEEE Transactions on Microwave Theory and Techniques* (submitted).